Chem Soc Rev

ROYAL SOCIETY OF CHEMISTRY

REVIEW ARTICLE

View Article Online
View Journal | View Issue

Cite this: *Chem. Soc. Rev.*, 2023, **52**, 3170

Dinuclear metal synergistic catalysis for energy conversion

Di-Chang Zhong, † Yun-Nan Gong,† Chao Zhang† and Tong-Bu Lu *

Catalysts featuring dinuclear metal sites are regarded as superior systems compared with their counterparts with mononuclear metal sites. The dinuclear metal sites in catalysts with appropriate spatial separations and geometric configurations can confer the dinuclear metal synergistic catalysis (DMSC) effect, and thus boost the catalytic performance, in particular for reactions involving multiple reactants, intermediates and products. In this review, we summarize the related reports on the design and synthesis of both homogeneous and heterogeneous dinuclear metal catalysts, and their applications in energy conversion reactions, including photo-/electro-catalytic hydrogen evolution reaction (HER), oxygen evolution reaction (OER), oxygen reduction reaction (ORR), CO_2 reduction reaction (CO_2RR), and N_2 reduction reaction (N_2RR). Particularly, we focus on the analysis of the relationship between the catalyst structure and catalytic performances, where the design principles are presented. Finally, we discuss the challenges in the design and preparation of dinuclear metal catalysts with the DMSC effect and present a perspective on the future development of dinuclear metal catalysts in energy conversion. This review aims to comprehensively summarize the up-to-date research progress on the synthesis and energy-related application of dinuclear metal catalysts and provide guidance for designing energy-conversion catalysts with superior performances.

Received 31st January 2023

DOI: 10.1039/d2cs00368f

rsc.li/chem-soc-rev

1. Introduction

With the rapid growth of the global economy and population, the huge consumption of non-renewable fossil fuels (such as coal and petroleum) has resulted in energy- and environment-related crises.[1–3] Therefore, the development of renewable energy sources to replace fossil fuels is urgent, where solar, wind and tidal energies are considered to be the most

Institute for New Energy Materials & Low-Carbon Technologies, School of Materials Science and Engineering, Tianjin University of Technology, Tianjin 300384, China. E-mail: lutongbu@tjut.edu.cn

† These authors contributed equally to this work.

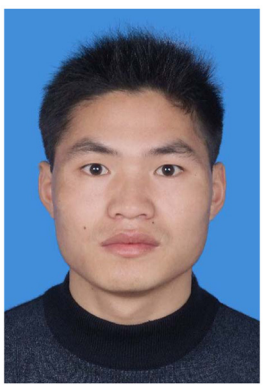

Di-Chang Zhong

Di-Chang Zhong obtained his BS in 2003 from Gannan Normal University and his MS in 2006 from Guangxi Normal University and PhD in 2011 from the Sun Yat-Sen University. Then, he joined the faculty at Gannan Normal University and was promoted as Professor in 2017. He worked as a JSPS Post-Doctoral Fellow at AIST, Japan for two years. In 2020, he moved to Tianjin University of Technology. His interests focus on the design and synthesis of molecular catalytic materials for energy storage and conversion.

Yun-Nan Gong

Yun-Nan Gong obtained his BS in 2008 and MS in 2011 from Nanchang Hangkong University and received his PhD in 2014 from Sun Yat-Sen University. Then, he joined the faculty at Gannan Normal University. He worked as a Post-Doctoral Fellow at the University of Science and Technology of China in 2018–2020. In 2021, he moved to Tianjin University of Technology and worked as an Associate Professor. His interests focus on the design and synthesis of porous materials for energy storage and conversion.

promising alternatives by virtue of their large capacity, environmental benignity and low cost.[4–6] However, infrastructure for both energy storage and conversion is required for these renewables because of their intermittent and distributed nature. Thus, in the past few decades, a wide variety of energy storage and conversion systems have been developed, among which photo-/electro-chemical reactions, including hydrogen evolution reaction (HER), oxygen evolution reaction (OER), oxygen reduction reaction (ORR), carbon dioxide reduction reaction (CO_2RR), and nitrogen reduction reaction (N_2RR), have attracted extensive attention.[7–16] However, to achieve efficient energy conversion in these important reactions, advanced catalysts with high performance and high stability are urgently required.

Conventionally, catalysts can be classified into homogeneous and heterogeneous catalysts.[17–19] Homogeneous catalysts work in the same phase as the reactants and are mainly soluble metal complexes.[20–24] They feature well-defined catalytic centers and maximized utilization of metal atoms, often showing high catalytic performances. Moreover, their catalytic mechanisms and structure–activity relationship are easier to elucidate. A series of metal complexes with good catalytic performances and well-recognized catalytic mechanisms in energy conversion reactions have been reported.[25–43] For instance, Robert *et al.* reported that an Fe–quaterpyridine complex could catalyze CO_2 photoreduction with high activity and selectivity.[29] Sun *et al.* developed an Ru complex showing excellent OER activity.[34] Our group also synthesized a series of non-noble-metal complexes for photocatalytic CO_2RR.[37–43] In contrast to homogeneous catalysts, heterogeneous catalysts operate in different phases with the reactants and can exist in the form of inorganic materials, metal–organic frameworks (MOFs), covalent organic frameworks (COFs) and graphitic carbon nitride materials.[44–50] These catalysts are extensively used in energy conversion because of their high stability and easy separation from the reaction mixtures. However, most heterogeneous catalysts usually suffer from suboptimal metal atom utilization because only a limited ratio of metal active sites on the catalyst surface can take part in the catalytic reactions. Therefore, numerous efforts have been devoted to downsizing the catalyst particles and/or regulating the surface morphology to expose more metal active sites and improve the catalytic efficiency.[51–54]

Mononuclear metal catalysts (MMCs), including conventional homogeneous mononuclear metal complexes and the emerging heterogeneous single-atom catalysts with atomically dispersed metals on solid supports, have received ever-growing interest in energy storage and conversion.[55–57] By virtue of the maximized utilization of metal active sites, MMCs usually display high catalytic activities and product selectivity. Thus, recently, significant progress has been achieved in the application of MMCs in the HER, OER, ORR, CO_2RR, N_2RR, *etc.*[58–64] However, these catalysts are often associated with the issue of transition states with a high free energy barrier owing to the complicated proton–electron transfer occurring on the single metal active site, which constrains the reaction kinetics. In this case, dinuclear metal catalysts (DMCs), with two adjacent metal centers as the catalytic active sites, are considered superior counterparts to MMCs, and thus have received increasing attention in energy storage and conversion. DMCs well inherit the characteristics of MMCs; more importantly, the neighbouring metal atoms in DMCs can give rise to a synergistic effect to lower the free energy barrier of the transition state, thus improving their catalytic performance.[65–69]

In 1975, Sonogashira *et al.* reported the cross-coupling reactions of halocarbons and acetylene using a Pd/Cu bimetallic catalyst. Its catalytic activity was found to be greatly improved after the addition of CuI to the catalytic system, given that copper(I) can function as a co-catalyst, promoting the deprotonation of terminal alkynes and the formation of copper(I) acetylides.[70,71] Afterwards, numerous efforts have been devoted to the field of dinuclear metal synergistic catalysis. Recently, dinuclear metal synergistic catalysis has been extensively

Chao Zhang

Chao Zhang obtained his BS in 2006 from Beijing Institute of Technology and his PhD in 2011 from Peking University. He worked sequentially as a Post-Doctoral Research Fellow at the Chinese University of Hong Kong and Peking University. He joined the faculty of Tianjing University of Technology in 2020 and worked as a Professor. Currently, his research interest is focused on the transport mechanisms across the macro–micro–nano scales in energy-related catalytic reactions.

Tong-Bu Lu

Tong-Bu Lu obtained his BS in 1988 and PhD in 1993 from Lanzhou University. After two years Post-Doctoral Fellowship at Sun Yat-Sen University, he joined the faculty at the same university, and became a Professor in 2000. He worked as a Post-Doctoral Fellow in F. Albert Cotton's group at Texas A&M University in 1998 and 2002, respectively. In 2016, he moved to Tianjin University of Technology. His current research interests focus on the study of artificial photosynthesis, including the design of homogeneous and heterogeneous catalysts for water splitting and CO_2 reduction.

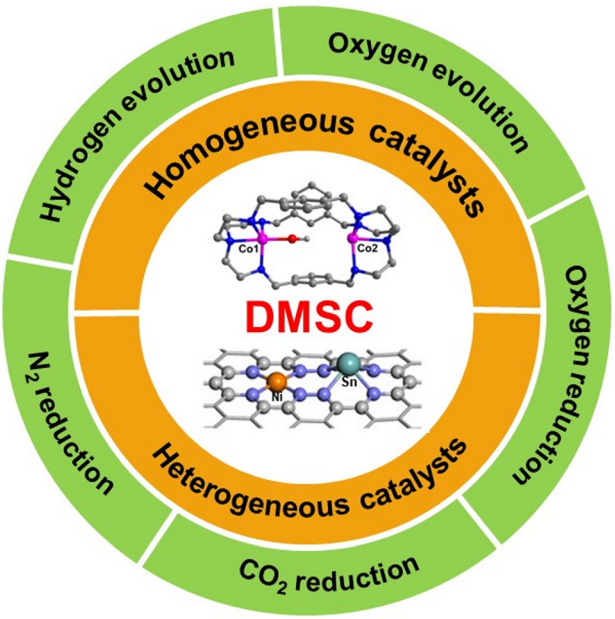

Scheme 1 Scope of this review.

explored in photo-/electro-catalytic reactions (such as HER, OER, ORR, CO_2RR and N_2RR) to enhance the catalytic efficiency.[72–77] In 2017, we first reported the dinuclear metal synergistic catalysis (DMSC) effect in photochemical CO_2 reduction into CO catalyzed by a dinuclear Co complex. The mechanistic study showed that one Co(II) acts as the catalytic center to bind and reduce CO_2, while the other Co(II) serves as the assisting site to promote the removal of the OH^- group from the COOH* intermediate, thus lowering the free energy barriers of the transition states and greatly boosting the catalytic activity.[42]

For the future development of the DMSC effect to boost the catalytic performance, it is timely to present a systematic overview of this field. Thus, in this review, we summarize the design and synthesis of both homogeneous and heterogeneous dinuclear metal catalysts for energy conversion reactions, including photo-/electro-catalytic HER, OER, ORR, CO_2RR and N_2RR (Scheme 1). Furthermore, a series of design protocols and principles is highlighted to reveal the structure–property relationship of the catalysts. Finally, the persisting challenges and future prospects on the design of dinuclear metal catalysts with the DMSC effect in energy conversion are discussed. We hope that this review will help garner the attention of more researchers for DMSC for energy conversion and provide guidance for the design of efficient energy-conversion catalysts.

2. DMSC and related catalysts

2.1 Definition, synthesis and catalytic mechanism of DMSC catalysts

Generally, DMSC catalysts are defined as dinuclear metal centers with suitable spatial separations and coordination configurations directly or indirectly taking part in the catalytic process, where catalysts featuring dinuclear metal centers shows a notable enhancement in catalytic activity with respect to their mononuclear counterparts.[75] For dinuclear metal complexes and metal–organic frameworks (MOFs) with dinuclear metal structural units, their crystal structures can be well analyzed *via* single-crystal X-ray diffraction (XRD), and thus the metal–metal distances and the coordination configurations can be determined with high precision *via* structural analysis.[67,78] For heterogeneous catalysts without significant long-range order, their structures are relatively unclear, despite the fact that their local structures are usually inferred *via* aberration-corrected high-angle annular dark-field scanning transmission electron microscopy (HAADF-STEM), X-ray absorption spectroscopy (XAS), electron energy loss spectroscopy (EELS), Mössbauer spectroscopy and other advanced characterization techniques. Based on the above-mentioned analysis, it is reasonable to classify DMSC catalysts as homo-nuclear and hetero-nuclear diatomic ones.[68,69] The periodic or local structures of these catalysts are often deciphered *via* single-crystal XRD or aberration-corrected HAADF-STEM and XAS. Reported examples include dinuclear Co–Co complexes, dinuclear Co–Zn complex, and dinuclear Cu–Cu catalyst.[75] The dinuclear metal centers in these catalysts can synergistically catalyze energy conversion reactions, demonstrating catalytic activities tens of times higher than that of their mononuclear counterparts. Besides, in some studies, it has been found that two types of metals randomly dispersed in a catalyst can also show enhanced catalytic activity over single-metal catalysts in energy conversion reactions. Specifically, a synergistic catalytic effect was identified between two metal centers, but their spatial separations and coordination configurations are uncertain. This type of catalyst is the so-called marriage-type bimetallic catalysts.[75] However, owing to the difficulty in revealing their structure–performance relationship, these catalysts will be not included and discussed in this review.

According to the types of dinuclear metal catalysts, the related synthesis methods can be divided into direct synthesis, precursor pyrolysis, and sequential deposition.[67–69] Direct synthesis is well applicable for the dinuclear metal complexes and MOFs with dinuclear metal structural units, which are usually obtained *via* the direct reaction of metal ions and organic ligands under specific conditions. Besides, the encapsulation of dinuclear metal complexes in the pores of porous materials and anchoring dinuclear metal complexes on supports *via* covalent bonds or supramolecular/electrostatic interactions can also be considered direct methods to obtain supported dinuclear metal catalysts. Consequently, the heterogenization of molecular catalysts can be achieved, and their durability and recycling ability can be improved, and thus their significance for practical application can be elevated. Pyrolysis of the precursor is an effective method for the precise preparation of heterogeneous dinuclear metal catalysts, where the precursors are usually MOFs containing dinuclear metal structural units or dinuclear metal complexes supported materials. Although pyrolysis destroys most parts of the MOF structures and the dinuclear metal complex supported materials, the essential dinuclear metal structural units are expected to be retained on the new *in situ* generated carbonaceous supports

with nitrogen (or other heteroatom) doping. The abundant nitrogen and carbon species resulting from pyrolysis can not only provide a carbonaceous support but also stabilize and regulate the coordination structures of dinuclear metal meters through the coordination of C and/or N atoms. These annealed catalysts with dinuclear structural units have been found to synergistically catalyze energy conversion reactions. For example, the precursors of bis(1,5-cyclooctadiene) diiridium(I) dichloride, dicarbonylcyclopentadienyliron, and allylpalladium(II) chloride dimer have been successfully used for the preparation of Ir_2, Fe_2, and Pd_2/mpg-C_3N_4 DMCs[79] and a diatomic Ag_2/graphene catalyst was obtained with a dinuclear Ag complex as the precursor.[80] The sequential deposition of identical or different metal atoms *via* atomic layer deposition (ALD) can precisely control the synthesis of bimetallic catalysts, where the key is to avoid the random distribution and aggregation of metal atoms, and thus the selective deposition of the second metal precursor is critical. Diatomic Pt_2 sites anchored on graphene were constructed *via* two-step sequential ALD, in which the steric hindrance induced by trimethyl(methylcyclopentadienyl)–platinum(IV) ($MeCpPtMe_3$) ensured the selective deposition of the second Pt in close proximity to the first Pt atom.[81]

The synergistically enhanced catalytic activity of dinuclear catalysts has attracted considerable research interest. Their synergistic catalysis mechanisms have also been studied in depth. Remarkably, the specifically synergistic catalysis mechanism of dinuclear metal catalysts is dependent on the catalyst itself, as well as the type of energy conversion reactions. Generally, there are two types of synergistic catalysis modes employed by dinuclear catalysts in catalyzing energy conversion reactions. The first mode features both metal centers directly binding with the substrate molecules or the reaction intermediates. In this case, the substrate molecules are activated by both metal centers, or the reaction intermediates are stabilized by both metal centers.[42,43,82] The second mode features only one metal center directly binding and activating the substrate molecules and reaction intermediates, with the neighboring metal center not taking part in the activation or stabilization of the reaction intermediates; nonetheless, this type of structure can slightly modulate the electronic structure of the adjacent metal center, thereby indirectly contributing to boosting the catalytic activity.[83] Most dinuclear metal electrocatalysts catalyze energy conversion reactions in this mode. In addition, the neighboring metal center can also bind with H_2O or other molecules, and the bonded H_2O can form hydrogen bonds with the reaction intermediates attached to the adjacent metal center and stabilize the reaction intermediates, thus also indirectly facilitating the catalytic process.[84]

2.2 DMSC for energy conversion reactions

As discussed above, dinuclear metal catalysts not only inherit the advantages of mononuclear catalysts, but also have more diverse functionalized sites, thereby meeting the demands of complex reactions. The energy conversion reactions typically include photo-/electro-catalytic HER, OER, ORR, CO_2RR, and N_2RR.[65–69,72–77] Designing dinuclear or multinuclear metal catalysts for these reactions may be related to the discoveries in biological studies. It has been found that in biological systems, many catalytic active centers of metalloenzymes have dinuclear metallic complexes as their essential parts, such as $[NiFe_4(OH)S_4]$ cluster-based carbon monoxide dehydrogenase (CODHs), $CaMn_4O_4$ oxygen evolving center in photosystem II, dinuclear-Fe-based hydrogenase, dinuclear-Cu-based tyrosinase and laccase.[85–89] These metalloenzymes are involved in diverse physiological functions in biological systems by metal–metal cooperation to achieve substrate recognition and transformation. Actually, all the above-mentioned energy conversion reactions are related to the formation or activation of stable chemical bonds. For instance, the HER involves the H–H bond formation process. In particular, for the proposed Tafel step after the Volmer step, two adsorbed *H are combined into adsorbed $*H_2$, which eventually desorbs to form free H_2.[69] The OER process also involves bond formation.[77] The typical catalytic pathway of dinuclear metal complexes for the OER is dinuclear cooperative catalysis following the I_2M mechanism, in which two M–O units interact to form an O–O bond. The ORR, CO_2RR, and N_2RR processes involve the activation of di-/tri-atomic molecules of O_2, CO_2, and N_2.[66,73,76] The coordination interactions of dinuclear metal centers in dinuclear metal catalysts with suitable metal–metal separation and configuration can contribute to their adsorption and activation, as well as the subsequent stability of the generated reaction intermediate, and thus conducive to the reduction of these molecules.

3. DMSC for energy conversion in homogeneous catalytic system

As the most representative homogeneous catalysts, metal complexes are constructed from metal ions and organic ligands *via* coordination bonds and have been widely used for photo-/electro-chemical energy conversion reactions.[20] Benefiting from the maximized utilization of metal active sites, metal complexes are often efficient and selective for these reactions. In particular, dinuclear metal complexes with suitable metal–metal separations and spatial configurations have recently been scrutinized with increasing interest because the dinuclear active sites show a synergistic catalysis effect to further enhance the catalytic efficiency.[66]

In this section, dinuclear metal complexes for photo-/electro-catalytic HER, OER, ORR, CO_2RR, and N_2RR in homogeneous catalytic systems will be summarized and discussed. The contents of this section are divided into five parts.

3.1 HER

Hydrogen, as a promising renewable high-energy fuel, has been considered an ideal alternative to conventional fossil fuels.[89] Electrochemical HER provides a promising solution to produce high-purity hydrogen gas.[90] However, to implement this important reaction, electrocatalysts with high efficiency are required. Recently, a wide library of homo-dinuclear complexes has

demonstrated the cooperativity of metal active centers in electrocatalytic HER.[91–100] For example, Peters *et al.* prepared a variety of dinuclear cobalt macrocycle complexes using $Co(OAc)_2$, dioxime precursors and $BF_3{\cdot}Et_2O$, which could be used as highly active electrocatalysts for proton reduction. Because of the directing cooperative substrate binding between the adjacent Co atoms, these dinuclear cobalt macrocycle complexes exhibited excellent electrocatalytic performances with relatively low overpotentials.[91] Apfel *et al.* reported a bimetallic macrocycle complex featuring two cofacially linked Ni–porphyrins for electrochemical HER. Compared with the Ni hangman porphyrin, the dinuclear Ni macrocycle complex achieved two-times higher HER activity with a faradaic efficiency (FE) of 95% and H_2 production rate of 1.4 mmol g^{-1} h^{-1}. The improved catalytic efficiency can be attributed to the synergistic effect between the two Ni centers.[92] Zhan *et al.* synthesized a dinuclear copper complex from $Cu(OH)_2$ and *N*,*N*′-bis(3-aminopropyl) oxamido ligand, which could work as a bifunctional electrocatalyst for both water oxidation and reduction. The electrochemical results demonstrated that water oxidation could be initiated at an overpotential of 0.289 V with a TOF of 6.7 s^{-1}, and the water reduction could be driven at the overpotential of 0.689 V with a TOF of 1383 h^{-1}. This dinuclear copper complex also showed high stability for water reduction for over 72 h electrolysis with an FE_{H2} of 97.4%.[93]

In addition, Cao *et al.* designed and synthesized a nickel(II) porphyrinic complex (Ni–P, P = porphyrin) bearing four *meso*-C_6F_5 groups for the HER. In the catalytic HER cycle, rapid bimetallic-site-catalyzed homolysis to produce H_2 was achieved, as shown by experimental and theoretical studies. The experimental results revealed that Ni–P exhibits high catalytic activity and stability, with a remarkable i_c/i_p ratio of 77 (i_c is the catalytic current and i_p is the peak current). The theoretical calculations demonstrated that the intermediate [H–Ni–P] undergoes homolysis to generate H_2 with a very low activation energy barrier of 3.7 kcal mol^{-1}, which suggests fast reaction kinetics.[94] To further confirm the homolytic H–H bond formation mechanism, the same team prepared three nickel(II) porphyrinic complexes by introducing bulky amido moieties in the *ortho*- or *para*-position of *meso*-phenyl groups. The complex bearing amido moieties at the *para*-position showed much smaller steric resistance at the direction perpendicular to the porphyrin ring, which underwent bimetallic homolysis to yield H_2.[95] Moreover, Sakai *et al.* found that mononuclear platinum(II) complexes formed dimeric structures with a metal–metal bond when they are used to catalyse H_2 generation from water. Furthermore, chloride ions were introduced in the platinum(II) complexes to minimize the coulombic repulsion between the two mononuclear units, which enhanced the capability of forming a dimer, thus improving the HER activity.[96]

Besides, some hetero-dinuclear metal complexes have been synthesized for the HER with the DMSC effect. For instance, Darensbourg *et al.* prepared an Ni–Fe bimetallic complex from $CpFe(CO)_2I$ and Ni(*N*,*N*-bis(2-mercaptoethyl)-1,5-diazacycloheptane) for electrochemical HER. This Ni–Fe bimetallic catalyst displayed excellent catalytic performance for H_2 generation with a turnover number (TON) and FE of 0.26 ± 0.01 and 96.0 ± 2.9%, respectively, which are superior to that of the homo-dinuclear Fe–Fe catalyst (TON = 1.92 and FE = 77.2%). The computational investigation demonstrated controlled proton–electron and proton–hydride coupling by the [NiFe]-hydrogenase active site to promote H_2 production.[97]

3.2 OER

The OER is a very important half reaction for energy conversion and storage.[101] However, this reaction is rather challenging owing to the transfer of four protons and four electrons. Dinuclear metal complexes have attracted broad attention in water oxidation because the two metal centers can activate different water molecules simultaneously to achieve O–O coupling. In recent years, many homo-dinuclear metal complexes have shown outstanding performance for electrocatalytic water oxidation.[102–116] In 2012, Mayer *et al.* prepared the dimeric bis-μ-hydroxide cation $[(bipyridine)Cu(\mu\text{-}OH)]_2^{2+}$ for the OER. The catalytic results demonstrated that this dinuclear complex shows large and irreversible currents at pH 11.8–13.3, indicating its high catalytic activity. The overpotential was 750 mV at pH 12.5, and the catalytic TOF was 100 s^{-1}, suggesting very fast kinetics. This is the first copper-based homogeneous catalyst for water oxidation.[102] Moreover, Zhang *et al.* synthesized a robust dinuclear copper catalyst for water oxidation from $Cu(CF_3SO_3)_2$ and 2,7-[bis(2-pyridylme-thyl)aminomethyl]-1,8-naphthyridine (BPMAN). The catalytic results demonstrated that this catalyst showed high activity with an overpotential of 0.8 V in phosphate buffer (pH = 7). DFT calculations revealed that the two Cu centers have a cooperative interaction to form O–O bonds, thus efficiently catalyzing water oxidation.[103] In addition, Zhang *et al.* prepared three copper-based complexes involving mononuclear, dinuclear and trinuclear copper clusters for electrocatalytic water oxidation. The trinuclear copper complex exhibited excellent activity with TOF of 20 000 s^{-1}, which is 15 times and 150 times higher than that of dinuclear and mononuclear copper complexes, respectively. Control experiments together with theoretical calculations showed that the cooperation between multiple metals plays a crucial role in O–O bond formation.[104]

Besides, Kieber-Emmons *et al.* prepared a dinuclear copper complex, $\{[(Me_2TMPA)Cu(II)]_2(\mu\text{-}OH)_2\}(OTf)_2$, *via* the metalation of Me_2TMPA (Me_2TMPA = bis((6-methyl-2-pyridyl)methyl)(2-pyridylmethyl)amine) for electrocatalytic water oxidation. This catalyst displayed a high FE of 90% and moderate TOF of 33 s^{-1} at ~1.0 V (*vs.* NHE). The kinetic isotope effect of the catalyst was calculated to be 20 at 1.5 V (*vs.* NHE), suggesting that proton-coupled electron transfer is the rate-determining step (RDS). DFT calculations revealed that both the nucleophilic attack of intermolecular water and redox isomerization of $\{[LCu(III)]_2(\mu\text{-}O)_2\}^{2+}$ are energetically accessible pathways for O–O bond formation.[105] Maayan *et al.* also fabricated a dinuclear copper catalyst for water oxidation, which demonstrated high performance and stability (Fig. 1). The TOF reached 129 s^{-1} (peak current measurements) or 5503 s^{-1} (foot-of-the-wave

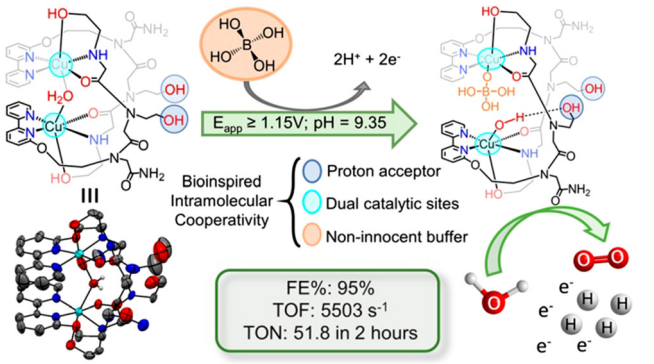

Fig. 1 Schematic illustration showing the cooperative water oxidation process with high activity over a dinuclear copper complex. Reproduced from ref. 106 with permission from the American Chemical Society, Copyright 2021.

analysis). The experimental TON value was 21.8 with FE of 95% in 2 h at an overpotential of ~600 mV. This catalyst could work stably for at least four cycles of potentiostatic electrolysis, as confirmed *via* spectroscopic and electrochemical techniques. The high catalytic performance of this dinuclear copper catalyst can be attributed to the cooperative interactions between the two Cu sites, as well as the –OH groups of the ethanolic side chains promoting proton transfer and borate species coordinated on one of the Cu sites, thus facilitating O–O bond formation.[106]

In addition to dinuclear copper complexes, some other dinuclear metal complexes have been constructed for electrocatalytic water oxidation. For instance, Zhang *et al.* synthesized a dinuclear cobalt complex bearing five- and six-coordinated sites, which can be used as a stable and efficient water oxidation catalyst. Different from O–O coupling, this catalyst has a "one-site catalysis with two-site oxidation" mechanism, that is, water oxidation occurs on two metal sites and the O–O bond is formed on one site with an FE of over 90% under neutral conditions.[107] Åkermark *et al.* prepared a series of dinuclear manganese complexes with different substituents in the ligand scaffold for electrocatalytic water oxidation. It was found that all these complexes can oxidize H_2O to O_2, among which the manganese-based complex containing distal carboxyl group exhibited the highest catalytic activity. The significantly improved performance is attributed to the hydrogen bonding between the Mn–hydroxy group and distal carboxyl group, which promotes the proton-coupled electron transfer, thus accelerating O–O bond formation during H_2O oxidation.[108]

3.3 ORR

The ORR is of utmost importance for energy storage and conversion technologies, such as fuel cells and metal–air batteries.[117] In 1964, Jasinski *et al.* synthesized a cobalt–phthalocyanine complex, which was first used as a molecular catalyst for the ORR under alkaline conditions.[118] Afterwards, a wide library of molecular catalysts has been developed for this reaction, among which dinuclear metal complexes have attracted considerable attention due to the synergistic effect of two metal centers promoting the activation and catalytic conversion of O_2.[119–127] Duboc *et al.* synthesized a dinuclear non-heme iron complex from $Fe(BF_4)_2{\cdot}6H_2O$ and 2,2′-(2,2′-bipyridine-6,6′-diyl)bis(1,1-diphenylethanethiolate) ligand, which can act as a high-efficiency ORR catalyst for the selective reduction of O_2 into H_2O_2 or H_2O. Under conventional chemical conditions, H_2O_2 is the main product with a selectivity of 95%, whereas under electrochemical conditions, H_2O is dominant, with <10% H_2O_2 produced. Theoretical calculations demonstrated that the production of H_2O_2 is thermodynamically and kinetically feasible under chemical conditions. When electrochemically driven, H_2O_2 is further reduced to H_2O owing to the fast electron transfer occurring in the reaction diffusion layer to break the O–O bond.[119] Moreover, Tanaka *et al.* prepared a dinuclear iron complex with both Fe–porphyrin and Fe–phthalocyanine as the catalytic centers for electrochemical ORR. This complex could catalyze the four-electron reduction of O_2 into H_2O with an onset potential of 0.78 V (*vs.* RHE). The excellent catalytic efficiency of the catalyst can be attributed to the electrostatic repulsion between the active metal center and the adjacent ammonium cations.[120]

In 2018, Maron *et al.* constructed a dinuclear cobalt complex based on a dianionic pentadentate ligand for the electrochemical reduction of O_2 to H_2O. This complex contained a diamagnetic Co^{III}–O–O–Co^{III} peroxo dimer, with an O–O distance of 1.43 Å, which is longer than that in O_2 (1.21 Å). This suggests a formally doubly reduced peroxo complex. Both the experimental and computational results demonstrated facile O–O bond cleavage and formation in the catalytic process, and the dianionic nature of the ligand plays a central role in the O–O bond cleavage to form H_2O. This is a new reaction pathway for the reduction of O_2 to H_2O by Co^{III}–O–O–Co^{III} peroxo intermediates.[121] Furthermore, Cao *et al.* designed and synthesized an asymmetrical Pacman dinuclear cobalt complex with the face-to-face configuration of two porphyrin moieties for electrochemical ORR (Fig. 2a). The catalytic results demonstrated that this complex is more efficient and selective than the corresponding mononuclear cobalt complex and symmetrical dinuclear cobalt complex for the four-electron reduction of O_2 to H_2O (Fig. 2b). The enhanced catalytic activity of the dinuclear cobalt complex is attributed to the cooperation between the two Co ions, that is, one Co–porphyrin moiety is likely the O_2 binding and reduction site, while the other may be used as a Lewis acid to assist the O_2 binding and activation (Fig. 2c).[122] Similarly, a series of other dinuclear cobalt cofacial porphyrin–corrole dyads have been constructed, which displayed good activities for electrochemical O_2 reduction.[123–125]

Besides, Cao *et al.* also prepared a water-soluble binuclear Cu^{II} complex for the reduction of O_2 into H_2O under neutral aqueous solution. The electrocatalytic results demonstrated that one Cu^{II} center is first reduced by one electron to form $Cu^{II}Cu^{I}$ species, which can activate an O_2 molecule to generate $O_2^{\bullet-}$. Then, $O_2^{\bullet-}$ is further reduced at the dicopper site to give H_2O. These results suggest the cooperation between the two Cu atoms for the ORR.[126] Mirica *et al.* synthesized a mononuclear

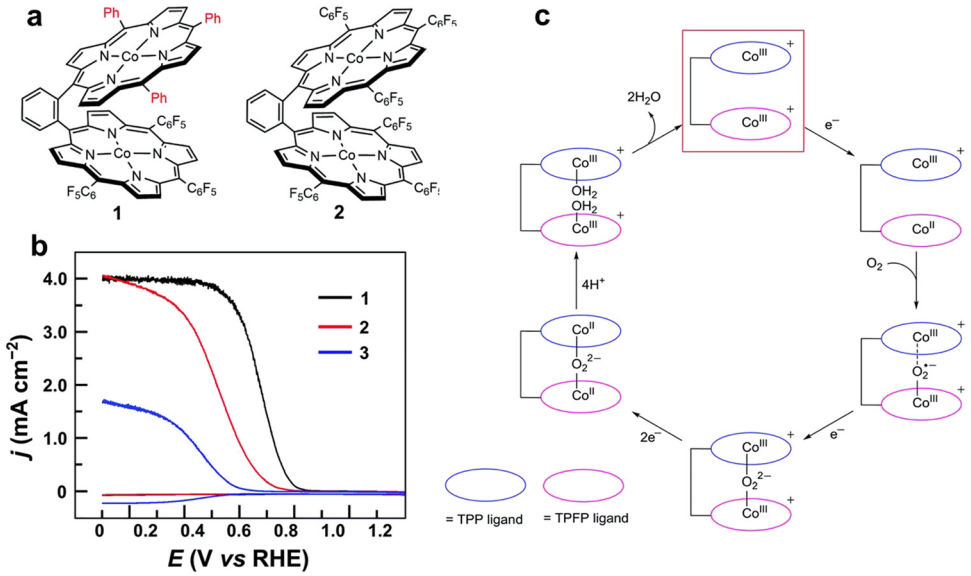

Fig. 2 (a) Molecular structures of asymmetrical (left) and symmetrical (right) dinuclear cobalt complexes. (b) Rotating ring-disk electrode measurements for the ORR with asymmetrical (black) and symmetrical (red) dinuclear cobalt complexes, as well as mononuclear cobalt complex (blue) in O_2-saturated 0.5 M H_2SO_4 solution. (c) Proposed catalytic cycle for the ORR over asymmetrical dinuclear cobalt complexes. Reproduced from ref. 122 with permission from The Royal Society of Chemistry, Copyright 2020.

palladium complex as a molecular homogeneous electrocatalyst for the selective reduction of O_2 into H_2O. This catalyst exhibited elevated ORR kinetics with a low overpotential of 0.32 V and high FE of 70% in MeCN solution. The electrochemical results imply that a dinuclear Pd^{III} intermediate, most likely a Pd^{III}–peroxo–Pd^{III} species, was formed in solution, which dictates the thermochemistry of the ORR process.[127]

3.4 CO_2RR

CO_2RR, powered either photochemically or electrochemically, has been regarded as promising technology to achieve carbon neutrality.[128] The activation of the CO_2 molecule and the stabilization of the reaction intermediates are the crucial issues. DMCs have been found to be unique for binding, activating and converting CO_2 molecules. A series of homo- and hetero-bimetallic complexes has been designed for photo- and electro-catalytic CO_2RR with the DMSC effect between two metal centers.

3.4.1 Photocatalysis. In 2017, we synthesized a dinuclear CoCo complex by confining two Co atoms in a cryptand for efficient CO_2 photoreduction to CO in CH_3CN/H_2O solution (Fig. 3a). This dinuclear CoCo complex could rapidly absorb CO_2 in its cavity to form carbonate with coordinated OH^-, as confirmed by single-crystal XRD. Therefore, it exhibited an extraordinarily high catalytic performance for CO_2-to-CO conversion, with a TON and TOF of 16 896 and 0.47 s^{-1}, which are much higher than that of the corresponding mononuclear Co complex (Fig. 3b and c), respectively. The enhanced catalytic efficiency is due to the DMSC effect between two Co, that is, one Co serves as a catalytic center to bind and reduce CO_2, and the other acts as an assisting catalytic site to facilitate the C–OH cleavage of the $[O{=}C{-}OH]^{\ddagger}$ intermediate and removal of the OH^- group, thus promoting CO production. This has been well supported by the DFT result, where it can be seen that the C–OH cleavage of the $[O{=}C{-}OH]^{\ddagger}$ intermediate is the RDS of the CO_2 reduction reaction, and in this step the dinuclear CoCo complex has a much lower energy barrier than its mononuclear counterpart (Fig. 3d).[42] Then, Robert *et al.* prepared a dinuclear Co complex bearing a bi-quaterpyridine ligand, which could selectively catalyze photochemical CO_2 reduction into $HCOO^-$ or CO by two Co atoms acting in synergy towards CO_2. In this work, $HCOO^-$ was produced with a selectivity of 97% and TON of 821 in basic acetonitrile solution, while CO production was achieved with a selectivity of 99% and TON of 829 in the presence of a weak acid. DFT calculations showed that this dinuclear Co complex undergoes different reaction pathways to reduce CO_2 to $HCOO^-$ and CO.[129] Moreover, Tschierlei *et al.* designed and synthesized a dinuclear Re complex, in which two (bipyridine)$Re(CO)_3Cl$ fragments are linked by a xanthene backbone. The catalytic results demonstrated that this dinuclear Re complex displayed significantly increased activity for photochemical CO_2-to-CO conversion compared to its mononuclear parent complex. The enhanced catalytic performance was attributed to the cooperative reaction mechanism between the two Re centers, where one Re center functions as a photosensitizer to assist the second active Re to accomplish CO_2 reduction.[130] In addition, Wang *et al.* prepared a dinuclear nickel complex for visible-light-driven CO_2 reduction. By using 50 μM dinuclear nickel complex, 3.25 μmol of CO and a selectivity of 99% were achieved, which are higher than 100 μM of the corresponding mononuclear Ni complex (2.60 μmol and 90%, respectively). The enhanced catalytic efficiency of the dinuclear nickel complex can be attributed to the synergy between two Ni sites.[131]

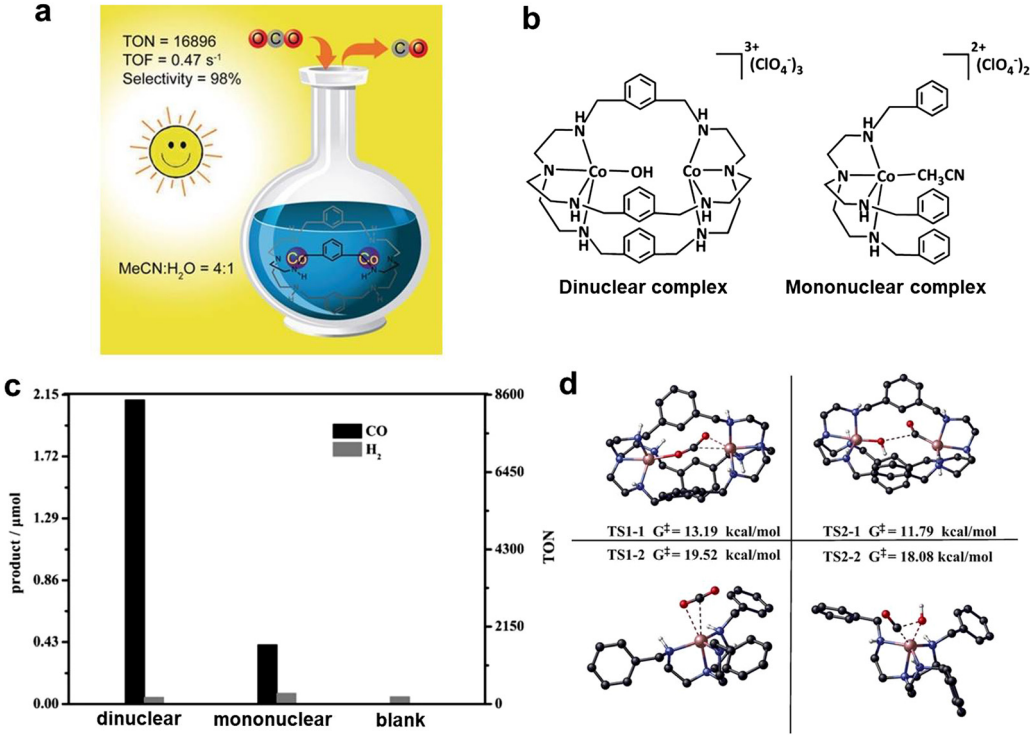

Fig. 3 (a) Schematic illustration of the dinuclear Co complex for efficient CO_2 photoreduction to CO in CH_3CN/H_2O solution. (b) Molecular structures of dinuclear and mononuclear Co complexes. (c) CO and H_2 yields obtained over dinuclear Co complex (0.025 μM), mononuclear Co complex (0.05 μM) and blank. (d) Energy barriers of CO_2 reduction and C–OH cleavage for dinuclear Co complex (top) and mononuclear Co complex (bottom). Reproduced from ref. 42 with permission from Wiley-VCH, Copyright 2017.

Besides homo-dinuclear metal complexes, hetero-dinuclear ones have also been shown to reduce CO_2 in synergy. As is known, zinc complexes usually exhibit only marginal photocatalytic activity for the CO_2RR, but Zn(II) has a strong binding affinity to the OH^- group, which is expected to be an ideal assisting catalytic site to promote the cleavage of the C–OH bond in the process of CO_2 reduction, thus improving the catalytic efficiency. Therefore, based on the fact that dinuclear CoCo complexes synergistically catalyse CO_2 reduction to CO, we further designed and synthesized a dinuclear heterometallic CoZn complex for photochemical CO_2-to-CO conversion. As expected, this CoZn complex showed extremely high photocatalytic activity with TON and TOF values of 65 000 and 1.8 s^{-1}, which are 4- and 19-fold higher than that of the homo-dinuclear CoCo and ZnZn complexes, respectively. DFT calculations revealed that the DMSC effect between Co and Zn is significantly strengthened with respect to the Co/Co and Zn/Zn counterparts, therefore dramatically lowering the activation barriers of the transition states, and subsequently increases the catalytic activity for photochemical CO_2 reduction to CO.[43] Additionally, Kojima *et al.* synthesized a mononuclear Ni complex based on S_2N_2-tetradentate ligand with two non-coordinated pyridine pendants, in which the pyridine pendants can capture Lewis-acidic metal ions by coordination to form hetero-binuclear metal complexes for photocatalytic CO_2RR (Fig. 4a). Consequently, the Mg, Ca or Zn-bound Ni complexes showed significantly enhanced photocatalytic performance for the reduction of CO_2 to CO compared to that of their mononuclear Ni complex without pyridine pendants, which can be ascribed to the cooperativity between the Ni and Mg, Ca or Zn centers for the stabilization of the Ni–CO_2 intermediate (Fig. 4b and c).[132]

Besides, hetero-dinuclear metal complexes containing noble metals can also exhibit the DMSC effect in photocatalytic CO_2RR, but the synergistic catalysis mechanism is different from that discussed above. For example, Kuramochi *et al.* prepared a dinuclear heterometallic complex by covalently connecting an Re complex and Zn–porphyrin complex for photocatalytic CO_2 reduction. Because of the rapid electron transfer from the Zn–porphyrin to the Re complex, this hetero-dinuclear metal complex exhibited high activity and selectivity to afford CO, with a TON of >1300 and selectivity of >99.9%, while the mixed system of the Re complex and the Zn porphyrin barely gave any CO.[133] A similar conclusion was reported by Schwalbe *et al.* They constructed a series of hetero-dinuclear complexes based on a phenanthroline extended tetramesityl porphyrin ligand, in which the porphyrin center was implanted with Cu, Pd, Zn, Co, or Fe, and the phenanthroline was coordinated by an Re tricarbonyl chloride unit. Among them, the hetero-dinuclear ZnRe complex showed high photocatalytic performance for CO_2-to-CO conversion with a TON of 13 without other noble metal photosensitizers, while the other hetero-dinuclear complexes are inactive under the same condition. These results suggest that cooperative catalysis is possible by

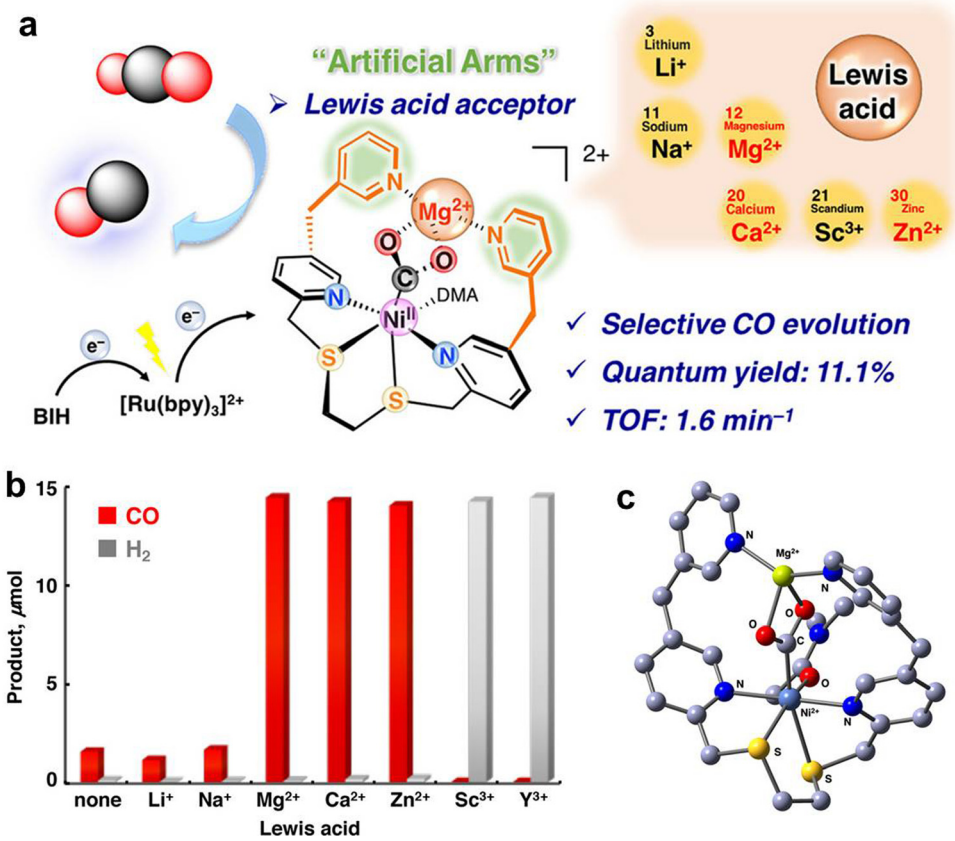

Fig. 4 (a) Schematic illustration of the Mg, Ca or Zn-bound Ni complex for synergistic photocatalytic CO_2 reduction to CO. (b) CO and H_2 yields in photocatalytic CO_2RR over Ni complex in the presence of cationic Lewis acids at 1 h. (c) Optimized structure of CO_2-coordinated Mg-bound Ni complex. Reproduced from ref. 132 with permission from the American Chemical Society, Copyright 2019.

the choice of the appropriate metal implanted in the porphyrin moiety. The synergistic mode in these examples is the covalent connection of the catalytic center and photosensitive center, thus accelerating the electron transfer from the photosensitizing center to the catalytic center and boosting the CO_2 reduction.[134]

3.4.2 Electrocatalysis. Electrocatalytic CO_2 reduction into valuable fuels and chemicals over dinuclear metallic complex catalysts has also attracted considerable research interest.[135–139] In 2018, we designed and synthesized a dinuclear Ni complex, which can serve as an electrocatalyst for the reduction of CO_2 to CO. The TON and TOF values reached as high as 4.1×10^6 and 190.0 s^{-1}, respectively, which are 38-fold improvement of that of the corresponding mononuclear Ni complex. Moreover, the FE_{CO} was 95%, which is also higher than that of the mononuclear Ni complex (62%). The experimental observations together with DFT calculations demonstrated that the significantly improved catalytic efficiency for the electrochemical CO_2-to-CO conversion of the dinuclear Ni complex can be attributed to the DMSC effect between the two Ni centers.[135] Furthermore, Polyansky *et al.* prepared a mononuclear macrocyclic Co complex for electrocatalytic CO_2RR. A series of experimental characterizations and DFT calculations revealed that a bimetallic intermediate was *in situ* generated from two reduced mononuclear Co species bridged by a CO_2 molecule, which is more beneficial for the CO_2 reduction to CO compared with the mononuclear pathway.[136]

In addition to transition metal centers, the DMSC effect between dinuclear noble metal sites in the electrocatalytic CO_2RR has also been studied. For example, Jurss *et al.* designed and synthesized two anthracene-bridged dinuclear Re complexes with *cis*- and *trans*-conformers, as well as a mononuclear Re complex for electrocatalytic CO_2 reduction. The catalytic results showed that the dinuclear Re complex with *cis*-conformer achieved the TOF value of 35.3 s^{-1} for the reduction of CO_2 to CO, which is larger than that of the *trans*-conformer (22.9 s^{-1}) and mononuclear catalyst (11.1 s^{-1}) (Fig. 5a). The UV-vis spectroelectrochemical experiments indicated that a broad band at around 850 nm emerged for the *trans* conformer, suggesting the formation of an Re–Re bonded dimer (Fig. 5b). However, this signal was absent for the *cis*-conformer, implying there was no intermolecular Re–Re bond (Fig. 5c). Thus, the two Re centers in *cis*-conformer can bind a CO_2 *via* the synergistic mode.[137]

3.5 N_2RR

Photocatalytic or electrocatalytic N_2RR is now becoming a promising approach to producing ammonia under mild

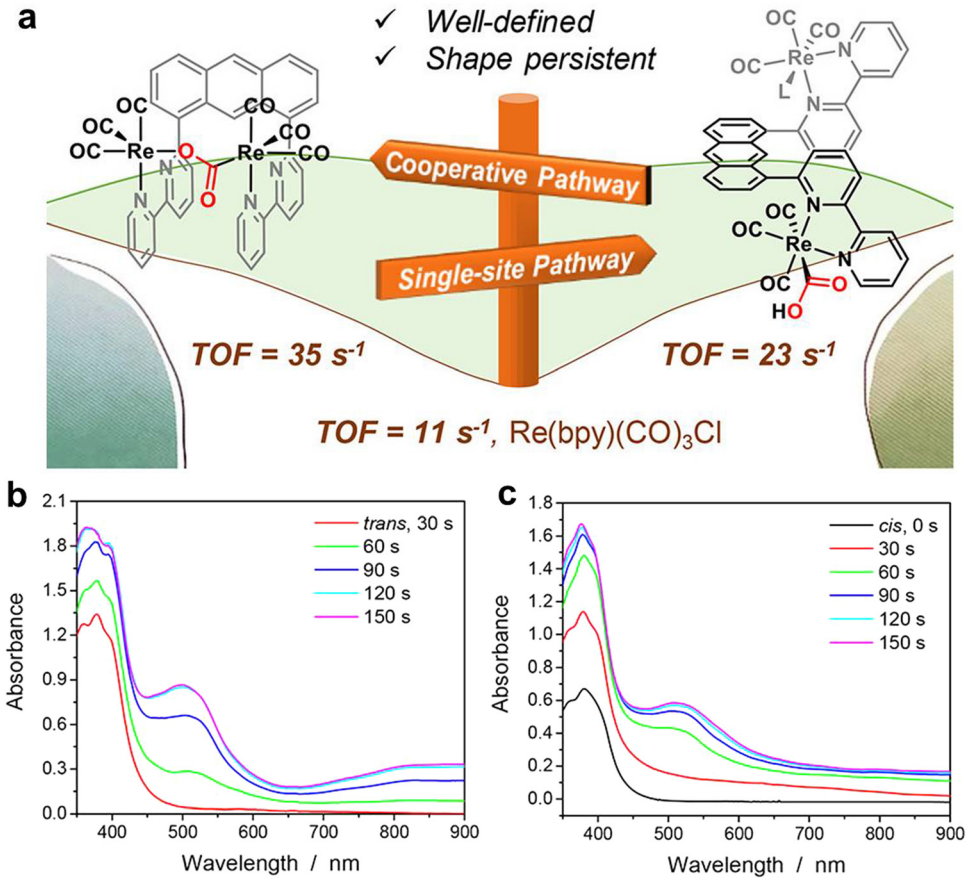

Fig. 5 (a) Illustration showing the dinuclear Re complex with *cis*-conformer for synergistic electrocatalytic CO_2 reduction to CO. UV-vis spectro-electrochemistry with 0.5 mM *cis*- (b) and *trans*- (c) Re_2Cl_2 at −1.7 V *vs.* Ag/AgCl in Ar-saturated DMF/0.1 M Bu_4NPF_6 solution. Reproduced from ref. 137 with permission from the American Chemical Society, Copyright 2018.

conditions. However, N_2 is thermodynamically stable owing to its extremely strong triple bond (941 kJ mol^{-1}), which requires highly efficient catalysts to achieve N_2RR.[140] Dinuclear metal complexes have been demonstrated as outstanding catalysts for the reduction of N_2 molecules. For example, Arnold *et al.* synthesized dinuclear uranium and thorium complexes with narrow cavities, which could bind N_2 molecules by two metal centers and mediate their reduction. In the presence of a weak acid and alkali metal reductant, the reactions produced ammonia at a slow reaction rate. When an excess of reductant and electrophile was added, this catalyst converted N_2 to a secondary silylamine. The bridging ligands may play a key role in controlling product formation because it can provide two protons to take part in N_2 reduction.[141] Furthermore, Schneider *et al.* constructed a dinuclear N_2-bridged rhenium complex, which was used as an excellent catalyst for the reduction of N_2 to benzamide/benzonitrile with an overall yield of 61%. A three-step cycle was demonstrated for N_2 reduction with a complex mechanism, involving rapid Re^{III}/Re^{II}-reduction, N_2-binding, halide loss, Re^{II}/Re^{I}-reduction, and Re^{I}/Re^{III}-comproportionation. The cooperating pincer ligand can act as a $2e^-/2H^+$ reservoir for nitrogen hydrogenolysis and electrochemical rehydrogenation to promote N_2 reduction.[142]

4. DMSC for energy conversion in heterogeneous catalytic systems

Besides homogeneous DMCs, heterogeneous DMCs have also been extensively studied for energy conversion reactions because of their superiority in terms of separation and recycling.[75,76] Thus, there are more corresponding reports on the latter. To date, many strategies have been developed to design and prepare heterogeneous DMCs to achieve efficient energy conversion. In this section, heterogeneous DMCs for photo-/electro-catalytic HER, OER, ORR, CO_2RR, and N_2RR will be reviewed and discussed. The contents in this section will also be divided into five parts.

4.1 HER

4.1.1 Photocatalysis. Heterogeneous photocatalytic water splitting to produce H_2 is a decades-old topic since the pioneering work of Fujishima and Honda, who found that a TiO_2 single crystal electrode can decompose water under illumination.[143] This aroused the interest of scientific and technological workers in photocatalytic water splitting. Many inorganic catalysts including metal oxides and sulfides have been developed.[144,145] Actually, besides inorganic catalysts, organic catalysts have also

been explored, where the typical example is graphitic carbon nitride (g-C_3N_4). g-C_3N_4 is a well-known non-metallic organic polymer semiconductor. It has attracted broad attention in energy conversion reactions, not only due to its own good photocatalytic performance, but also for its supporting function to stabilize metal active sites by abundant N atoms.[146] Accordingly, Li *et al.* fabricated an Fe–Co DMC for photocatalytic HER by loading Fe and Co single atoms on mesoporous g-C_3N_4 *via* a freeze-drying method. Aberration-corrected high-angle annular dark-field scanning transmission electron microscopy (HAADF-STEM) demonstrated that many bright spots were evenly distributed on mesoporous g-C_3N_4, which were identified as Fe and Co single atoms. The photocatalytic hydrogen production rate over Fe–Co DMC was 1958 μmol g^{-1}, which is 10 and 2.4 times higher than that of its monometallic Fe and Co counterparts, respectively. The significantly improved catalytic performance of Fe–Co DMC is attributed to the synergistic effect between Fe and Co.[147] Furthermore, Lei *et al.* constructed Co(II)-modified P-doped g-C_3N_4 nanosheets *via* a low-temperature phosphating method. In the photocatalytic HER process, Pt nanoparticles were *in situ* deposited on the nanosheets. The resulting catalyst exhibited excellent catalytic activity with a hydrogen production rate of 774 μmol g^{-1} h^{-1}, which is 8.6 times higher than that of pure g-C_3N_4 nanosheets. In the synergistic effect between Pt and Co, Pt serves as an electron transfer cocatalyst and Co acts as a hole transfer cocatalyst, thus promoting the separation of photogenerated e^- and h^+, and greatly boosting the photocatalytic HER activity.[148]

An *et al.* synthesized two heteronuclear Pt–Au DMCs for photocatalytic water splitting, which was achieved by dispersing Pt and Au atoms on TiO_2 with exposed {001} and {101} facets *via* a two-step deposition–precipitation method. Aberration-corrected HAADF-STEM of PtAu/{001}-TiO_2 showed numerous bright points, suggesting the even distribution of Au and Pt atoms. However, a few clusters were observed for PtAu/{101}-TiO_2. Normalized Pt L_3-edge X-ray absorption near-edge structure (XANES) spectroscopy demonstrated dominant peaks at ~1.6 Å for both PtAu/{001}-TiO_2 and PtAu/{101}-TiO_2, which can be assigned to Pt–O coordination. The Au L_3-edge XANES of PtAu/{001}-TiO_2 only showed the Au–O scattering path, whereas the characteristic peak of PtAu/{101}-TiO_2 is similar to Au foil, implying the existence of Au nanoparticles in PtAu/{101}-TiO_2. These results agree well with the HAADF-STEM results. The photocatalytic results showed that the H_2 evolution rate of PtAu/{001}-TiO_2 (61.3 mmol h^{-1} g^{-1}) is 4-times higher than that of PtAu/{101}-TiO_2 because the unsaturated Ti^{4+} in {001}-TiO_2 are prone to accommodate Pt and Au single atoms. Moreover, benefiting from the synergistic DMSC effect between Pt and Au, PtAu/{001}-TiO_2 achieved 3 and 5 times improvement in catalytic activity than that of its Pt/TiO_2 and Au/TiO_2 single-atom counterparts, respectively.[149] Zhou *et al.* prepared a Cu_1–Ti dual-site catalyst (Cu_1–Ti/TiO_2) by depositing atomic Cu on TiO_2 with abundant surface oxygen vacancies (Ti/TiO_2). The aberration-corrected HAADF-STEM image of Cu_1–Ti/TiO_2 showed some bright dots, implying the presence of isolated Cu atoms on the surface of Ti/TiO_2. The Cu K-edge spectrum in Fourier-transformed extended X-ray absorption fine structure (FT-EXAFS) exhibited a main peak at around 1.5 Å, which can be attributed to Cu–O coordination. No signal of Cu–Cu bond was detected, further suggesting that Cu atoms were single-atomically distributed. The catalytic results demonstrated that Cu_1–Ti/TiO_2 achieved superb activity for photocatalytic HER with an H_2 evolution rate of 3830 μmol g^{-1} h^{-1}, which is 7.3 and 26.6 times higher than that of Cu_1/TiO_2 and Ti/TiO_2, respectively. DFT calculations revealed that the introduction of Cu atoms offers active sites for the HER to promote the dissociation of water, thus boosting the catalytic performance.[150]

4.1.2 Electrocatalysis. Electrochemical HER provides a tangible approach to produce H_2, given that it can continuously generate clean H_2, where DMCs have been widely considered as promising electrocatalysts.[151–160] For instance, Cui *et al.* prepared tungsten atomic clusters anchored on P-doped carbon support using W single atoms as the parent material *via* a thermal migration strategy. The corresponding magnified HAADF-STEM images revealed numerous paired bright spots, which were identified as W_2 atom pairs. The *R*-space plots of the FT-EXAFS profiles presented a weak metal–metal peak, indicating the presence of W–W bonds. The results of alkaline electrochemical HER demonstrate that the synthesized tungsten atomic clusters display outstanding activity with an overpotential of 53 mV at 10 mA cm^{-2} and a Tafel slope of 38 mV dec^{-1}, which is a remarkable enhancement in HER activity with respect to both tungsten single atoms and tungsten carbide nanoparticles. DFT calculations revealed that the W–W dual-sites of the tungsten atomic clusters facilitate the desorption kinetics of the H* and OH* intermediates, thus accounting for the excellent alkaline HER activity.[151]

Beside W–W DMCs, studies showed that doping other metals can also form W-based heteronuclear DMCs for electrochemical HER. Fan *et al.* prepared a W–Mo DMC (W_1Mo_1-NG) with the W–O–Mo–O–C configuration *via* a facile two-step method. Specifically, the hydrothermal reaction of $Na_2WO_4 \cdot 2H_2O$, $(NH_4)_6Mo_7O_{24} \cdot 4H_2O$ and graphene oxide (GO) produced a precursor solution, which was further freeze-dried to produce a spongy column. Subsequently, the sponge column was treated by chemical vapor deposition (CVD) in NH_3/Ar gas at 800 °C to obtain the W_1Mo_1-NG DMC (Fig. 6a). The aberration-corrected HAADF-STEM image clearly showed some isolated heteronuclear W–Mo atoms with a distance of ~3.6 Å, which is much longer than the Mo–Mo/W–Mo/W–W bonds (~3.0 Å), suggesting that there are extra atoms to bridge W and Mo atoms (Fig. 6b and c). The results of FT-EXAFS spectroscopy and DFT calculations demonstrate that the heteronuclear W–Mo atoms are anchored in N-doped graphene by four O and two C atoms to form a W–O–Mo–O–C configuration (Fig. 6d). Consequently, the W_1Mo_1-NG DMC exhibited an excellent catalytic performance for electrochemical HER with an overpotential of 24 mV at the current density of 10 mA cm^{-2} in acidic electrolyte, which is lower than that of Mo_2 N-doped graphene (145 mV), W_2 N-doped graphene (156 mV), and pristine N-doped graphene (200 mV) electrocatalysts (Fig. 6e). DFT calculations further

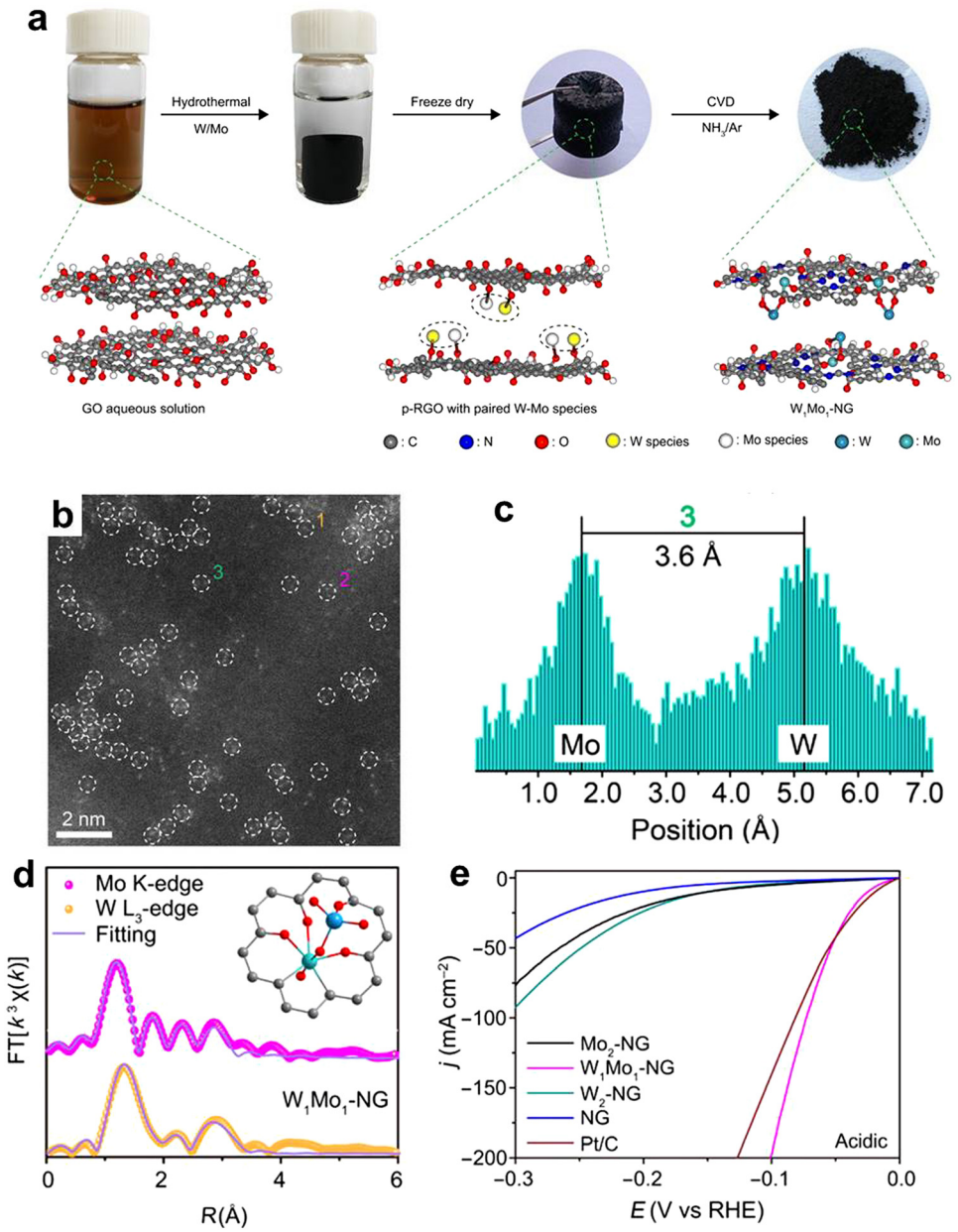

Fig. 6 (a) Schematic illustration showing the construction of W_1Mo_1-NG DMC. (b) Aberration-corrected HAADF-STEM images of W_1Mo_1-NG DMC. (c) Intensity profile obtained on one individual W–Mo dimer. (d) Corresponding Mo K-edge and W L_3-edge FT-EXAFS fitting curves for W_1Mo_1-NG in *R*-space. (e) Polarization curves of Mo_2-NG, W_1Mo_1-NG, W_2-NG, NG, and Pt/C in 0.5 M H_2SO_4. Reproduced from ref. 152 with permission from American Association for the Advancement of Science, Copyright 2020.

revealed that heteronuclear W–Mo DMC affords the desirable adsorption strength of H and good HER kinetics, thus facilitating the HER process.[152]

In 2019, Luo *et al.* designed and synthesized Cr-doped Co_4N nanorod arrays on carbon cloth for electrocatalytic HER in alkaline electrolyte. The obtained material displayed promising catalytic activity with an overpotential of 21 mV at the current density of 10 mA cm^{-2}, which is much better than the commercial Pt/C electrocatalyst. DFT calculations together with experimental results revealed that the introduction of Cr increased the H_2O adsorption and dissociation ability, which is beneficial for both the alkaline Volmer and Heyrovsky steps, thus leading to the high performance.[153] Moreover, Chen *et al.* developed a facile method to construct a conductive bimetallic electrocatalyst by the introduction of Co atoms in conductive Cu-catecholate nanorod arrays on carbon cloth for the HER. The catalytic results demonstrated that the synthesized bimetallic electrocatalyst exhibited excellent activity with overpotentials of 52 and 143 mV at a current density of 10 mA cm^{-2} in alkaline and neutral media, respectively, which is significantly lower than that of the benchmark Pt/C electrocatalyst. DFT calculations revealed that Co doping can optimize the

adsorption energies of both water and hydrogen, facilitating the Volmer step in the HER process.[154]

Pt has been regarded as the most efficient catalyst for the HER, but its high cost limits its large-scale applications. Accordingly, the integration of Pt and other metals to form DMCs is a promising strategy to lower the use of Pt and enhance the catalytic efficiency of Pt-based catalysts. For instance, Yao *et al.* fabricated a Co–Pt DMC with 0.16 wt% of Pt by annealing a cobalt-based MOF and dicyandiamide. This catalyst displayed ultrahigh activity for electrochemical HER with an overpotential of only 27 mV in acidic media and 50 mV in alkaline media at 10 mA cm^{-2}, which are superior to that of the commercial Pt/C (59 mV and 65 mV, respectively). The excellent catalytic performance of Co–Pt DMC was attributed to the synergistic effect of atomic Pt and Co, which induced charge polarization around the atomic Co and lowered the Gibbs free energy change of the intermediates, thus boosting the catalytic activity, as supported by DFT calculation.[155] Moreover, Qian *et al.* prepared well-dispersed PtNi alloy nanoparticles implanted on N-doped carbon *via* the carbonization of polyaniline-containing Pt and Ni ions. The transmission electron microscopy (TEM) image demonstrated that numerous PtNi nanoparticles were anchored on the surface of the carbon substrate with a size of ~6.5 nm. The electrocatalytic results showed that the optimized PtNi catalyst displayed an outstanding HER performance with the current density of 3.78 A mg_{Pt}^{-1} in 1.0 M KOH, which is 13-times higher than that of the benchmark 20% Pt/C catalyst. DFT computations revealed that the incorporation of Pt and Ni elements could help modify their mutual electron distributions and d-band center positions to promote the dissociation of $*H_2O$, thereby enhancing the HER activity.[156]

Besides, Li *et al.* synthesized a Pt–Cu DMC containing 1.5 atom% Pt *via* a two-step approach for electrocatalytic HER. Firstly, atomically dispersed Cu on Pd nanosheets was prepared by adding $CuCl_2{\cdot}2H_2O$ aqueous solution to Pd nanosheets; then the mixture was injected into K_2PtCl_4 solution to obtain the Pt–Cu DMC. The Pt L_3-edge FT-EXAFS spectrum showed two main peaks at 2.05 and 2.56 Å, which can be assigned to Pt–Cu and Pt–Pd paths, respectively. These results suggest the presence of Pt–Cu dual sites on the Pd nanosheets. Electrochemical tests showed that the Pt–Cu DMC exhibited outstanding HER activity, with an overpotential of 22.8 mV at 10 mA cm^{-2} and mass current density of 3002 A $g^{-1}_{(Pd+Pt)}$ at −0.05 V (*vs.* RHE).[157] Sun *et al.* prepared Pt–Ru dimers with 0.9 wt% of Pt *via* a two-step ALD process for electrocatalytic HER. As shown in Fig. 7a, the Pt single atoms were first deposited onto N-doped carbon nanotubes (NCNTs) using trimethyl(methylcyclopentadienyl) platinum ($MeCpPtMe_3$) as the precursor for ALD. The aberration-corrected HAADF-STEM image indicated a large number of Pt atoms anchored on NCNTs. Subsequently, the deposition of Ru atoms on the Pt single atoms to form Pt–Ru dimers was achieved by ALD using bis(ethylcyclopentadienyl)ruthenium as the precursor. The aberration-corrected HAADF-STEM revealed a number of paired bright and dark spots, implying that Pt–Ru dimers were constructed (Fig. 7b and c), as further confirmed *via* X-ray absorption spectroscopy. The prepared Pt–Ru dimers showed higher catalytic activity for the HER than Pt single atoms and commercial Pt/C catalysts (Fig. 7d and e). DFT calculations revealed that the synergetic effect between Pt and Ru modulates the electronic structure, resulting in the high HER performance.[158]

4.2 OER

It is well-known that the OER is the bottleneck of water splitting owing to the four-electron- and proton-transfer steps, which requires efficient and stable catalysts to achieve this half reaction. A series of heteronuclear DMCs demonstrated that dinuclear metal sites can overcome the obstacles and promote

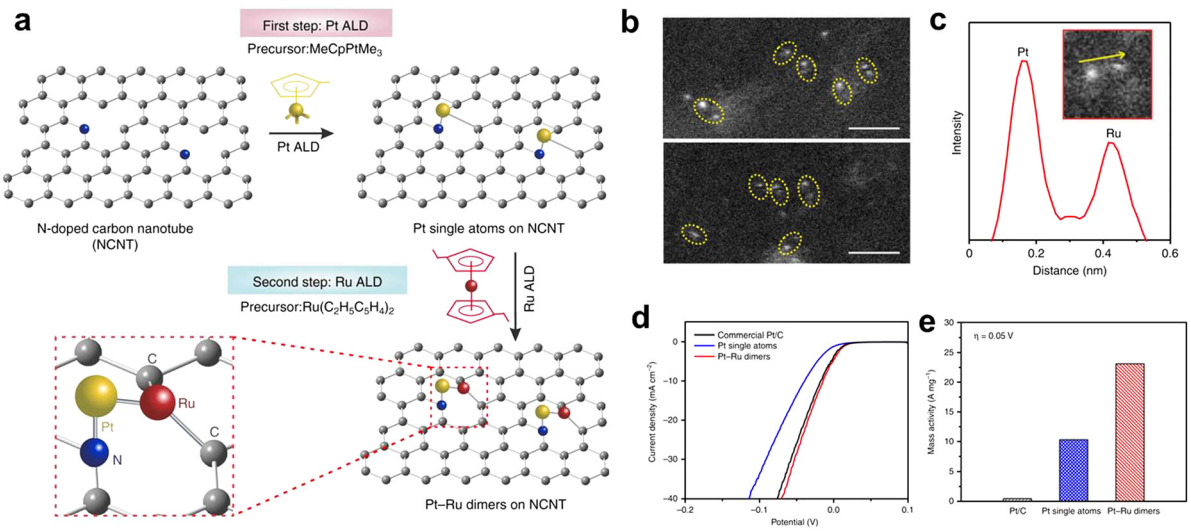

Fig. 7 (a) Schematic illustration showing the synthesis of Pt–Ru dimers on NCNTs by ALD process. (b) Aberration-corrected HAADF-STEM images of Pt–Ru dimers/NCNTs. Scale bars: 1 nm. (c) Intensity profile obtained on one individual Pt–Ru dimer. (d) HER curves and (e) normalized mass activity at 0.05 V (*vs.* RHE) of Pt–Ru dimers, Pt single atoms and Pt/C catalysts. Reproduced from ref. 158 with permission from Springer Nature, Copyright 2019.

electrocatalytic OER.[161–179] In 2019, Hu *et al.* synthesized an Fe–Co DMC *via* an *in situ* electrochemical method for the OER. Firstly, a single-atom Co precatalyst (Co–N–C) was prepared by calcining a mixture of Co complex, phenanthroline and $Mg(OH)_2$, in which $Mg(OH)_2$ was used as a template and dispersing reagent. Then, Co–N–C was tested for the OER in 1 M KOH solution with and without $Fe(NO_3)_3{\cdot}9H_2O$. The catalytic results demonstrated that the overpotential is 495 mV at 10 mA cm^{-2} in Fe-free KOH solution, whereas it is 308 mV at 10 mA cm^{-2} in Fe-containing KOH solution. A series of experimental characterizations (XAS, in particular) revealed that Fe was electrochemically incorporated in Co–N–C to yield an Fe–Co double-atom catalyst, which consisted of Fe–Co active sites for the OER. The significantly enhanced catalytic activity of the Fe–Co catalyst over the single-atom Co catalyst can be attributed to the synergetic effect between Fe and Co.[161] In addition, Bu *et al.* constructed an Fe–Co DMC embedded in N-doped graphitic carbon by high-temperature annealing ZIF-8 containing bimetallic phthalocyanines macromolecules (FeCoPc). The aberration-corrected HAADF-STEM image demonstrated many paired bright spots, which can be assigned to Fe–Co atom pairs. The FT-EXAFS of Fe–Co DMC at Fe and Co K-edges only displayed Fe–N and Co–N scattering paths, suggesting the atomic dispersion of Fe and Co. The catalytic results showed that the Fe–Co DMC exhibited outstanding activity for the OER in N_2-saturated 1.0 M KOH, with an overpotential of 370 mV at 10 mA cm^{-2}, much lower than that of Fe MMC (440 mV) and Co MMC (398 mV). DFT calculations demonstrated that the synergetic effect between Fe and Co optimized the d-band center position of the metal sites and lowered the energy barrier of the RDS, thereby improving the OER performance.[162] Xu *et al.* also designed and synthesized an Fe_2Co DMC using the classical host–guest delocalization strategy. The Fe_2Co trinuclear metal complex was first immobilized on a zinc-based MOF precursor, followed by pyrolysis of Fe_2Co@MOF to form Fe_2Co DMC. In the aberration-corrected HAADF-STEM image, some paired and isolated spots were observed, corresponding to the dual iron atoms and single Co atoms, respectively, as further confirmed *via* EELS. The electrochemical measurements demonstrated that the Fe_2Co DMC had good catalytic activity for the OER with an overpotential of 350 mV at 10 mA cm^{-2}, which is much lower than that of the Fe_3 catalyst (447 mV), FeCo DMC (>480 mV) and IrO_2 (420 mV).[163]

Besides Fe–Co, Fe–Ni DMCs have also been investigated for electrocatalytic OER. In 2018, Sun *et al.* prepared a series of Fe–Ni DMCs (Ni-MOF@Fe-MOF) with different Ni/Fe atomic ratios by decorating hybrid Ni-based MOF nanosheets with Fe-MOF nanoparticles for the OER. Compared with the pure Ni-based MOF, the catalytic activity dramatically increased after the introduction of Fe-MOF nanoparticles. The optimal catalytic activity was achieved with an Ni/Fe atomic ratio of 3.5/1, with an overpotential of 265 mV at 10 mA cm^{-2} in 1 M KOH. This overpotential is much lower than that for Ni-MOF (370 mV) and IrO_2 (365 mV). The current density of Ni-MOF@Fe-MOF was 12.8 mA cm^{-2} at 1.50 V (*vs.* RHE), which is 10-times higher than that of Ni-MOF (1.0 mA cm^{-2}). During the OER process, NiO nanograins with the size of ~5 nm were observed in the HRTEM image, which acted as OER active centers. The high catalytic performance of Ni-MOF@Fe-MOF is due to the synergistic effect between the Ni active centers and Fe species.[164] Furthermore, Peng *et al.* synthesized Fe/Ni single atoms embedded in an N-doped carbon (NC) matrix (FeNi SAs/NC) by annealing FeNi-MOF with coated polydopamine (PDA), following by acid etching to remove the Fe and Ni nanoparticles, forming Fe–Ni DMCs for electrocatalytic OER (Fig. 8a). The aberration-corrected HAADF-STEM image evidenced the existence of Fe–Ni atomic pairs (Fig. 8b). The FT-EXAFS spectrum of Fe K-edge of FeNi SAs/NC in the *R*-space showed two strong peaks at 1.50 and 2.27 Å, which were assigned to the Fe–N and Fe–Ni bonds, respectively (Fig. 8c). XANES together with DFT calculations further confirmed an $Fe–Ni–N_6$ structure in this heteronuclear DMC. The prepared Fe–Ni DMC exhibited a high performance for the OER, with a low overpotential of 270 mV at 10 mA cm^{-2}, which is much lower than that of FeNi NPs/NC (290 mV), NC (350 mV) and RuO_2 (310 mV) (Fig. 8d). DFT calculations further demonstrated that the Ni sites modulated the electronic structure of the Fe active center, which facilitated the four-electron transfer process and lowered the energy barrier of the RDS, thus improving the catalytic efficiency (Fig. 8e).[165] Also, Duan *et al.* constructed an Fe–Ni dual-site catalyst *via* the pyrolysis of ZIF-8 containing Fe^{3+} and Ni^{2+} ions through a theory-guided atomic design and fabrication strategy. The aberration-corrected HAADF-STEM images demonstrated the formation of Fe–Ni dual sites. The FT-EXAFS spectrum of Fe displayed two main peaks at 1.52 and 2.48 Å, and these for Ni were 1.58 and 2.44 Å, implying the co-existence of Fe–N, Ni–N and Fe–Ni bonds. The obtained Fe–Ni DMC exhibited excellent OER activity with an overpotential of 395 mV at 10 mA cm^{-2}, which is superior to that for Fe and Ni MMCs. DFT calculations revealed that the activation of OH* and O* occurs on the Fe and Ni sites, respectively, and the synergistic effect between Fe and Ni regulates the OOH* formation energy of the RDS, thus facilitating the OER process.[166]

Other Fe-based DMCs were also developed for electrochemical OER. Wang *et al.* constructed an ultrathin 2D Fe–Mn DMCs by pyrolysis of ZIF-8 encapsulating Fe^{3+} and Mn^{2+} ions with the assistance of the $KCl/ZnCl_2$ eutectic salt. Aberration-corrected HAADF-STEM showed numerous evenly distributed bright spots, among which 62% were paired spots, corresponding to the Fe–Mn dual atoms. The Fe and Mn K-edge FT-EXAFS spectra showed the primary peaks at ~1.5 Å, which can be assigned to the Fe–N and Mn–N scattering paths, respectively. No metal–metal scattering peak was detected, suggesting the presence of atomically dispersed Fe and Mn on the 2D nanosheet. The Fe–Mn DMC showed excellent OER activity with an overpotential of 405 mV at 10 mA cm^{-2}, which is lower than that of Fe (496 mV) and Mn (525 mV) MMCs.[167] In addition, Shen *et al.* prepared Fe- and Mo-modified $Ni(OH)_2$/NiOOH (FeMo:$Ni(OH)_2$/NiOOH) nanosheets grown on commercial nickel foam for the OER. FeMo:$Ni(OH)_2$/NiOOH gave a current density of 134.5 mA cm^{-2} at 1.53 V (*vs.* RHE), which

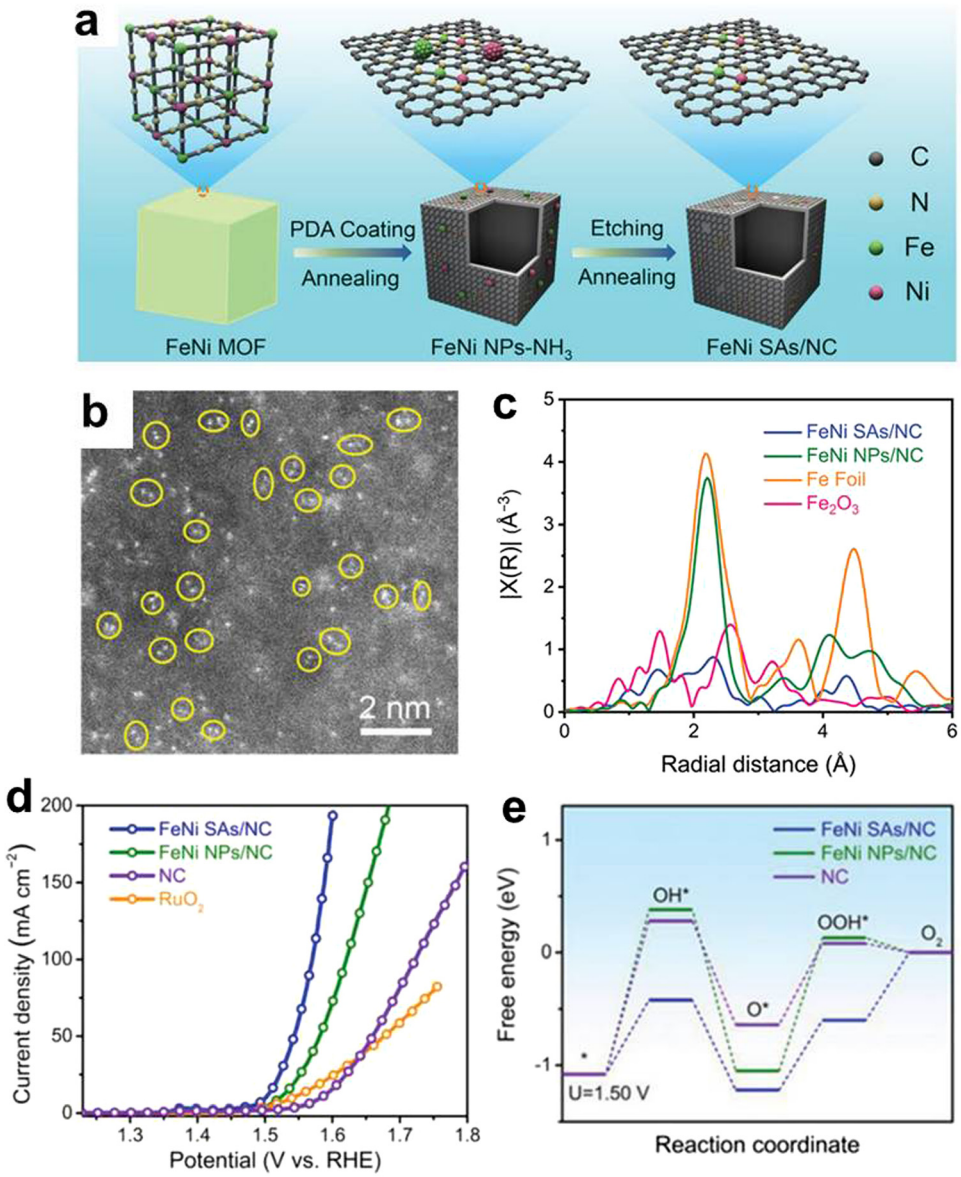

Fig. 8 (a) Schematic illustration showing the synthesis of FeNi SAs/NC. (b) Aberration-corrected HAADF-STEM images of FeNi SAs/NC. (c) FT-EXAFS spectra of the Fe K-edge of FeNi SAs/NC, FeNi NPs/NC, Fe foil, and Fe_2O_3. (d) OER LSV curves of FeNi SAs/NC, FeNi NPs/NC, NC, and Pt/C in 1.0 M KOH. (e) Free energy diagrams of different OER intermediates OH*, O*, and OOH* at 1.50 V. Reproduced from ref. 165 with permission from Wiley-VCH, Copyright 2021.

is much higher than that of Fe:$Ni(OH)_2$/NiOOH (49.2 mA cm^{-2}), Mo:$Ni(OH)_2$/NiOOH (18.5 mA cm^{-2}), and $Ni(OH)_2$/NiOOH (12.8 mA cm^{-2}). Furthermore, FeMo:$Ni(OH)_2$/NiOOH only required an overpotential of 280 mV to achieve a current density of 100 mA cm^{-2} and maintained long-term stability over 50 h at this high current density. A series of experiment results confirmed the presence of a synergistic effect between Fe and Mo to improve both the activity and stability.[168]

In addition to Fe-based DMCs, Co-based DMCs have also attracted considerable attention for electrochemical OER. In 2019, Hu *et al.* fabricated a Co–Ni DMC by annealing a CoNi-based MOF and polydopamine, followed by acid leaching to remove Co and Ni nanoparticles. The aberration-corrected HAADF-STEM image revealed numerous isolated bright spots, corresponding to Co and Ni single atoms. The Co and Ni K-edge FT-EXAFS spectra demonstrated the major peaks located at approximately 1.49 and 2.22 Å, which can be assigned to the Co–N/Ni–N and Co–Ni bonds, respectively. The resulting Co-Ni DMC displayed good electrocatalytic activity for the OER, with the required overpotential of 340 mV at 10 mA cm^{-2}, which is lower than that of the corresponding Co–Ni nanoparticles (440 mV) and IrO_2 (400 mV). Experimental and theoretical investigations revealed that the synergistic effect between the Co and Ni atoms lowered the energetic barrier and promoted the reaction kinetics, thereby enhancing the catalytic activity.[169] Moreover, Lou *et al.* prepared an atomically dispersed Ni and Co

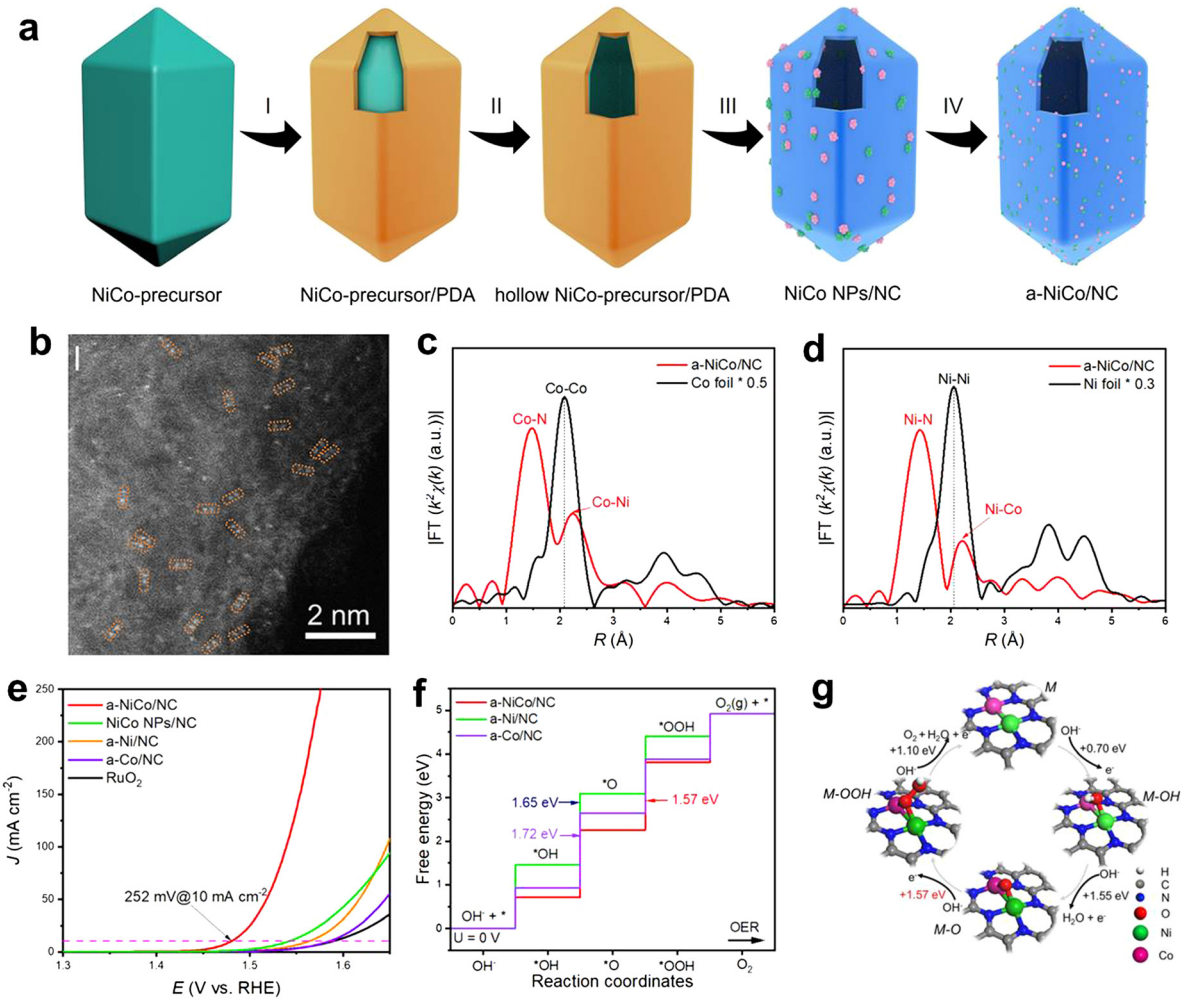

Fig. 9 (a) Schematic illustration showing the synthesis of a-NiCo/NC by multi-step templating strategy. (b) Aberration-corrected HAADF-STEM image of a-NiCo/NC. FT-EXAFS spectra of Co (c) and Ni (d) K-edges of a-NiCo/NC. (e) LSV plots of a-NiCo/NC, a-Ni/NC, a-Co/NC, NiCo and RuO_2. (f) Free energy diagram of a-NiCo/NC, a-Ni/NC, and a-Co/NC for the OER. (g) Optimized OER catalytic pathways of a-NiCo/NC. Reproduced from ref. 170 with permission from Wiley-VCH, Copyright 2022.

dual-site catalyst *via* a multi-step templating strategy for the OER. As shown in Fig. 9a, a thin polydopamine (PDA) layer was first coated on the surface of the NiCo-based acetate hydroxide precursor by the self-polymerization of dopamine. Then, the inner NiCo-precursor cores were partially etched to generate a hollow NiCo-precursor/PDA composite. Subsequently, the composite was carbonized at low temperature, and then NiCo nanoparticles were removed by an acidic solution to obtain the Co and Ni dual-site catalyst (a-NiCo/NC). The aberration-corrected HAADF-STEM image demonstrated atomically dispersed Ni and Co atoms, in which many atomic pairs are observed, suggesting the possible Ni–Co dual-metal sites (Fig. 9b). The FT-EXAFS of Co and Ni K-edges showed that the peaks at 1.42, 1.47 and 2.23 Å are assigned to Ni–N, Co–N and Ni–Co bonds, respectively (Fig. 9c and d). The obtained a-NiCo/NC exhibited outstanding OER activity, with an overpotential of 252 mV at 10 mA cm^{-2} in 1.0 M KOH, which is much lower than that of the corresponding a-Ni/NC (333 mV) and a-Co/NC (354 mV) single-atom catalysts, as well as NiCo nanoparticles (312 mV) and RuO_2 (358 mV) (Fig. 9e). It also showed long-term durability over 150 h. DFT calculations demonstrated that the strong synergistic interaction between the Ni and Co sites lowered the reaction energy barrier, thus boosting the catalytic activity (Fig. 9f and g).[170]

Besides transition metals, a variety of noble metal iridium-based DMCs have also been developed for electrocatalytic OER. For example, Wang *et al.* synthesized an Ir–Co DMC by trapping Ir single atoms on Co nanosheets with 1.7 wt% Ir. The aberration-corrected HAADF-STEM image showed many bright spots, which can be assigned to the Ir single atoms. The FT-EXAFS of Ir L-edge in *R* space showed a major peak at ~2.20 Å, which is shorter than that of the Ir–Ir bond (2.47 Å), suggesting the formation of Ir–Co bonds. The prepared Ir–Co DMC displayed good OER activity, with an overpotential of 273 mV at 10 mA cm^{-2}, which is lower than that of Ir/C (290 mV) and Co nanosheets (393 mV). DFT calculations in combination with experiments revealed that the cooperation of Ir–Co dual sites is beneficial for stabilizing the OOH* intermediate *via* hydrogen bonding, thus expediting the OER process.[171] Moreover,

Chen *et al.* prepared a diatomic Ir–Co catalyst by pyrolyzing an Ir-impregnated ZnCo-ZIF under a flowing Ar/H_2 atmosphere. The aberration-corrected HAADF-STEM image demonstrated some bright dual dots, corresponding to the dinuclear metal configuration. The FT-EXAFS spectra of Co K-edge and Ir L-edge displayed major peaks at 1.44 and 1.64 Å, which can be assigned to the Co–N and Ir–N paths, respectively. The Ir–Co bond was also detected at 2.11 Å in the Ir L-edge spectrum. The Ir–Co catalyst exhibited promising OER activity with an overpotential of 330 mV at 10 mA cm^{-2} in 0.1 M KOH, which is 69 and 47 mV lower than that of the corresponding Co and Ir MMCs, respectively, and even 21 mV more negative than that for the Ir/C benchmark. Theoretical calculations revealed that the incorporation of Ir atom modulated the Co d-orbital electron configuration, resulting in faster reaction kinetics.[172]

4.3 ORR

The ORR involves two types of processes, *i.e.*, four-electron transfer to generate H_2O and two-electron transfer to form H_2O_2.[180,181] Both processes need efficient catalysts, and thus numerous heterogeneous homo- and heteronuclear DMCs have been developed.[182–220]

4.3.1 Homonuclear DMCs. In 2019, Xiong *et al.* designed and synthesized an Fe_2 DMC *via* the pyrolysis of ZIF-8 containing dinuclear $Fe_2(CO)_9$ and used this catalyst for electrocatalytic ORR in acidic electrolyte. The aberration-corrected HAADF-STEM image showed numerous bright paired spots, which were assigned to the Fe_2 dimers. The FT-EXAFS spectrum of Fe K-edge revealed a major peak at ~1.50 Å and minor peak at 2.46 Å, which can be ascribed to Fe–N and Fe–Fe bonds, respectively. The synthesized Fe_2 DMC exhibited outstanding ORR activity in 0.5 M H_2SO_4 solution with a half-wave potential ($E_{1/2}$) of 0.78 V (*vs.* RHE), which is 65 mV higher than that of the corresponding Fe MMC.[182] Furthermore, Xie *et al.* prepared a planar-like Fe_2N_6 DMC *via* thermal treatment of hemin molecules with the typical FeN_4 structure. The aberration-corrected HAADF-STEM images revealed a large number of bright dots, most of which were in pairs, corresponding to Fe_2 dimers. The planar-like Fe_2N_6 coordination structure was further confirmed *via* XAS. The FT-EXAFS spectrum of the Fe K-edge showed a major peak at 1.39 Å and minor peak at 2.19 Å, corresponding to Fe–N/O and the Fe–Fe shell, respectively. The planar-like Fe_2N_6 DMC displayed high ORR activity with $E_{1/2}$ of 0.84 V (*vs.* RHE), which is higher than that for FeN_4 MMC (0.76 V *vs.* RHE). It also achieved a large peak power density of 845 mW cm^{-2} in proton-exchange membrane fuel cell systems. DFT calculations revealed that the synergic effect between two adjacent Fe_2 atoms of Fe_2N_6 DMC accelerated the catalytic kinetics, thereby promoting the catalytic activity.[183]

In addition, Xing *et al.* designed and elaborated three Co_2N_5 DMCs by pyrolyzing ZnCo-ZIF with different molar ratios of Zn/Co for the ORR. Upon the evaporation of Zn at high temperature, the optimized Co_2N_5 DMC exhibited bright adjacent spots in the aberration-corrected HAADF-STEM image with the distance of 2.1–2.2 Å, suggesting the formation of dinuclear sites. The FT-EXAFS spectrum of Co K-edge further confirmed the presence of Co–N and Co–Co bonds. The prepared Co_2N_5 DMC displayed excellent ORR activity with $E_{1/2}$ of 0.79 V (*vs.* RHE), which is 12-times higher than the conventional CoN_4 catalyst. Theoretical calculations revealed that the dinuclear metal sites of the Co_2N_5 DMC promoted the reaction of $*OH \rightarrow H_2O$, resulting in the high catalytic activity.[184]

4.3.2 Heteronuclear DMCs

4.3.2.1 Fe–Co DMCs. In 2017, by the pyrolysis of Co/Zn-ZIF with adsorbed Fe ions, Wu *et al.* obtained an Fe–Co DMC for the ORR in acidic electrolyte. Numerous evenly distributed bright dual dots were observed in the aberration-corrected HAADF-STEM images, which were assigned to the Fe and Co atomic pairs. The FT-EXAFS spectra showed Fe–N, Co–N and Fe–Co scattering paths, further implying the presence of Fe–Co dual sites. The obtained Fe–Co DMC displayed a superior ORR performance with $E_{1/2}$ of 0.863 V (*vs.* RHE), which is superior to Fe and Co MMCs. It also exhibited long-term stability over 50 000 cycles for electrode measurement and 100 h for H_2/air single cell operation. DFT calculations revealed that the outstanding catalytic activity of the Fe–Co DMC is due to the synergistic effect between the Fe and Co sites, which is beneficial for the activation of the O–O bond.[185] Using the same strategy, Xing *et al.* synthesized an Fe–Co DMC ($FeCoN_5$-OH) by pyrolyzing Co/Zn-ZIF containing $Fe(acac)_3$ molecules (acac = acetylacetonate). The aberration-corrected HAADF-STEM images revealed some bright paired dots with the distance of 2.2–2.3 Å, corresponding to the Fe–Co dual-atom sites. The EELS data showed atomically distributed Fe and Co atoms located adjacent to N atoms, further verifying the presence of Fe–Co dual-atom sites. The FT-EXAFS curves of this DMC showed primary peaks at ~1.5 Å, corresponding to Fe–N and Co–N scattering paths, and no Co–Co, Fe–Fe, and Fe–Co scattering paths were detected. The catalytic results demonstrated that $FeCoN_5$-OH displayed excellent ORR activity with $E_{1/2}$ of 0.86 V (*vs.* RHE), with an intrinsic activity over 20 times higher than that of the FeN_4 single site. DFT calculations revealed that the electron-withdrawing OH ligand adsorbs on the Fe–Co dual centers to form triangle $FeCoN_5$-OH sites, which tailor their electronic structure to facilitate O–O bond cleavage.[186]

Xu *et al.* fabricated another Fe–Co DMC (FeCo@C) for electrocatalytic ORR *via* the one-step pyrolysis of Zn-based MOF with Fe and Co ions. The aberration-corrected HAADF-STEM and energy-dispersive X-ray spectroscopy (EDS) mapping images indicated the existence of Fe and Co atomically dispersed metal sites. The Fe and Co K-edge FT-EXAFS spectra exhibited the main peak at ~1.5 Å, corresponding to Fe–N and Co–N bonds. The absence of Co–Co, Fe–Fe, and Fe–Co scattering paths further confirmed atomically dispersed Fe and Co atoms. The obtained FeCo@C showed high ORR activities in both alkaline and acidic electrolyte. In 0.1 M KOH, FeCo@C exhibited a more positive onset potential (E_{onset}) and $E_{1/2}$ than that of the commercial Pt/C. FeCo@C also displayed high ORR activity in 0.5 M H_2SO_4, which is close to that for Pt/C.[187] In addition, Bu *et al.* proposed a ''pre-constrained metal twin'' strategy to construct a contiguous FeN_4 and CoN_4 DMC (FeCo-DACs/NC). In this work, the bimetallic phthalocyanine

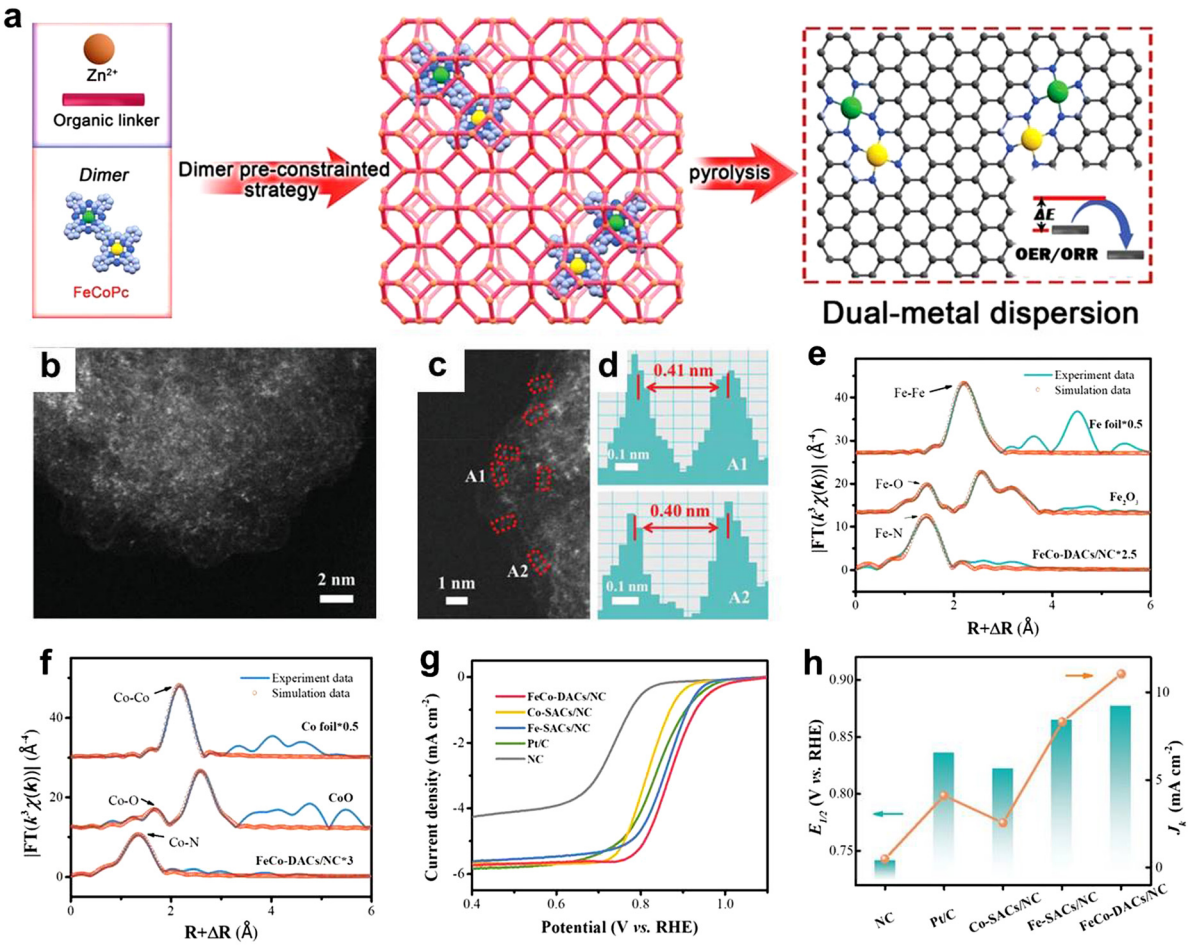

Fig. 10 (a) Schematic illustration showing the construction of FeCo-DACs/NC *via* the "pre-constrained metal twin" strategy. (b and c) Aberration-corrected HAADF-STEM images of FeCo-DACs/NC. (d) Intensity profiles obtained for two metals. FT-EXAFS spectra of Fe (e) and Co (f) K-edges of FeCo-DACs/NC. (g) LSV plots and (h) comparison of $E_{1/2}$ and J_k of FeCo-DACs/NC, Fe-MMC/NC, Co-MMC/NC, Pt/C and N–C. Reproduced from ref. 162 with permission from Wiley-VCH, Copyright 2022.

macromolecules (FeCoPc) were first implanted *in situ* in ZIF-8 to form a composite. Then, the high-temperature annealing of the composite generated the Fe–Co DMC embedded in N-doped graphitic carbon (Fig. 10a). Aberration-corrected HAADF-STEM images showed numerous bright spots, corresponding to Fe and Co atoms (Fig. 10b), among which some dispersed metal pairs were observed with the distance of ~0.4 nm (Fig. 10c and d). The FT-EXAFS spectra of FeCo-DACs/NC at Fe and Co K-edges only demonstrated dominant peaks at 1.44 and 1.36 Å, which can be attributed to the Fe–N and Co–N scattering paths, and no signals of metal–metal bonds were detected, implying the atomic distribution of Fe and Co atoms (Fig. 10e and f), respectively. The resulting FeCo-DACs/NC exhibited outstanding ORR activity with an E_{onset} of 0.984 V (*vs.* RHE) and $E_{1/2}$ of 0.877 V (*vs.* RHE), which are better than that of Fe-MMC/NC (0.943 and 0.865 V), Co-MMC/NC (0.909 and 0.822 V), commercial Pt/C (0.962 and 0.836 V) and NC (0.825 and 0.741 V) (Fig. 10g and h), respectively. Impressively, the kinetic current density (J_k) of FeCo-DACs/NC was the largest among the catalysts (Fig. 10h). Theoretical calculations demonstrated the synergistic effect between the Fe and Co atoms, which modulated the d-band center position of the metal centers and optimized the free energy of the *O intermediate, thereby resulting in improved catalytic activity.[162]

Besides, Luo *et al.* prepared an FeCo–N-doped hollow carbon catalyst (FeCo–N-HCN) with neighbouring Fe–N_4–C and Co–N_4–C dual metal sites *via* the polymerization of pyrrole on porous FeCo oxides followed by pyrolysis. The aberration-corrected HAADF-STEM images revealed some bright dots of single Fe or Co atoms, among which the neighboring Fe and Co atomic pairs were also observed with the distance of ~0.5 nm. The presence of the Fe and Co atomic pair was further confirmed *via* EELS because the signals for Fe (707.0 eV) and Co (798.0 eV) atoms were detected. The FT-EXAFS spectra of FeCo–N-HCN at Fe and Co K-edges showed main peaks at ~1.5 Å, corresponding to Fe/Co–N bonds, and no metal–meal bonds were identified, suggesting that the Fe and Co atoms were atomically dispersed. The electrocatalytic results showed that FeCo–N-HCN displayed superior ORR activity with E_{onset} and $E_{1/2}$ of 0.98 and 0.86 V (*vs.* RHE) in 0.1 M KOH solution, which are more positive than that of Fe–N-HCM MMC (0.96 and 0.76 V *vs.* RHE), respectively. The enhanced catalytic performance of FeCo–N-HCN is attributed to the synergistic effect of Fe and

Co dual active centers, which lowered the reaction energy barriers for the ORR.[188] Fu *et al.* also designed and synthesized an Fe–Co DMC (Fe, Co SAs-PNCF) by pyrolyzing a mixture of Fe/Co complexes, polyacrylonitrile and ZnO nanoparticles in an N_2 atmosphere. The aberration-corrected HAADF-STEM images showed distributed Fe–Co dual-metal single atoms with a distance of 0.23 nm, as further verified *via* EELS. The FT-EXAFS spectra of the Fe and Co K-edges displayed prominent peaks at 1.50 and 1.30 Å, corresponding to Fe–N and Co–N coordination, respectively, and no signals of metal–metal bonds were found, implying the atomic dispersion of Fe and Co in this catalyst. The obtained Fe, Co SAs-PNCF displayed high ORR activities in both alkaline and acidic media. In 0.1 M KOH solution, the E_{onset} and $E_{1/2}$ for the Fe, Co SAs-PNCF were 1.04 and 0.93 V (*vs.* RHE), which are more positive than that for Fe (1.00 and 0.89 V *vs.* RHE) and Co (0.96 and 0.83 V *vs.* RHE) MMCs, respectively. In 0.1 M $HClO_4$ solution, the E_{onset} and $E_{1/2}$ of Fe, Co SAs-PNCF were 0.94 and 0.0.78 (*vs.* RHE), respectively, which are also superior to that of Fe and Co MMCs. Theoretical calculations demonstrated that the synergistic effect of the Fe and Co single-atom sites lowered the energy barrier for O* dissociation, thus promoting the ORR activity.[189]

4.3.2.2 Fe–Ni DMCs. In 2021, Peng *et al.* reported the preparation of a bimetallic MOF-derived Fe–Ni DMC (denoted as FeNi SAs/NC) for the ORR. Firstly, the bimetallic FeNi-MOF was coated by polydopamine through the *in situ* polymerization of dopamine to form a composite. Subsequently, the pyrolysis of this composite under NH_3 followed by acid etching and further annealing process generated FeNi SAs/NC. The aberration-corrected HAADF-STEM image revealed many bright dots, which were attributed to the isolated Fe and Ni atoms, among which some Fe–Ni atomic pairs were also observed. The FT-EXAFS spectrum of the Fe K-edge presented two strong peaks at 1.50 and 2.27 Å, and similar results were found in the Ni K-edge spectrum, suggesting the existence of Fe–N, Ni–N and Fe–Ni bonds. The prepared FeNi SAs/NC exhibited extraordinary ORR activity with E_{onset} and $E_{1/2}$ of 0.98 and 0.84 V (*vs.* RHE), respectively, in alkaline media, superior to that of FeNi NPs/NC and Pt/C. DFT calculations revealed that the Fe site acts as the catalytic center to realize the ORR, and the Ni site regulates the electronic structure of Fe to reduce the energy barrier of the RDS.[165] Furthermore, Lu *et al.* constructed an Fe–Ni DMC (Fe-NiNC) *via* a one-step dual-solvent ion deposition method. Specifically, the $Fe(NO_3)_3$ aqueous solution was added dropwise to the Ni-doped polydopamine *n*-hexane solution followed by calcination and leaching to form Fe-NiNC. The aberration-corrected HAADF-STEM image showed some bright spot pairs with a distance of 0.18 nm, implying the presence of metal–metal bonds. The FT-EXAFS spectra of Fe and Ni K-edges show the main peaks at ~1.47, 1.38 and 2.43 Å, which can be assigned to Fe–N, Ni–N and Fe–Ni bonds, respectively. The resulting Fe-NiNC displayed good ORR activity with E_{onset} and $E_{1/2}$ of 0.86 and 0.75 V (*vs.* RHE), respectively, in 0.1 M KOH solution, which can be ascribed to the mutual effects of Fe and Ni for charge redistribution to facilitate the ORR performance.[175] In addition, Sun *et al.* synthesized a bimetallic FeNi-NC catalyst for the ORR by heating a mixture of $NiCl_2$, $FeCl_2$, and $ZnCl_2$ and formamide. The results of aberration-corrected HAADF-STEM image and FT-EXAFS spectra confirmed the atomic dispersion of Fe and Ni atoms. X-ray photoelectron spectroscopy (XPS) fine scans combined with computational simulations demonstrated the strong synergistic interaction between Fe and Ni. Consequently, the FeNi-NC catalyst delivered high ORR $E_{1/2}$ of 0.85 V, which is comparable to that of the Pt/C-RuO_2 mixture.[190]

4.3.2.3 Fe–Cu DMCs. In 2020, Chen *et al.* fabricated a highly-dispersed Fe–Cu dual-atom nanozyme as an ORR electrocatalyst (FeCu-DA/NC) to mimic cytochrome *c* oxidase *via* the pyrolysis of a mixture of $FeCl_3{\cdot}6H_2O$, $CuCl_2{\cdot}2H_2O$, nano-$CaCO_3$ and polyvinylpyrrolidone. The aberration-corrected HAADF-STEM image revealed some atomic pairs with the distance of ~0.5 nm, demonstrating the absence of metal–metal bonds. In the FT-EXAFS spectra, only the primary peaks at ~1.5 Å were observed for both Fe and Cu K-edges, which were assigned to the Fe–N and Cu–N paths, respectively. The resulting FeCu-DA/NC exhibited high ORR activity in both acidic and alkaline conditions. In 0.1 M KOH, the E_{onset} and $E_{1/2}$ were 0.96 and 0.86 V (*vs.* RHE), which are much more positive than that for Fe (0.91 and 0.8 V *vs.* RHE) and Cu (0.87 and 0.78 V *vs.* RHE) MMCs, as well as commercial Pt/C (0.94 and 0.83 V *vs.* RHE), respectively. In 0.5 M H_2SO_4, FeCu-DA/NC also displayed a much more positive E_{onset} and $E_{1/2}$ than Fe and Cu MMCs, and only a gap of 20 mV to that of Pt/C. The improved ORR activity of FeCu-DA/NC can be attributed to the synergistic effect between Fe and Cu, in which Fe acts as the active center to activate O_2, and Cu serves as the electron donor to increase the electron density of Fe to promote O_2 activation.[191] Moreover, Yan *et al.* prepared a Fe–Cu bimetal site catalyst (FeCu–N-HC) for the ORR by pyrolyzing a mixture of pyrrole, $FeCl_2{\cdot}4H_2O$, $CuCl_2$, and SiO_2 nanospheres followed by acid etching. The aberration-corrected HAADF-STEM image showed some bright paired spots distributed on the carbon support with an interatomic distance of 0.24 nm, suggesting the existence of Fe–Cu atomic pairs. The FT-EXAFS spectra showed prominent peaks at 1.4 Å, 2.0 Å and 2.3 Å in the Fe and Cu K-edges, which can be ascribed to the Fe–N, Fe–Cu and Cu–Fe scattering paths, respectively. In 0.1 M KOH solution, FeCu–N-HC showed an $E_{1/2}$ of 0.92 V (*vs.* RHE), which is much better than that for Fe (0.89 V), Cu (0.83 V) MMCs and 20% Pt/C (0.87 V). DFT calculations revealed that the elongation of the O–O bond over FeCu–N-HC favours its dissociation, thereby enhancing the reaction efficiency.[192]

4.3.2.4 Fe–Mn DMCs. In 2018, Chen *et al.* designed an efficient Fe–Mn electrocatalyst for the ORR *via* the one-step pyrolysis of ZIF-8 containing Fe and Mn ions. The aberration-corrected HAADF-STEM and XANES results confirmed the presence of highly dispersed Fe and Mn atoms anchored on N-doped carbon. The obtained catalyst displayed high ORR activity with an $E_{1/2}$ of 0.904 V (*vs.* RHE), which is 49 mV more positive than that of commercial 20% Pt/C. DFT calculations

demonstrated that the introduction of Mn ions regulated the electronic structure of Fe active centers to lower the energy barrier of the ORR process, thus enhancing the catalytic activity.[193] Moreover, Dong *et al.* synthesized a novel Fe–Mn DMC (Fe–Mn–N/S@mC) with atomically dispersed Fe–N_4 and Mn–N_2S_2 sites *via* the thermal treatment of oleic-acid-capped $Mn_{0.43}Fe_{2.57}O_4$ nanocrystals. The aberration-corrected HAADF-STEM image showed many bright spots distributed in the carbon framework, corresponding to heavy Fe and/or Mn atoms. A prominent peak at 1.41 Å was observed in the Fe K-edge FT-EXAFS spectrum, which was attributed to Fe–N coordination. The Mn K-edge FT-EXAFS spectrum showed a main peak at 1.72 Å, corresponding to Mn–N/S coordination. In 0.1 M KOH, Fe–Mn–N/S@Mc exhibited excellent catalytic activity for the ORR with an $E_{1/2}$ of 0.896 V (*vs.* RHE), outperforming the conventional Pt/C (0.856 V *vs.* RHE). DFT calculations revealed that the synergistic interaction between Fe and Mn atoms lowers the energy barrier of *OH reduction, resulting in improved ORR activity.[194]

Besides, Zhang *et al.* designed and synthesized a dual-metal atomically dispersed Fe,Mn/N–C electrocatalyst *via* the pyrolysis of dicyandiamide, Fe–phthalocyanine complex and $Mn(NO_3)_2$ (Fig. 11a). The aberration-corrected HAADF-STEM image revealed some bright paired spots, which were attributed to the Fe/Mn atomic pairs, and further confirmed *via* EELS (Fig. 11b and c). The FT-EXAFS spectrum of Fe K-edge showed two peaks at 1.4 and 2.16 Å, corresponding to the Fe–N bond and Fe–metal atomic pair, respectively (Fig. 11d). The FT-EXAFS spectrum of Mn K-edge also demonstrated Mn–N bond and Mn–metal atomic pairs (Fig. 11e). The resultant Fe,Mn/N–C

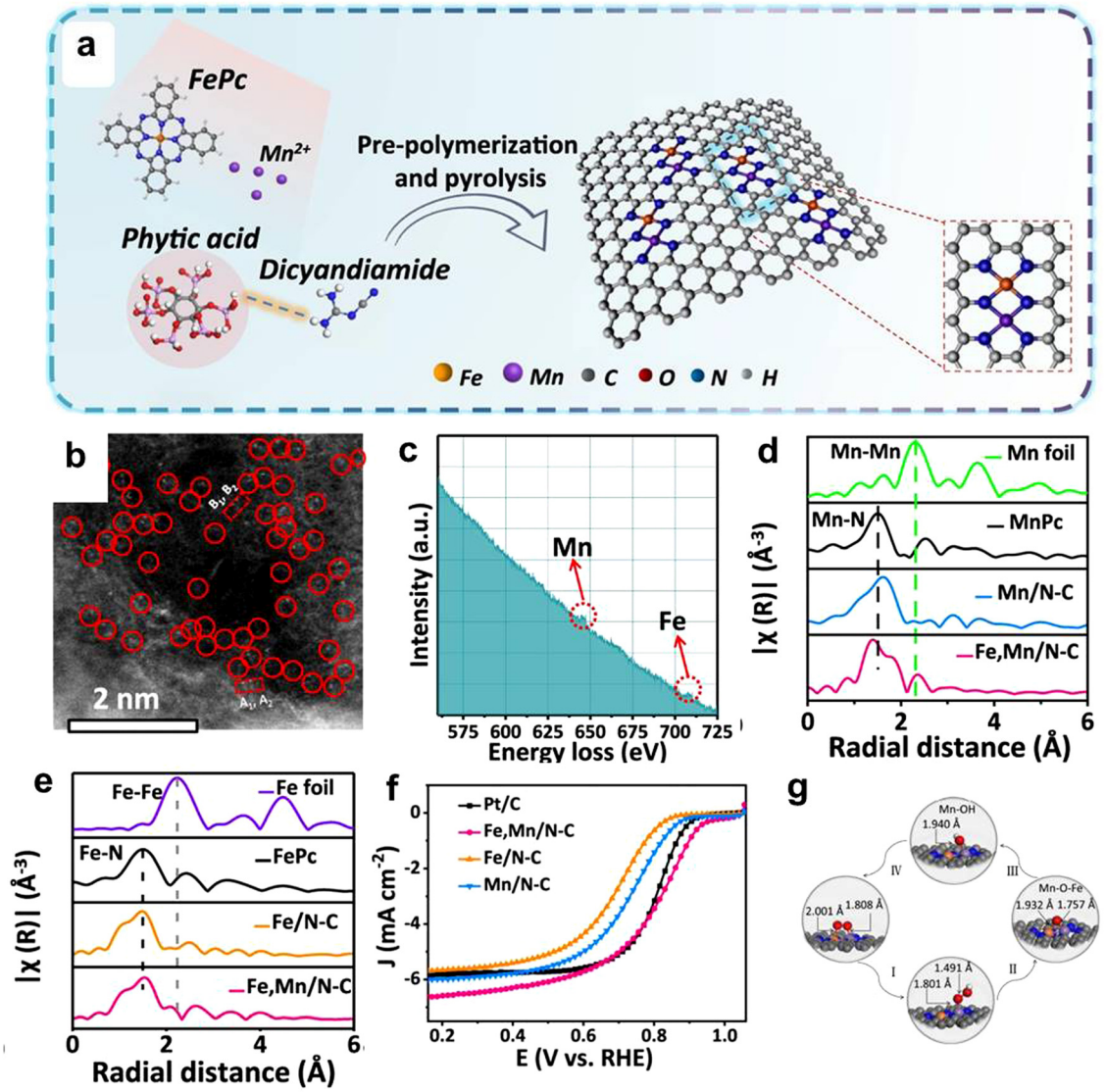

Fig. 11 (a) Schematic illustration showing the fabrication of Fe,Mn/N–C. (b) Aberration-corrected HAADF-STEM images of Fe,Mn/N–C. (c) EELS data of Fe,Mn/N–C. (d) Fe K-edge FT-EXAFS spectra of Fe,Mn/N–C and reference samples. (e) Mn K-edge FT-EXAFS spectra of Fe,Mn/N–C and reference samples. (f) LSV curves of Fe,Mn/N–C, Fe/N–C, Mn/N–C and Pt/C catalyst in 0.1 M $HClO_4$ solution. (g) Optimized atomic structures for the main process of the ORR on Fe,Mn/N–C. Reproduced from ref. 195 with permission from Springer Nature, Copyright 2021.

displayed excellent ORR performance with an $E_{1/2}$ of 0.804 V (*vs.* RHE) in 0.1 M $HClO_4$ and 0.928 V (*vs.* RHE) in 0.1 M KOH, which is comparable to that of the commercial Pt/C (Fig. 11f). Magnetic measurements together with theoretical calculations revealed that the introduction of Mn atoms tuned the spin state of Fe^{III}, resulting in the appropriate bond length and binding energy to stabilize the oxygen intermediate, leading to excellent ORR activities (Fig. 11g).[195] Zhao *et al.* also prepared an atomically dispersed Fe–Mn DMC *via* the pyrolysis of ZnO@polydopamine containing Fe and Mn ions under an N_2 atmosphere. The aberration-corrected HAADF-STEM image illustrated a large number of bright spots on the carbon support, in which some paired dots evidenced the formation of diatomic sites. The diatomic sites were further confirmed *via* EELS as the Fe and Mn edge peaks at ~650 and ~715 eV, respectively. The FT-EXAFS spectrum of the Fe K-edge showed two peaks at 1.48 and 2.41 Å, which can be assigned to the Fe–N and Fe–Mn scattering paths, respectively. The prepared Fe-Mn DMC displayed excellent ORR activity with $E_{1/2}$ and E_{onset} of 0.88 and 1.02 V (*vs.* RHE) in 0.1 M KOH solution, which are much more positive than that of Fe (0.85 and 0.97 V *vs.* RHE) and Mn (0.74 and 0.89 V *vs.* RHE) MMCs, respectively. The mechanistic study demonstrated that the synergic effect of the diatomic site lowered the energy barrier of the intermediate adsorption, and thus improved the ORR activity.[196]

4.3.2.5 Fe–Mo DMCs. Li *et al.* constructed an Fe–Mo dual site catalyst (FeMo–N–C) by pyrolyzing FeZn-ZIF containing $MoO_2(acac)_2$ molecules. The aberration-corrected HAADF-STEM image demonstrated some paired dots, corresponding to Fe–Mo atomic pairs, which was further confirmed *via* EELS. The FT-EXAFS spectra of FeMo–N–C in *R* space showed dominant peaks at 1.5 and 1.2 Å, which are attributed to the Fe–N and Mo–N bonds, respectively. The negligible signals for the metal–metal scattering paths imply the presence of atomically distributed Fe and Mo atoms. Consequently, FeMo–N–C delivered outstanding electrocatalytic ORR activity with $E_{1/2}$ and E_{onset} of 0.84 and 0.98 V (*vs.* RHE), respectively, in 0.1 M $HClO_4$ electrolyte, which were more positive than that of its Fe–N–C single-atomic counterpart (0.77 and 0.91 V *vs.* RHE). DFT calculations showed that the presence of Mo modulated the electronic configuration and down-shifted the d-band center of Fe, which optimized the adsorption of ORR intermediates, thereby boosting the catalytic activity.[197]

4.3.2.6 Co–Ni DMCs. In 2019, Hu *et al.* reported the synthesis of an atomically dispersed bimetallic Co–Ni site catalyst (CoNi-SAs/NC) by pyrolyzing dopamine-coated CoNi-MOF for the ORR. The aberration-corrected HAADF-STEM and elemental mapping images demonstrated the presence of isolated Co and Ni atoms. The FT-EXAFS spectra of the Co and Ni K-edges showed major peaks at ~1.5 Å, corresponding to the Co–N and Ni–N paths, respectively. In addition, a weak peak at ~2.22 Å was also observed, which can be attributed to the diatomic Co–Ni coordination. In 0.1 M KOH solution, CoNi-SAs/NC displayed outstanding ORR activity with $E_{1/2}$ and E_{onset} of 0.76 and 0.88 V (*vs.* RHE), which are comparable to that of commercial Pt/C (0.82 and 0.90 V *vs.* RHE), respectively. DFT calculations demonstrated that the synergistic effect between neighboring Co and Ni can lower the energetic barrier and promote the reaction kinetics, thus substantially enhancing the catalytic performance.[169] Furthermore, Pan *et al.* synthesized a Co-Ni DMC (NiCo DASs/N–C) featuring the proximity electronic effect (PEE) by pyrolyzing NiCo@ZIF-8 precursor to synergistically promote the ORR. The aberration-corrected HAADF-STEM image showed many paired bright spots, suggesting that Co and Ni atomic pairs exist in NiCo DASs/N–C. The distance between the Co–Ni pairs is ~6.4 Å, indicating the dispersion of Co–Ni diatomic sites. According to the Co K-edge FT-EXAFS curve, a main peak at 1.5 Å was observed in *R* space, corresponding to Co–N coordination. The FT-EXAFS spectrum of Ni K-edge presented a main peak at 1.31 Å, which was assigned to Ni–N coordination. No peak corresponding to metal–metal coordination was observed, indicating the presence of the atomically dispersed Co and Ni atoms. The catalytic results demonstrated that NiCo DASs/N–C exhibited outstanding $E_{1/2}$ of 0.880 and 0.754 V (*vs.* RHE) in alkaline and acidic solution, which are much higher than that of single-metal Ni (0.716 and 0.618 V *vs.* RHE) and Co (0.746 and 0.661 V *vs.* RHE) catalysts, respectively. The *in situ* characterization and theoretical calculation results indicated that the Co atom served as the active site for O_2 adsorption–activation, and the adjacent Ni site acted as a modulator to promote *OH and *H adsorption on the Co site, thus significantly boosting the ORR activity.[198]

4.3.2.7 Co/Cu–Zn DMCs. In 2018, Sun *et al.* fabricated a bimetallic Co–Zn site catalyst (Zn/CoN–C) *via* the pyrolysis of a mixture of chitosan, $ZnCl_2$ and $Co(CH_3COO)_2$, followed by acid etching and annealing process (Fig. 12a). The aberration-corrected HAADF-STEM images revealed a large number of bright spots on the carbon support, among which some paired bright spots were observed with the distance of ~0.22 nm, corresponding to the Co–Zn atomic pairs (Fig. 12b and c). The Co K-edge FT-EXAFS spectrum of Zn/CoN–C showed two main peaks at 1.4 and 2.1 Å, which can be attributed to the Co–N and Co–metal coordination, respectively (Fig. 12d). In the Zn K-edge FT-EXAFS spectrum, two primary peaks at 1.44 and 2.1 Å were detected, corresponding to Zn–N and Zn–metal coordination, respectively (Fig. 12e). These results indicate the existence of the Co–Zn bond in Zn/CoN–C. As shown in Fig. 12f, the prepared Zn/CoN–C exhibited excellent ORR activity with the $E_{1/2}$ of 0.861 V (*vs.* RHE) in 0.1 M KOH solution, superior to that of CoN–C (0.793 V *vs.* RHE) and ZnN–C (0.706 V *vs.* RHE) MMCs, as well as Pt/C (0.825 V *vs.* RHE). DFT calculations demonstrated that the bimetallic Co and Zn with N sites could enhance the binding ability of O_2 and elongate the O–O bond from 1.23 to 1.42 Å, thereby promoting the cleavage of the O–O bond. The assembled zinc–air battery with Zn/CoN–C as the cathode catalyst delivered the maximum power density of 230 mW cm^{-2} in 6 M KOH electrolyte, which outperformed its Pt/C counterpart (201 mW cm^{-2}) (Fig. 12g).[199]

Moreover, Yang *et al.* constructed a non-precious-metal-based ORR catalyst (Co/Zn–NCNF) for the ORR with Co–Zn

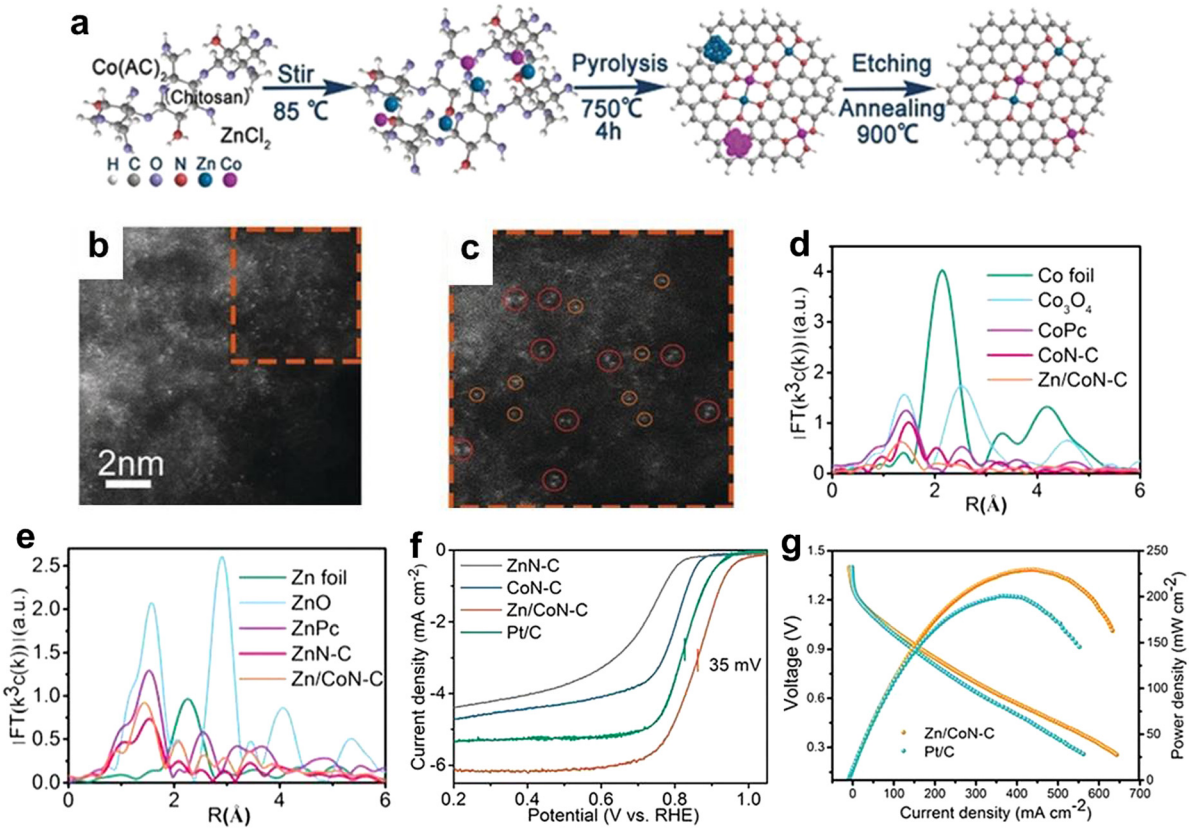

Fig. 12 (a) Schematic illustration showing the synthesis of Zn/CoN–C. (b and c) Aberration-corrected HAADF-STEM images of Zn/CoN–C. FT-EXAFS spectra of Co (d) and Zn (e) K-edges of Zn/CoN–C. (f) LSV plots of Zn/CoN–C, CoN–C, ZnN–C and Pt/C. (g) Polarization and power density curves of assembled zinc-air battery over Zn/CoN–C and Pt/C as ORR catalyst in 6 M KOH electrolyte. Reproduced from ref. 199 with permission from Wiley-VCH, Copyright 2019.

dual active sites *via* electrospinning, carbonization and post-treatment. The aberration-corrected HAADF-STEM images revealed paired bright dots with a distance of ~0.23 nm, suggesting the formation of Co–Zn dual sites. In the FT-EXAFS spectra, the Co and Zn K-edges in *R* spaces showed main peaks at 1.40 and 1.44 Å, which were attributed to the Co–N and Zn–N scattering paths, respectively. The ORR catalytic activity of Co/Zn-NCNF indicated $E_{1/2}$ and E_{onset} of 0.797 and 0.997 V (*vs.* RHE), respectively, in 0.1 M $HClO_4$ solution, outperforming the Co and Zn MMC comparison samples, and only 41 mV more negative than that for commercial Pt/C. DFT calculations revealed that the presence of Co–Zn dual sites lowered the dissociation barrier of the *OOH intermediate, thus improving the ORR activity.[200] Besides, Fu *et al.* constructed a bimetallic single-atom catalyst (Cu/Zn-NC) with Zn–N_4 and Cu–N_4 by directly pyrolyzing the CuZn-ZIF precursor. The aberration-corrected HAADF-STEM image demonstrated numerous bright spots, which were attributed to atomically dispersed Cu or Zn on the carbon substrate. The FT-EXAFS spectra of Cu and Zn K-edges showed the primary peaks at ~1.50 and 1.44 Å, corresponding to the Cu–N and Zn–N scattering paths, respectively. No signals of metal–metal bonds were observed, further verifying the atomic dispersion of Cu and Zn atoms in Cu/Zn-NC. The catalytic results of the ORR demonstrated that Cu/Zn-NC displayed an E_{onset} of 0.98 V (*vs.* RHE) in 0.1 M KOH electrolyte, superior to that for Zn (0.86 V *vs.* RHE) and Cu (0.89 V *vs.* RHE) MMCs, and similar to that for Pt/C (0.99 V *vs.* RHE). Operando XANES analyses and DFT calculations revealed that the presence of the Zn atom regulated the d-orbital electron distribution of the Cu active center to promote the cleavage of O–O on the Cu site, thus accelerating the ORR process.[201]

4.3.2.8 Pt–Fe/Co DMCs. In addition to transition metals, some noble-metal-based DMCs have been also constructed for electrocatalytic ORR. For example, Yu *et al.* prepared a Pt single-atom-grafted Fe–N–C electrocatalyst (Pt_1@Fe–N–C) with Pt_1–O_2–Fe_1–N_4 active moieties by stirring Fe–N–C powder in H_2PtCl_6 solution. The aberration-corrected HAADF-STEM image clearly revealed many bright dots, which were attributed to Fe, Pt atoms or Fe/Pt atomic pairs, suggesting the presence of atomically dispersed Fe and Pt atoms. The FT-EXAFS spectrum of Fe K-edge demonstrated two main peaks at 1.6 and 1.2 Å, corresponding the Fe–N and Fe–O scattering paths, respectively. The FT-EXAFS data of Pt showed a major peak at 1.6 Å, which can be assigned to the Pt–O scattering path. No metal–metal scattering path was detected in the FT-EXAFS spectra, implying the atomically dispersed Fe and Pt, and the possible Pt_1–O_2–Fe_1–N_4 active moieties in Pt_1@Fe–N–C. The resulting Pt_1@Fe–N–C with 2.1 wt% Pt exhibited outstanding ORR activity in 0.5 M H_2SO_4 solution with E_{onset} and $E_{1/2}$ of 0.93

and 0.80 V (*vs.* RHE), respectively. The assembled half-cell with Pt_1@Fe–N–C as the optimized cathode catalyst displayed a high current density of 280 mA cm^{-2} at 0.8 V (*vs.* RHE), which is higher than that of Fe–N–C (211 mA cm^{-2}) and 20% Pt/C (193 mA cm^{-2}). DFT calculations revealed the existence of synergy in the Pt_1–O_2–Fe_1–N_4 active moiety, which accelerated the kinetics of proton adsorption and reduction.[202] Furthermore, Zou *et al.* constructed a Pt–Fe DMC (Pt_1–Fe/Fe_2O_3) by loading atomic Pt on α-Fe_2O_3 (012) facets with 0.13 wt% Pt. The aberration-corrected HAADF-STEM image clearly revealed individual Pt atoms dispersed on Fe_2O_3. The FT-EXAFS spectrum of Pt L_3-edge showed two primary peaks at 1.8 and 2.4 Å, which can be attributed to the Pt–O and Pt–Fe contributions, respectively. The catalytic results of the ORR showed that Pt_1–Fe/Fe_2O_3 exhibited a high E_{onset} and $E_{1/2}$ of 1.15 V and 1.05 V (*vs.* RHE), respectively, in 0.1 M KOH solution, which is superior to that for Fe_2O_3(012) (E_{onset} = 0.78 V *vs.* RHE). In addition, Pt_1–Fe/Fe_2O_3 displayed high mass activity of 14.9 A mg^{-1}_{Pt} at 0.95 V (*vs.* RHE) and stability over 50 000 cycles. The outstanding catalytic activity of Pt_1–Fe/Fe_2O_3 was ascribed to the fact that the Pt–Fe pair sites can cooperatively adsorb O_2 and dissociate the O═O bond, and the key OH* intermediate desorbs over the Pt site.[203] In addition, Yao *et al.* prepared an atomic Pt–Co nitrogen–carbon-based catalyst (A-CoPt-NC) with a Pt content of 0.16 wt% by calcining Co-MOF, followed by electrochemical activation with a Pt wire as the counter electrode. The aberration-corrected HAADF-STEM image clearly showed atomic Pt/Co metals trapped in a vacancy-type defect. The results of the XANES analysis demonstrated that atomic Co–Pt–N–C configurations with Co–N and Pt–N bonds. A-CoPt-NC exhibited high activity for the ORR with an $E_{1/2}$ of 0.96 V (*vs.* RHE) in 0.1 M KOH electrolyte, which is 90 mV superior to that of Pt/C. The ORR mass activity of A-CoPt-NC was 45.47 A mg^{-1}, which is 267 times higher that of the commercial Pt/C. DFT calculations revealed that this high activity can be attributed to the charge redistribution and d orbital shift induced by the synergistic effect of the Pt–Co atomic pair.[204]

4.3.2.9 Pd–Mo DMCs. Using a one-pot wet-chemical approach, Guo *et al.* prepared a PdMo bimetallene catalyst with excellent ORR performance. The PdMo bimetallene possessed a morphology of two-dimensional nanosheets, with an average thickness of 0.88 nm, as identified *via* HAADF-STEM and atomic force microscopy (AFM). The PdMo bimetallene had a large electrochemically active surface area and high atomic utilization, which resulted in high mass activity for the ORR, with the value reaching as high as 16.37 A mg^{-1}_{Pd} at 0.9 V (*vs.* RHE). This mass activity was 78 and 327 times higher than that of the commercial Pt/C and Pd/C catalysts, respectively. Moreover, the ORR polarization curves showed that PdMo bimetallene/C had an $E_{1/2}$ of 0.95 V in 0.1 M KOH, which is higher than that for the commercial Pt/C (0.85 V) and Pd/C (0.84 V). DFT calculations revealed that the higher mass activity of PdMo could be ascribed to the cooperative catalysis. Specifically, in PdMo bimetallene, there is substantial charge transfer from Mo to Pd, which makes the Pd d-band center shift towards negative energy. The downshift of the d-band center shifts the oxygen binding energy towards the optimal value. The alloying effect, together with the strain effect and quantum size effect, contributed to the enhanced ORR activity of PdMo bimetallene.[205]

4.4 CO_2RR

Many strategies have also been developed to design and synthesize heterogeneous DMCs to achieve photo- and electrocatalytic CO_2RR.[221–276] However, more examples have been reported for the latter.

4.4.1 Photocatalysis

4.4.1.1 Homonuclear DMCs. Encouraged by the successful work on designing homogeneous DMCs for synergistic photocatalytic CO_2 reduction, we further prepared two types of ultrathin two-dimensional (2D) Ni-based metal–organic layers (MOLs) with rich (010) crystal facets (Ni-MOL-010) and (100) crystal facets (Ni-MOL-100) exposed for photocatalytic CO_2RR (Fig. 13a). Selected-area electron diffraction (SAED) showed clear diffraction spots along the [010] and [100] zone axes for Ni-MOL-010 and Ni-MOL-100, indicating their exposed (010) and (100) facets (Fig. 13b and d), respectively. The HRTEM images clearly revealed (001)/(100) and (010)/(001) crystal lattice fringes for Ni-MOL-010 and Ni-MOL-100, respectively, further confirming that the main crystal facets are (010) and (100) (Fig. 13c and e), respectively. The photocatalytic results demonstrated that Ni-MOL-100 displayed a 2.5-fold improvement in catalytic activity for CO_2 reduction to CO with respect to that of Ni-MOL-010 (Fig. 13f). The enhanced catalytic performance of Ni-MOL-100 was attributed to the synergistic catalysis between two neighboring Ni sites with a close separation distance of 3.50 Å on the surface of Ni-MOL-100, which lowered the rate-determining free-energy change (ΔG) value for photocatalytic CO_2-to-CO conversion, as revealed by the theoretical calculations.[221] Moreover, Kim *et al.* synthesized a series of Co DMCs with different Co contents by pyrolyzing a mixture of melamine, cyanuric acid and cobalt chloride for photo-driven CO_2RR. Co DMC-3.5 (3.5% Co atoms) was used as an example, where its aberration-corrected HAADF-STEM image revealed numerous bright spot pairs, which were assigned to the diatomic Co_2 sites. The FT-EXAFS spectra revealed Co–N and Co–Co shells in Co DMC-3.5. According to the FT-EXAFS fitting results, each Co atom is coordinated by three N atoms, and two adjacent Co atoms are connected through Co–Co bonding. Benefiting from the synergistic effect between the diatomic Co_2 sites, Co DMC-3.5 showed excellent catalytic activity for the CO_2RR with a CH_4 selectivity of 65.0%, which is superior to that of the single-atomic Co counterpart. Theoretical calculations disclosed that the diatomic Co_2 sites could help better stabilize the rate-limiting COOH* intermediate than the single-atomic Co site, which accounts for the high catalytic performance.[222]

4.4.1.2 Heteronuclear DMCs. The heteronuclear bimetallic active sites in heterogeneous catalysts can also exhibit synergistic effects to give rise to high photocatalytic activity for the CO_2RR. For instance, Cu and Ni dual-metal sites were successfully incorporated in a robust MOF (MOF-808) to yield a bioinspired MOF-808-CuNi photocatalyst for CO_2-to-CH_4

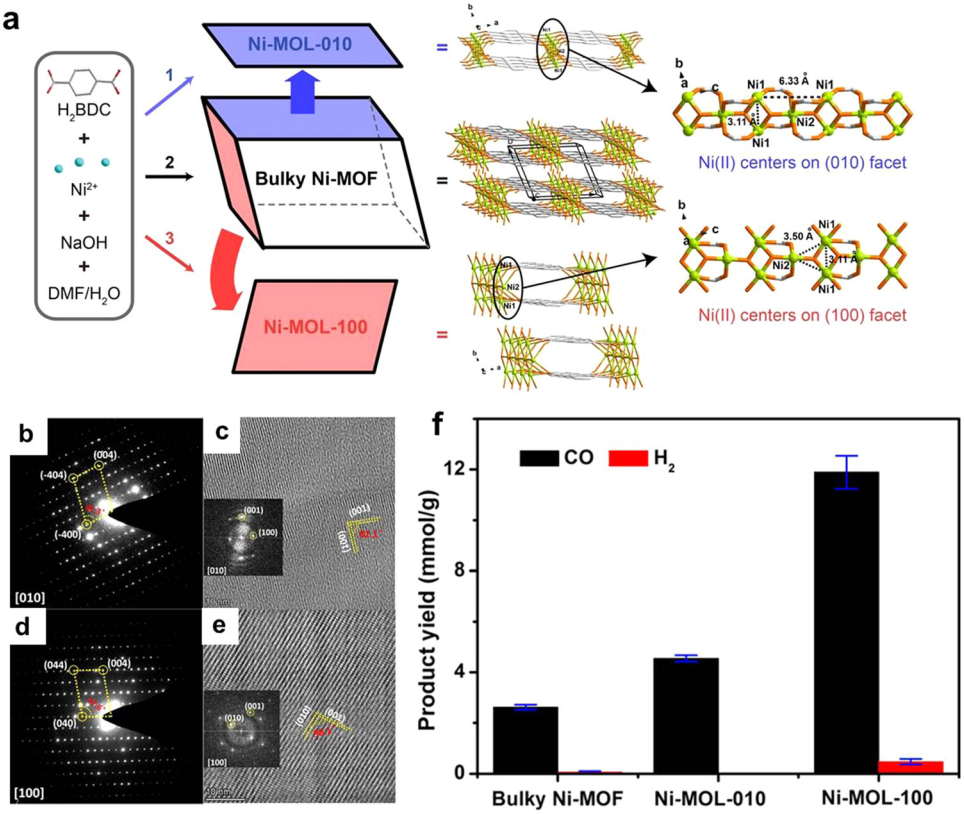

Fig. 13 (a) Schematic illustration showing the synthesis of bulky Ni-MOF, Ni-MOL-010, and Ni-MOL-100. (b) SAED pattern and (c) HRTEM image for Ni-MOL-010. (d) SAED pattern and (e) HRTEM image for Ni-MOL-100. (f) CO and H_2 production rates over a bulky Ni-MOF, Ni-MOL-010, and Ni-MOL-100 photocatalysts. Reproduced from ref. 221 with permission from Wiley-VCH, Copyright 2021.

conversion, as reported by Zhong *et al.* (Fig. 14a). The XANES results demonstrated that both Cu and Ni species are in their single-site forms and four-coordinated with two N and two O atoms from flexible ethylenediaminetetraacetic acid (EDTA). The obtained MOF-808-CuNi resulted in a high CH_4 production rate of 158.7 μmol g^{-1} h^{-1} and selectivity of 97.5%, which are higher than that of the corresponding MOF-808-Cu and MOF-808-Ni single-site catalysts (Fig. 14b and c). DFT calculations revealed that the synergistic effect and self-adaptive behaviour between Cu and Ni sites can stabilize various C1 intermediates and suppress the formation of undesired by-products, thus leading to high CH_4 selectivity (Fig. 14d).[82] Furthermore, Lu *et al.* constructed a series of Ni_xCo_y-GR composites (GR = reduced graphene oxide) with porous aerogel structures *via* a facile *in situ* growth method for photocatalytic CO_2RR. After Co doping, Ni_xCo_y-GR displayed significantly enhanced catalytic activity and selectivity due to the synergistic effect of Ni–Co bimetallic hydroxide. Consequently, the Ni_7Co_3-GR catalyst exhibited an excellent catalytic performance with a high CO formation rate of 941.5 μmol h^{-1} g^{-1} and selectivity of 96.3% in the absence of photosensitizers.[223] In addition, Li *et al.* synthesized a carbon nitride (CN) photocatalyst with Mn and Co double single-atom active sites (Mn_1Co_1/CN). In the process of the CO_2RR, the photogenerated holes migrate to the Mn site to promote H_2O oxidation, whereas photogenerated electrons migrate to the Co sites to reduce CO_2 to CO. Benefiting from the synergistic effect between the Mn and Co active centers, the CO formation rate of Mn_1Co_1/CN reached 47 μmol g^{-1} h^{-1}, which is higher than that of the corresponding single-metal site photocatalysts.[224]

In addition, hetero-dinuclear photocatalysts have been demonstrated as promising candidates to work synergistically to reduce CO_2 into C_{2+} products. For example, Guo *et al.* successfully prepared an atomically dispersed photocatalyst comprised of In–Cu atomic pairs anchored on polymeric carbon nitride (InCu/PCN) *via* a facile thermal polymerization approach for photocatalytic CO_2 reduction to CH_3CH_2OH. The aberration-corrected HAADF-STEM image revealed a number of paired bright and dark spots, which were identified as Cu (dark) and In (bright) atoms. The FT-EXAFS spectra showed Cu–N and In–N scattering paths. The results of the EXAFS fittings revealed that each Cu is coordinated by three N atoms, and each In is four-coordinated by four N atoms. The Cu and In atoms are bridged *via* a shared N atom to form a Cu–In atomic pair. InCu/PCN exhibited excellent catalytic efficiency with a CH_3CH_2OH production rate of 28.5 μmol g^{-1} h^{-1} and selectivity of 92%. Experimental investigation combined with DFT calculations revealed that the electronic structure of Cu was tuned by the introduction of In to facilitate the adsorption of *CO intermediates and lower the energy barrier for C–C coupling,

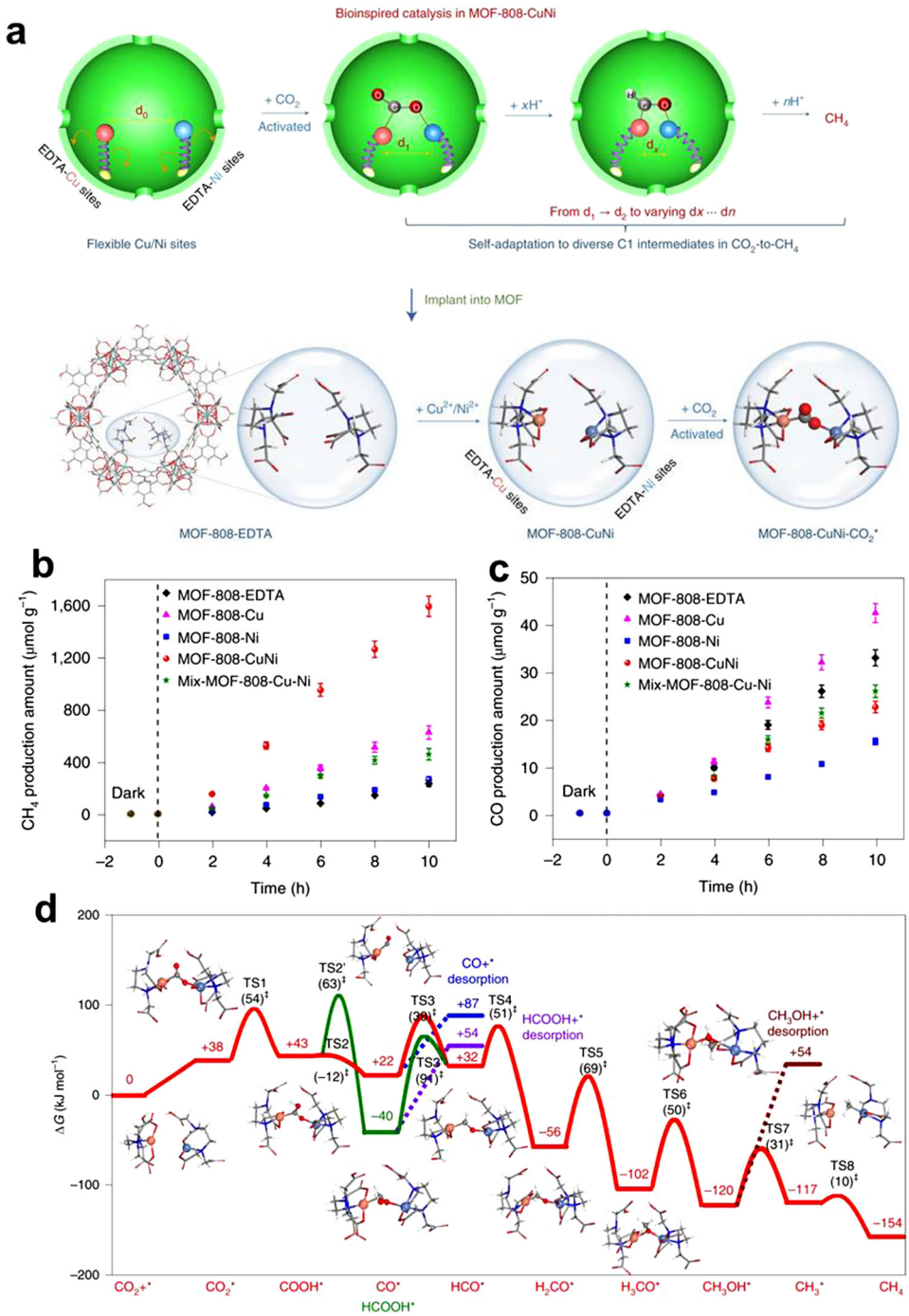

Fig. 14 (a) Schematic illustration of the implantation and self-adaption of flexible Cu/Ni dual-metal-site pairs in MOF-808 for highly selective CO_2 photoreduction to CH_4. (b and c) Time-dependent CH_4 and CO evolution curves over various photocatalysts. (d) Gibbs free energy diagram for the photoreduction of CO_2 to CH_4 over MOF-808-CuNi. Reproduced from ref. 82 with permission from Springer Nature, Copyright 2021.

thus further promoting the formation of CH_3CH_2OH.[225] Moreover, Yu *et al.* prepared a TiO_2-based photocatalyst involving asymmetric diatomic sites by replacing adjacent Ti atoms with Ni and Co atoms (NiCo–TiO_2) for photocatalytic CO_2 reduction into CH_3COOH. The immobilization of Ni and Co single sites on TiO_2 not only lowered the energy barriers of electron transfer, but also promoted C–C coupling to form CH_3COOH. Consequently, NiCo–TiO_2 displayed an impressive catalytic performance with CH_3COOH production rate of 22.6 μmol g^{-1} h^{-1} and selectivity of 71%.[226]

4.4.2 Electrocatalysis

4.4.2.1 Homonuclear DMCs. The homonuclear DMCs for electrocatalytic CO_2RR mainly include Fe_2, Ni_2, Cu_2, Ag_2, and Pd_2 DMCs. Han *et al.* constructed two Fe_2 DMCs (Fe_2-N_6-C-*o*

and Fe_2-N_6-C-*p*) *via* the pyrolysis of Fe-ZIF-8 precursor under different ratios of H_2 and Ar. The aberration-corrected HAADF-STEM images revealed numerous well-isolated atomic pairs, confirming the presence of Fe_2 bimetallic sites on the support. The FT-EXAFS curves displayed a prominent peak at 1.74 Å, which was assigned to the Fe–N shell. EXAFS fittings indicated that the coordination number of Fe–N is 4 for Fe_2–N_6–C-*o* and 3 for Fe_2–N_6–C-*p*. The catalytic results showed that the optimal Fe_2–N_6–C-*o* DMC achieved excellent activity with an FE_{CO} of above 80% over a wide applied potential window from −0.5 to −0.9 V (*vs.* RHE), which is better than that of its Fe_1–N–C MMC counterpart. The enhanced catalytic efficiency of Fe_2–N_6–C-*o* DMC is attributed to the synergistic effect on the Fe_2 site, which decreased the energy gap between the antibonding and bonding states for *CO adsorption.[237]

Yao *et al.* prepared a DMC consisting of Ni_2 sites anchored on N-doped carbon support (Ni_2/NC) *via* the pyrolysis of a dinuclear Ni complex and ZIF-8. The Ni_2 atomic pairs with the distance of ∼2.9 Å were identified *via* aberration-corrected HAADF-STEM. The FT-EXAFS spectra showed two main peaks at 1.4 and 2.4 Å, corresponding to the Ni–N and Ni–Ni shells, respectively. EXAFS fittings demonstrated that the coordination numbers of Ni–N and Ni–Ni were 4.3 and 1.2, respectively, suggesting that each Ni atom in Ni_2/NC is five-coordinated by four N atoms and one neighboring Ni atom. The obtained Ni_2/NC showed excellent activity and stability in the electrocatalytic CO_2RR. The FE_{CO} was 94.3% at the current density of 150 mA cm^{-2}, which is ∼1.3-fold higher than that of the corresponding Ni_1/NC MMC. Moreover, the FE_{CO} was maintained at 91% after 50 h continuous electrolysis at −0.6 V (*vs.* RHE). Theoretical simulations revealed that the formation of the O–Ni_2–N_6 structure in Ni_2/NC could help lower the energy barrier for the activation of CO_2 in the COOH* intermediate, thus explaining its high catalytic activity.[83] Moreover, Zhang *et al.* constructed a Ni_2 DMC by using a two-step method for electrocatalytic CO_2 reduction. Firstly, nickel acetylacetonate ($Ni(acac)_2$) was introduced in a solution of polyacrylonitrile/polystyrene (PAN/PS) to prepare PAN/PS/$Ni(acac)_2$ fibers *via* the electrospinning method. Upon pyrolysis in N_2, the PAN/PS/$Ni(acac)_2$ fibers were transformed into Ni_2 DMC with dinuclear nickel bridging structures (Ni_2–N_4–C_2), as confirmed by EXAFS results. This unique bridging structure could effectively tune the electronic structure of the d-states in Ni_2–N_4–C_2 to promote the favored reduction of CO_2 into CO. Consequently, the FE_{CO} over Ni_2–N_4–C_2 was >87.0% over a wide potential range from −0.6 to −1.0 V (*vs.* RHE), with the maximum FE_{CO} of 96.6% at −0.8 V (*vs.* RHE), which is much higher than that for Ni–N_3–C MMC.[238]

Besides, we designed and synthesized a series of Ni_2 DMCs (Ni_2–N_xC_y) with modulated electronic structures of Ni atoms for CO_2 electroreduction. A dinuclear Ni complex, carbon black and dicyandiamide were pyrolyzed in an Ar atmosphere at different temperatures, producing three Ni_2 DMCs with different N and C coordination numbers (namely, Ni_2–N_7, Ni_2–N_5C_2 and Ni_2–N_3C_4) (Fig. 15a). The aberration-corrected HAADF-STEM images clearly revealed many paired bright dots with a distance of ∼3.1 Å, which were assigned to dual Ni atoms (Fig. 15b and c). XPS combined with Ni K-edge XANES spectra showed that the valence states of Ni in these Ni_2 DMCs could be tuned *via* coordination environment engineering (Fig. 15d). The FT-EXAFS spectra of Ni_2–N_5C_2 and Ni_2–N_3C_4 presented Ni–N and Ni–C scattering paths, whereas only the Ni–N scattering path was identified for Ni_2–N_7 (Fig. 15e). The EXAFS fittings showed that each Ni atom in Ni_2–N_7, Ni_2–N_5C_2 and Ni_2–N_3C_4 is coordinated by four, three and two N atoms, respectively. The catalytic results demonstrated that Ni_2–N_3C_4 with the lowest N coordination number displayed the highest performance for CO_2 reduction into CO, in contrast to Ni_2–N_7, Ni_2–N_5C_2 and the corresponding Ni–N_2C_2 MMC (Fig. 15f). At −0.88 V (*vs.* RHE), the FE_{CO} of Ni_2–N_3C_4 was 98.9% (Fig. 15g). DFT calculations revealed that the significantly improved catalytic activity of Ni_2–N_3C_4 is attributed to the electronic structure modulation of the Ni centers to induce proper binding energies for the COOH* and CO* intermediates.[239]

Copper is a special catalyst for electrocatalytic CO_2RR, given that it can help reduce CO_2 into a diverse range of products, in particular, C_{2+} products. In 2019, Chen *et al.* fabricated a Cu_2 DMC by anchoring atom-pair sites (Cu-APC) on $Pd_{10}Te_3$ alloy nanowires. The experimental and theoretical data demonstrated that the Cu in the Cu-APC sample (0.10% Cu loading) is atomically dispersed and partially oxidized to Cu^{x+} to form Cu_4–O_x structures. In this configuration, one Cu atom binds with O to form Cu_1^{x+}, which further links with the adjacent Cu atom to generate a stable Cu_1^0–Cu_1^{x+} atom pair. The other two Cu atoms in the Cu_4 cluster are accommodated in the defects on nanowires to stabilize the Cu_1^0–Cu_1^{x+} atom pair. The results of electrocatalytic CO_2RR showed that the Cu_2 DMC exhibited excellent activity with the FE_{CO} of 92% at −0.78 V (*vs.* RHE), which is 6.57-times higher than that of undoped $Pd_{10}Te_3$ nanowires (14%). During the CO_2RR, Cu_1^0 adsorbs one CO_2, while the neighbouring Cu_1^{x+} binds one H_2O to form O–H···O hydrogen bond interaction with the oxygen of CO_2, thus promoting CO_2 activation and conversion.[84] Lan *et al.* synthesized two stable Cu-based coordination polymers (NNU-32 and NNU-33(S); S = sulfate radical), which displayed high selectivity for electrochemical CO_2-to-CH_4 conversion because of the intramolecular cuprophilic interactions. Single-crystal XRD revealed that NNU-32 contained octanuclear copper clusters with two cuprophilic interactions, and NNU-33(S) featured a cuprophilic interaction in octanuclear copper clusters. Moreover, during the electrocatalytic process, NNU-33(S) would be transformed into NNU-33(H), which contained four cuprophilic interactions. Consequently, NNU-33(H) with enhanced cuprophilic interactions exhibited an improved catalytic performance with an FE_{CH_4} of 82% at −0.9 V (*vs.* RHE), in contrast to NNU-32 (55.1% at −1.0 V *vs.* RHE). DFT calculations confirmed that the cuprophilic interaction effectively promoted the CO_2-to-CH_4 conversion by lowering the free energy of the RDS.[240]

Cu-based electrocatalysts can reduce CO_2 to C_{2+} products because Cu has moderate affinity to CO for promoting C–C coupling. Zhang *et al.* synthesized three isoreticular Cu-based MOFs with different functional groups on the organic ligands *via* the solvothermal reaction of Cu_2O and dialkyl-1,2,4-

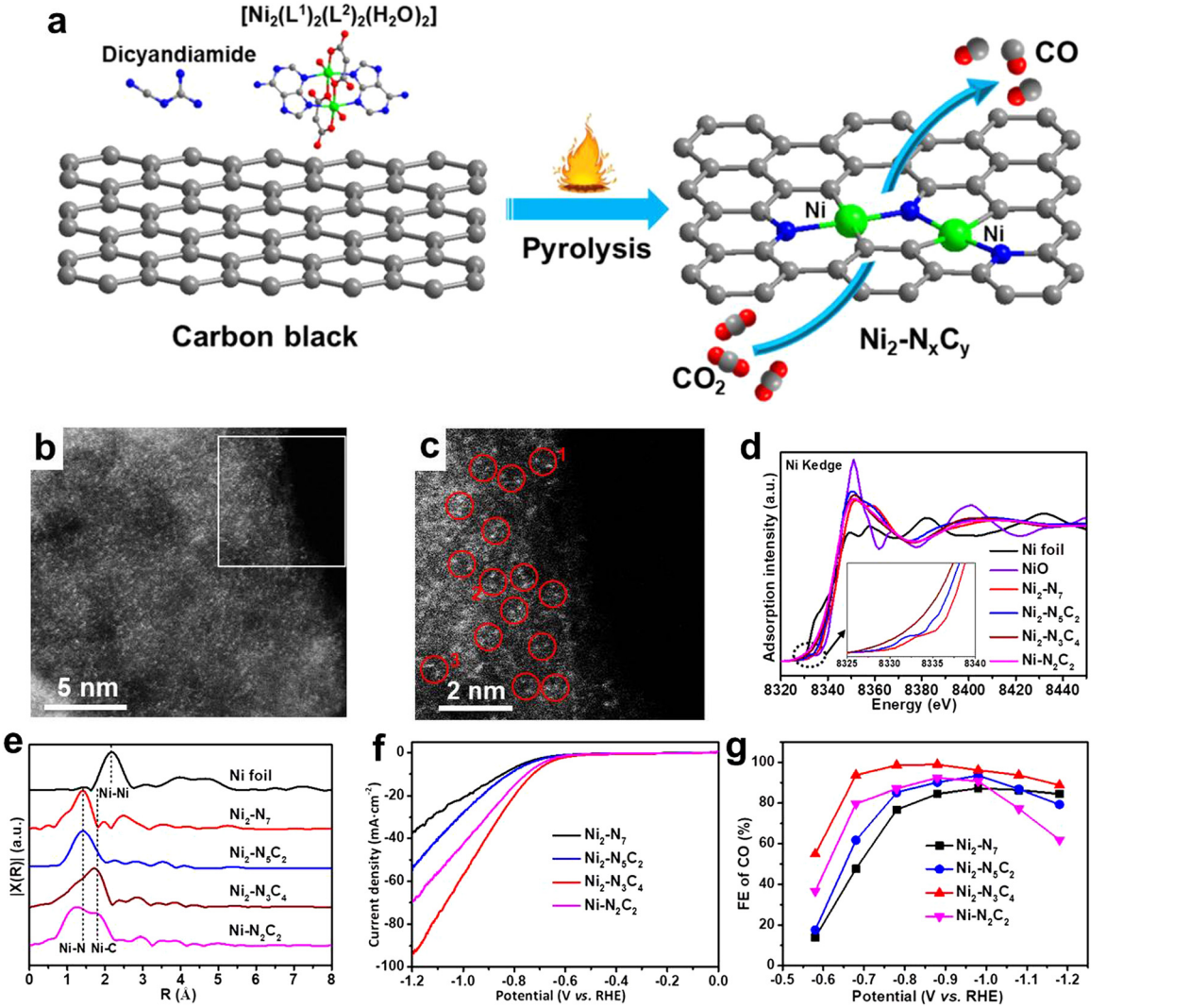

Fig. 15 (a) Schematic illustration showing the fabrication of Ni_2 DMC catalysts *via* one-step pyrolysis strategy for CO_2 electroreduction to CO. (b and c) Aberration-corrected HAADF-STEM image of Ni_2–N_3C_4, showing Ni_2 species highlighted by red circles. (d) Ni K-edge XANES spectra of Ni_2–N_xC_y, Ni–N_2C_2, Ni foil and NiO. (e) FT-EXAFS spectra at *R* space of Ni_2–N_xC_y, Ni–N_2C_2 and Ni foil. (f) LSV curves and (g) FEs for CO at different applied potentials for Ni_2–N_xC_y and Ni–N_2C_2. Reproduced from ref. 239 with permission from Wiley-VCH, Copyright 2022.

triazoles, in which the Cu(I) ions were trigonally bridged to form dimers with a Cu–Cu distance of 3.4 Å. The results of electrocatalytic CO_2RR showed that all three MOFs can help reduce CO_2 into C_2H_4, among which the MOF with ethyl groups achieved the highest $FE_{C_2H_4}$ of 51.2% ± 2.3% at −1.3 V (*vs.* RHE). Theoretical calculations demonstrated that the synergetic effect between the two adjacent Cu(I) ions facilitated C–C coupling for the formation of C_2H_4.[241] Similar results were also reported by Zhang *et al.* They constructed ultrathin boron imidazolate layers with Cl^--bridged dinuclear copper units (BIF-102NSs) for electrochemical CO_2RR. The catalytic results showed that BIF-102NSs exhibited higher activity for CO_2 reduction into C_2H_4 than its corresponding single-metal counterparts. Experimental observations combined with DFT calculations revealed that the enhanced catalytic activity is attributed to the cooperative nature of the Cu_2 dual-metal sites.[242]

In addition, Lan *et al.* designed and synthesized a series of Cu-based single-chain catalysts (Cu-PzX; X = H, Cl, Br, I; Pz = pyrazole) with different halogen atoms on the pyrazole ligands for electrochemical CO_2RR (Fig. 16a). The delicate variation in the ligands in these compounds resulted in different distances (from 3.57 to 3.63 Å) and dihedral angles (from 74.48° to 70.87°) in the contiguous active Cu sites, further giving rise to different synergistic effects on the Cu diatomic sites. Among the catalysts, Cu-PzH displayed the highest performance for the reduction of CO_2 into C_2H_4, with an $FE_{C_2H_4}$ of 60% and a large current density of 346.46 mA cm^{-2} at −1.0 V (*vs.* RHE, Fig. 16b). DFT calculations demonstrated that Cu-PzH exhibited the most negative d-band center, suggesting the strongest interaction between catalytic active sites and the key reaction intermediates, which is beneficial for C–C coupling (Fig. 16c). Moreover, Cu-PzH displayed an enhanced synergistic effect on the Cu diatomic sites to promote

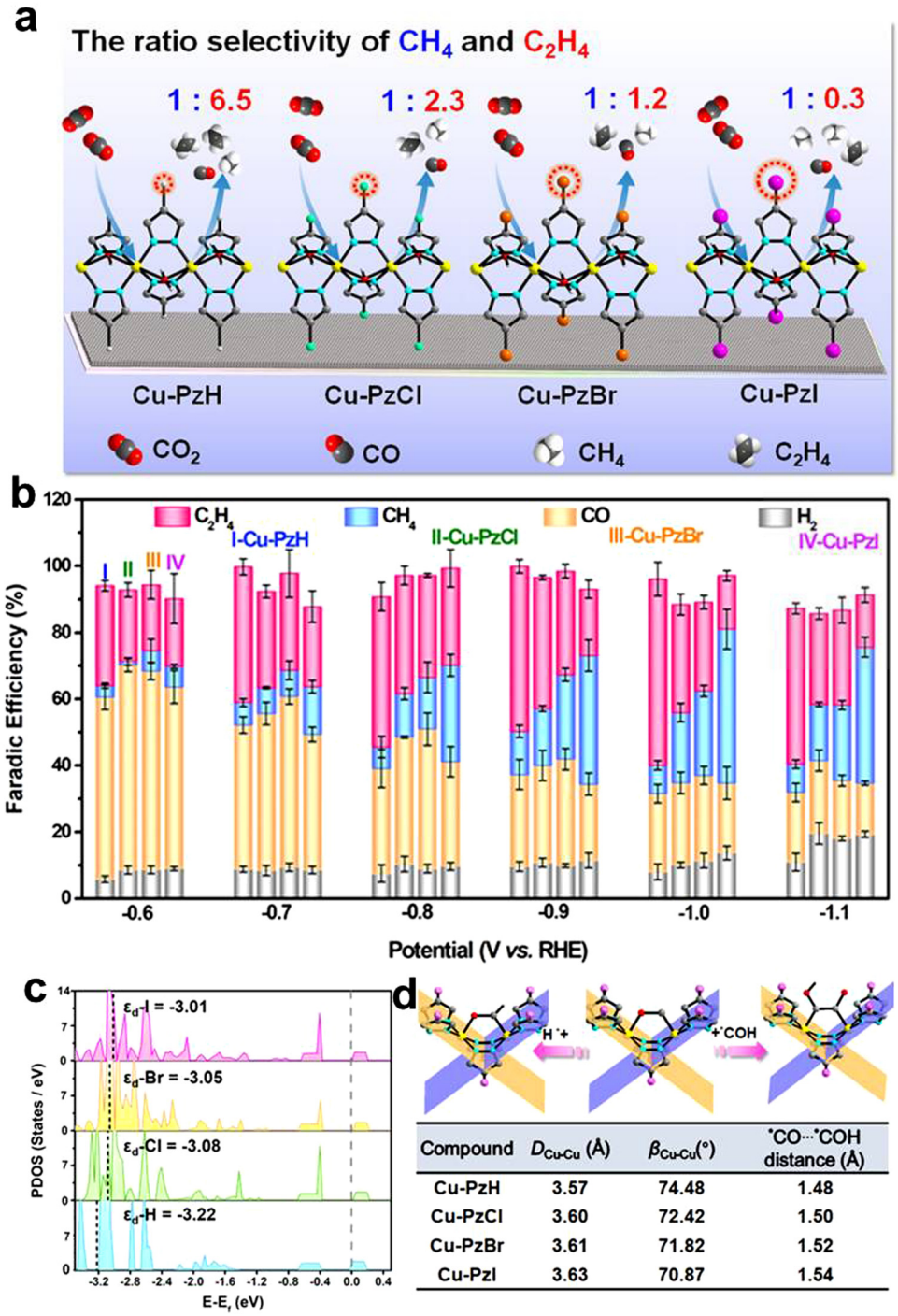

Fig. 16 (a) Schematic illustration of the different selectivities of Cu-PzX (where X = H, Cl, Br, I) for electrocatalytic CO_2RR. (b) FEs for different products over Cu-PzX at different applied potentials. (c) Partial density of states (PDOS) of Cu 3d for Cu-PzX. (d) Important parameters and RDS of optimized Cu-PzX structure. Reproduced from ref. 243 with permission from Wiley-VCH, Copyright 2021.

C–C coupling compared with the other compounds because of the shortest Cu–Cu distance (Fig. 16d). Liao *et al.* also synthesized a stable π–π stacking Cu-based framework with pyrazolate-bridged Cu diatomic sites for electrochemical CO_2 reduction. The result of single-crystal XRD showed that the Cu–Cu distance is 3.52 Å, and the diatomic sites may serve as active sites for CO_2 reduction into multi-carbon products. As expected, this Cu-based catalyst showed an excellent performance for CO_2 reduction into C_{2+} products with a total FE of 73.7% ± 2.8% [*i.e.*, ethylene (44%), ethanol (21%), acetate (4.7%), and propanol (4%)] at −1.3 V (*vs.* RHE). The control experiments and DFT calculations revealed that the synergistic effect between the active Cu site and intramolecular triazole protons could facilitate C–C coupling, leading to high catalytic activity.[243]

Noble-metal DMCs have also been reported for electrocatalytic CO_2RR with the DMSC effect. In 2020, Zhou *et al.* prepared a diatomic Ag_2/graphene catalyst (Ag_2–G) *via* the temperature-programmed pyrolysis of dinuclear Ag complex and graphene, in which AgN_3–AgN_3 diatomic sites were anchored on the graphene support by Ag–C bonds. The aberration-corrected HAADF-STEM image revealed that the Ag–Ag distance in Ag_2–G is about 0.35 nm, consistent with that in the dinuclear Ag complex. Ag_2–G catalyzed the CO_2RR at a potential of −0.25 V (*vs.* RHE) and showed a superior FE_{CO} of 93.4% with a current density of 11.87 mA cm^{-2} at −0.7 V (*vs.* RHE), which is much better than that of its single-atom Ag_1/graphene counterpart. DFT calculations revealed that the diatomic Ag_2 site in Ag_2–G could aid in the formation of the COOH* intermediate of the RDS, thus explaining its excellent catalytic activity.[80]

Besides Ag_2 DMCs, Pd_2 DMCs have also been constructed to synergistically catalyze the CO_2RR. For example, Wang *et al.* synthesized a Pd_2 DMC *via* the recombination of a dinuclear Pd complex and acetylene black *via* anion replacement deposition–precipitation method. The experimental characterization of HAADF-STEM, XPS and XAFS demonstrated that the Pd species in Pd_2 DMC has a PdN_2O_2 coordination structure, consistent with the precursor. The obtained Pd_2 DMC exhibited superior activity for the reduction of CO_2 into CO with an FE_{CO} of 98.2% at −0.85 V (*vs.* RHE), surpassing the Pd_1 MMC. DFT calculations demonstrated that the Pd_2 DMC shows a moderate CO* adsorption strength, thus promoting CO production.[244]

4.4.2.2 Heteronuclear DMCs. Several studies on heterogeneous heteronuclear DMCs for electrocatalytic CO_2RR have emerged during the past decade. In 2019, Zhao *et al.* synthesized an Fe–Ni DMC *via* the pyrolysis of Fe- and Ni-doped ZIF-8 at 1000 °C under an Ar atmosphere. The aberration-corrected HAADF-STEM image revealed many dual dots, which were assigned to the Fe–Ni diatomic sites. The EXAFS spectra of Fe–Ni DMC presented Fe–N, Ni–N and Fe–Ni scattering paths. The EXAFS fitting results demonstrated that both Fe and Ni are coordinated with three N atoms. The results of electrocatalytic CO_2RR demonstrated that this Fe–Ni DMC exhibited high activity with an FE_{CO} of greater than 90% over a wide potential window from −0.5 to −0.9 V (*vs.* RHE), with the maximum FE_{CO} of 98% at −0.7 V (*vs.* RHE), which is much higher than that of Fe and Ni MMCs. DFT calculations revealed that the Fe–Ni diatomic centers could lower the reaction barrier for the formation of COOH* and desorption of CO* because of the synergistic effect, which accounts for the excellent catalytic performance.[245] Jiang *et al.* developed a Zn-assisted atomization strategy to synthesize a novel Fe–Ni DMC (Fe_1-Ni_1–N–C) for electrocatalytic CO_2RR. Firstly, the negatively charged ZIF-8 precursor was synthesized *via* the reaction of Zn^{2+} and 2-methylimidazole. Subsequently, Fe–ZnO and Ni–ZnO NPs with positive surface charges were co-assembled outside ZIF-8 through electrostatic interaction to form an Fe&Ni-ZnO/ZIF-8 composite. Finally, the direct pyrolysis of this composite generated the Fe_1-Ni_1–N–C DMC with neighboring Fe and Ni atomic pairs (Fig. 17a). The aberration-corrected HAADF-STEM and EELS of Fe_1-Ni_1–N–C clearly demonstrated the existence of Fe–Ni atomic pairs with a distance of ∼4.1 Å (Fig. 17b and c). The FT-EXAFS analysis showed the presence of Fe–N and Ni–N bonding, but the absence of Fe–Fe, Fe–Ni and Ni–Ni bonding (Fig. 17d and e). EXAFS fittings further verified that the coordination configurations of Fe and Ni are Fe–N_4 and Ni–N_4, respectively. The results of electrocatalytic CO_2RR showed that Fe_1–Ni_1–N–C exhibited excellent catalytic activity with an FE_{CO} of 96.2% at −0.5 V (*vs.* RHE), which is higher than that of Fe_1–N–C and Ni_1–N–C MMCs (Fig. 17f and g). The significantly enhanced performance of Fe_1–Ni_1–N–C is attributed to the synergistic effect between Fe and Ni sites, which lowered the formation energy barrier of the COOH* intermediate.[246]

Besides, Wu *et al.* designed and synthesized an Fe–Ni DMC for electrocatalytic CO_2RR *via* a two-step synthesis approach. Firstly, an N-doped carbon support (ZIF-NC) was obtained by carbonizing ZIF-8 nanocrystals. Then, Fe and Ni were trapped by the N atoms in ZIF-NC to form ZIF-NC–Ni–Fe, which was further thermally activated at 900 °C under an Ar atmosphere to generate the Fe–Ni DMC. The Fe–Ni pairs were confirmed *via* high-resolution STEM, aberration-corrected HAADF-STEM and EELS. The Fe and Ni K-edge FT-EXAFS spectra displayed Fe–N and Ni–N coordination shells. EXAFS fittings together with DFT calculations demonstrated that both Fe and Ni were coordinated with four N atoms to generate Fe–N_4 and Ni–N_4 configurations, which were connected through Fe–Ni bonding and shared two N atoms. The electrocatalytic results showed that this Fe–Ni DMC exhibited excellent catalytic performance with a maximum FE_{CO} of 97.8% at −0.6 V (*vs.* RHE), which is higher than that of the corresponding Fe and Ni MMCs. DFT calculations further simulated three possible configurations including non-bridged (Fe–Ni)N_6, 2N-bridged (Fe–Ni)N_6, and 1N-bridged (Fe–Ni)N_7 sites, in which 2N-bridged (Fe–Ni)N_6 DMC with Fe and Ni sites bridged by two shared N atoms was predicted to have the highest activity for the CO_2RR. The outstanding catalytic performance of the 2N-bridged (Fe–Ni)N_6 DMC was attributed to the suitable distance between Fe and Ni, producing a synergistic effect to facilitate COOH* adsorption and CO* desorption in the CO_2RR.[247] Chen *et al.* also constructed an Fe–Ni DMC *via* the pyrolysis of L-alanine (an amino acid), ferric(II) acetate, nickel(II) acetate tetrahydrate, and melamine, in which the hetero-diatomic pairs were anchored on N-doped graphene. The aberration-corrected HAADF-STEM image suggested the presence of Fe–Ni atomic pairs, which was further confirmed *via* EELS. The results of the FT-EXAFS spectra suggested the existence of Fe–N, Ni–N and Fe–Ni bonds, and both Fe and Ni were coordinated with four N atoms. The obtained Fe–Ni DMC displayed an outstanding electrocatalytic performance for the reduction of CO_2 into CO with an FE_{CO} of 94.5% and current density of 50.4 mA cm^{-2} at an overpotential of 0.69 V, outperforming the corresponding Fe and Ni MMCs. The advanced experiments and theoretical calculations revealed that the orbital coupling between Fe and Ni led to a higher oxidation state of the catalytic center Fe and weakened binding strength with the intermediates, thus boosting the catalytic performance.[248]

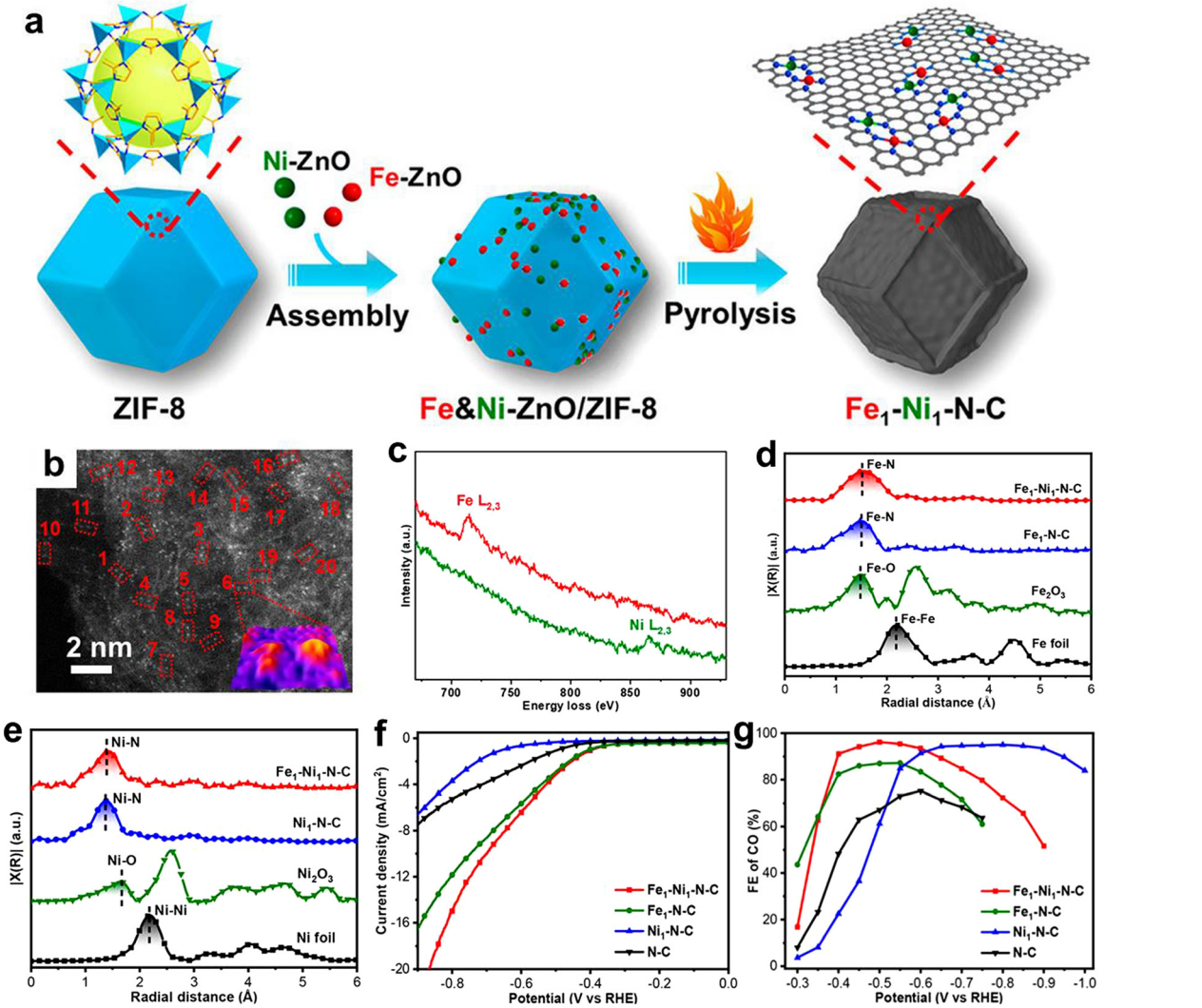

Fig. 17 (a) Schematic illustration of the fabrication of Fe_1–Ni_1–N–C DMC. (b) Aberration-corrected HAADF-STEM image of Fe_1–Ni_1–N–C DMC. (c) EELS spectra extracted from atomic pairs in (b). (d) Fe K-edge FT-EXAFS spectra of Fe_1–Ni_1–N–C and Fe_1–N–C. (e) Ni K-edge FT-EXAFS spectra of Fe_1–Ni_1–N–C and Ni_1–N–C. (f) LSV curves and (g) FEs of CO for Fe_1–Ni_1–N–C, Fe_1–N–C, Ni_1–N–C, and N–C in 0.5 M $KHCO_3$. Reproduced from ref. 246 with permission from the American Chemical Society, Copyright 2021.

Fan *et al.* also synthesized an Fe–Ni DMC (H-NiFe/NG) with surface oxygen vacancies *via* a steam-assisted chemical vapor deposition (CVD) method through a three-step procedure. Firstly, the hydrothermal treatment of ferric nitrate, nickel nitrate and graphene oxide (GO) formed a precursor solution, in which the Fe^{3+} and Ni^{2+} ions were anchored on the surface of GO. Next, this mixture was treated under NH_3/Ar gas *via* the CVD technique to generate Fe–Ni NPs dispersed on N-doped graphene (NiFe/NG). Finally, NiFe/NG was further treated through the CVD technique under H_2/H_2O/Ar gas by high-temperature annealing to form H-NiFe/NG. After the introduction of oxygen vacancies, the valence states of Fe^{3+} and Ni^{2+} ions decreased to +2 and +1, respectively, which is conducive to adsorb and activate CO_2. Therefore, H-NiFe/NG exhibited outstanding catalytic activity for electrocatalytic CO_2RR with the maximum FE_{CO} of 94% at −0.80 V (*vs.* RHE), which is twice as high as that for NiFe/NG without surface oxygen vacancies. Moreover, H-NiFe/NG showed higher catalytic activity than H-Ni/NG and H-Fe/NG MMCs because of the synergetic effect between Ni and Fe. DFT calculations confirmed that H-NiFe/NG featured the lowest energy barrier for the formation of the COOH* intermediate, thus exhibiting a superior catalytic performance for the CO_2RR.[249]

Liu *et al.* reported the synthesis of an Fe–Cu DMC for electrochemical CO_2RR *via* the thermal pyrolysis of Fe- and Cu-doped ZIF-8. The Fe–Cu dual sites were confirmed by aberration-corrected HAADF-STEM given that many distinct dual dots were observed on the substrate. The EXAFS results showed that both Fe and Cu were coordinated with three N atoms to form $Fe–N_3$ and $Cu–N_3$ configurations, which were linked by the formation of an Fe–Cu bond. The Fe–Cu DMC could effectively help to reduce CO_2 to CO with a maximum FE_{CO} of 95.5% at −0.4 V *vs.* RHE, which is higher than that for Fe (68.3%) and Cu (47.7%) MMCs. The significantly enhanced

catalytic performance can be attributed to the fast proton and electron transfer induced by cooperative Fe–Cu and extra active pyridine N sites.[250] Moreover, He *et al.* synthesized an Fe–Cu DMC for electrocatalytic CO_2RR *via* an MOF-assisted approach. Firstly, the Cu^{2+} and $Fe(acac)_3$ molecules were *in situ*-doped in the ZIF-8 framework to form an Fe/Cu@ZIF-8 composite, in which the Zn^{2+} nodes were partially replaced by Cu^{2+}, and $Fe(acac)_3$ was encapsulated in the cavities of ZIF-8. Subsequently, Fe/Cu@ZIF-8 was pyrolyzed at 1000 °C under an Ar atmosphere to obtain Fe–Cu diatomic sites anchored on an N-doped porous carbon matrix. The aberration-corrected HAADF-STEM image showed many bright dual spots, suggesting the existence of diatomic sites. EELS further confirmed that the adjacent double spots were Fe and Cu atomic pairs. The XAS results demonstrated that the coordination structures of neighboring Fe and Cu sites were Fe–N_4 and Cu–N_3 linked by an Fe–Cu bond. Electrochemical investigations revealed that the Fe–Cu DMC exhibited excellent catalytic activity with the maximum FE_{CO} of 99.2% at −0.8 V (*vs.* RHE) and high TOF of 5047 h^{-1} at −1.1 V *vs.* RHE, which are higher than that of the corresponding Fe and Cu MMCs. DFT calculations revealed that the significantly improved catalytic efficiency of Fe–Cu DMC is due to the synergistic effect between the Fe–Cu diatomic pair, which promoted charge transfer and regulated the position of the d-band center, thus lowering the energy barriers for COOH* formation and CO* desorption.[251]

Besides Fe-based DMCs, Co-based DMCs have also been developed for electrocatalytic CO_2RR. For example, Zhuang *et al.* synthesized a Co–Ni DMC (Co–N–Ni/NPCNSs) *via* a two-step procedure for CO_2 electroreduction to CO. Firstly, porous carbon nanosheets (PCNSs) were obtained *via* the pyrolysis of cellulose. Then, a mixture of PCNSs, melamine and metal phthalocyanine was pyrolyzed at 1000 °C under an N_2 atmosphere to generate Co–N–Ni/NPCNSs. The aberration-corrected HAADF-STEM image revealed numerous bright dots in the carbon substrate, among which ∼70% were pairs, suggesting the Co–Ni bimetallic sites. EXAFS showed that both Co and Ni were coordinated with four N atoms and connected through one shared N atom. The electrocatalytic results of Co–N–Ni/NPCNSs demonstrated that the FE_{CO} was 96.4% at −0.48 V (*vs.* RHE), which is higher than that of the corresponding Co (66.5% at −0.57 V *vs.* RHE) and Ni (90.7% at −0.76 V *vs.* RHE) MMCs. The *in situ* synchrotron radiation Fourier transform infrared (SR-FTIR) measurements together with DFT calculations revealed that the N-bridged Co–N–Ni bimetallic sites could promote COOH* formation and accelerate CO* desorption, thus accounting for its excellent catalytic performance.[252]

Wu *et al.* synthesized a DMC comprised of Co–Cu pairs *via* the pyrolysis of cobalt acetate, copper acetate, carbon black and urea under an Ar atmosphere. The aberration-corrected HAADF-STEM images revealed many bright spot pairs on the support, suggesting the existence of Co–Cu pairs. The Co–Cu DMC was tested for electrocatalytic CO_2RR. Impressively, this catalyst showed ultrahigh activity with a maximum FE_{CO} of 99.1% and CO partial current density of 483 mA cm^{-1} in a flow cell, which are much better than that of Co and Cu MMCs. The current density delivered by Co–Cu DMC is higher than the industrial-relevant level (>200 mA cm^{-2}), demonstrating its potential for practical application. The excellent catalytic performance of this Co–Cu DMC is attributed to the synergistic effect between Co and Cu, which lowered the activation energy for the formation of the COOH* intermediate to promote CO production, as revealed by DFT calculations.[253]

Gong *et al.* reported the electronic effect between neighboring Co and Zn atoms in Co–Zn DMC (ZnCoNC) to facilitate electrocatalytic CO_2RR. ZnCoNC was synthesized by pyrolyzing a mixture of zinc nitrate, cobalt nitrate, carbamide, and activated carbon black, followed by nitric acid treatment to remove nanoclusters. The aberration-corrected HAADF-STEM and DFT calculations confirmed many Co–Zn atomic pairs anchored on N-doped carbon with a distance of 0.28 nm. ZnCoNC showed an outstanding catalytic performance with an FE_{CO} of 93.2% at −0.5 V (*vs.* RHE), which is higher than that for Co (56.3%) and Zn (67.3%) MMCs. Theoretical calculations further demonstrated that the energy barrier for the formation of the COOH* intermediate was lowered because of the electronic effect between Zn and Co, thus accounting for the high catalytic activity.[254]

Ni-based DMCs for electrocatalytic CO_2RR have also been developed. For instance, He *et al.* synthesized an Ni–Cu DMC *via* the one-step thermal activation of an $Ni(acac)_2$@ZnCu-ZIF composite (Fig. 18a). The aberration-corrected HAADF-STEM image showed atomically dispersed bright spot pairs, suggesting neighboring Ni and Cu atoms (Fig. 18b). EELS further confirmed the presence of Ni–Cu atomic pairs (Fig. 18c). The FT-EXAFS spectra revealed Ni–N and Cu–N coordination shells (Fig. 18d and e), and the coordination numbers of Ni–N and Cu–N were both 4. Moreover, the neighboring Ni–N_4 and Cu–N_4 were linked by two bridging N atoms. The Ni–Cu DMC presented a significantly increased catalytic performance for the CO_2RR with respect to the corresponding Ni and Cu MMCs, with an FE_{CO} of >95% from −0.39 to −1.09 V (*vs.* RHE) and maximum FE_{CO} of 99.2% and CO partial current density of 29.9 mA cm^{-2} at −0.79 V (*vs.* RHE) (Fig. 18f and g). DFT calculations revealed that the synergistic effect between Ni and Cu induced the charge redistribution of Ni to facilitate the formation of COOH* on Ni sites and to promote CO generation.[255] Furthermore, Li *et al.* prepared an Ni–Cu DMC for the CO_2RR *via* the pyrolysis of a mixture of carbon nanotubes, dicyandiamide, nickel chloride and copper chloride. The Ni–Cu DMC exhibited a high FE_{CO} of >90% over a wide potential range of −0.6 V to −0.9 V (*vs.* RHE), which was much more efficient than Ni and Cu MMCs. The enhanced catalytic efficiency of Ni–Cu DMC is ascribed to the synergy between Ni and Cu for promoting CO production.[256]

In addition to C_1 products, Ni–Cu DMCs can also be used as electrocatalysts for the reduction of CO_2 into multi-carbon products. For instance, Zhang *et al.* successfully decorated atomic Ni clusters on defect-rich Cu surface to form an Ni–Cu DMC for electrocatalytic CO_2 reduction into C_2 products. For the preparation of the Ni–Cu DMC, a defect-rich metallic copper was first synthesized by electrochemically reducing a

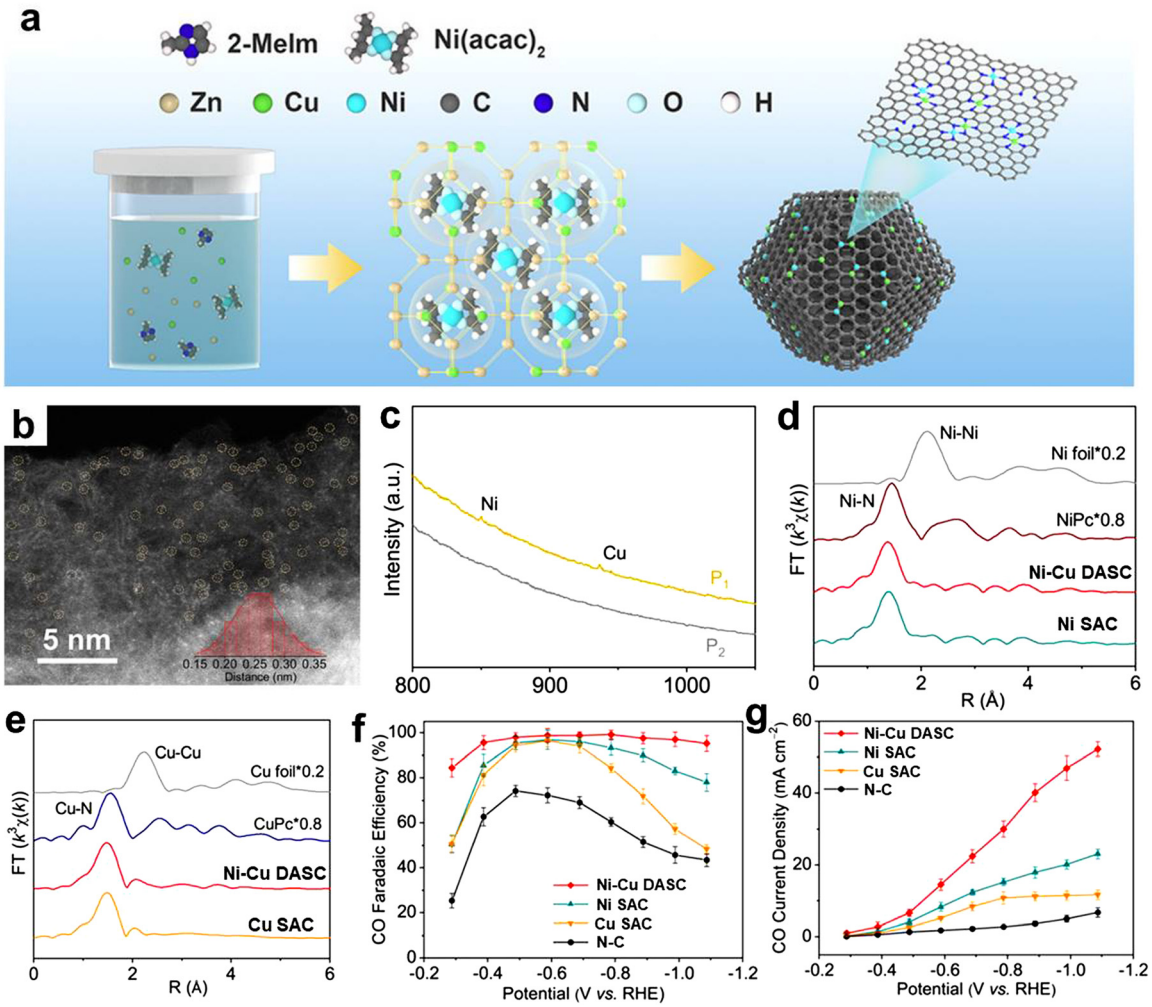

Fig. 18 (a) Schematic illustration of the synthesis of Ni–Cu DMC. (b) Aberration-corrected HAADF-STEM image of Ni–Cu DMC. (c) EELS spectra extracted from atomic pairs. (d) Ni K-edge FT-EXAFS spectra of Ni–Cu DMC, Ni MMC, NiPc and Ni foil. (e) Cu K-edge FT-EXAFS spectra of Ni–Cu DMC, Cu MMC, CuPc and Ni foil. (f) FE_{CO} and (g) CO partial current density of Ni–Cu DMC, Ni MMC, Cu MMC and N–C. Reproduced from ref. 255 with permission from the American Chemical Society, Copyright 2021.

copper sulfide layer, which was further immersed in an N_2-saturated nickel nitrate aqueous solution by a coordination-enabled galvanic replacement method to produce the Ni–Cu DMC. Energy-dispersive X-ray spectroscopy (EDS) and aberration-corrected HAADF-STEM revealed that Ni atoms were anchored on the surface of defect-rich Cu. The electrocatalytic results showed that the Ni–Cu DMC with an Ni/Cu ratio of 0.82% achieved a 7-fold improvement in selectivity for C_2 products with respect to pristine Cu, and the maximum FE for C_2 products was 62% at −0.88 V (*vs.* RHE). DFT calculations demonstrated that the Ni–Cu sites are preferable to adsorb and protonate CO_2 to form the COOH* intermediate. Further protonation of COOH* would occur at the Ni–Cu sites to accumulate CO* for C–C coupling.[257] Moreover, Hu *et al.* synthesized homogeneously alloyed Ni–Cu bimetallic nanoparticles ($Cu_{0.9}Ni_{0.1}$) *via* a non-equilibrium synthesis strategy for CO_2 electroreduction into C_{2+} products. Firstly, the carbon nanofibers containing copper nitrate and nickel nitrate were treated with an ultrashort current pulse, which were rapidly heated to >1300 °C for only 0.2 s, and then quickly cooled to room temperature to induce the mixing of Ni and Cu atoms. The obtained $Cu_{0.9}Ni_{0.1}$ showed a high FE of ~76% for C_{2+} products, which was ~20% higher than that of pure Cu.[258]

Lu *et al.* constructed an Ni–Zn DMC by pyrolyzing a mixture of chitosan, zinc chloride and nickel chloride, which was used as an electrocatalyst for the CO_2RR. The aberration-corrected HAADF-STEM image revealed that 76.2% of the atoms existed in the form of Ni–Zn atomic pairs with a distance of ~0.24 nm. The XAFS profile for this Ni–Zn DMC showed that both Ni and Zn were coordinated with three N atoms, and also coordinated with each other to form an Ni–Zn–N_6–C structure. The theoretical and experimental results further demonstrated that this heteronuclear coordination led to the modification of the d states of the metal atoms; hence, a pronounced synergistic effect between Ni and Zn, which induced a lower free energy barrier. Consequently, this Ni–Zn DMC showed a maximum FE_{CO} of 99% at −0.8 V (*vs.* RHE), which was higher than that of the corresponding Ni and Zn MMCs.[259]

Wei *et al.* prepared an Ni–Sn DMC *via* a two-step procedure, which displayed a synergistic effect to facilitate electrocatalytic CO_2 reduction into formate (Fig. 19a). Firstly, an N-doped carbon nanosheet array attached to a flexible carbon cloth was obtained *via* the pyrolysis of ZIF-8 and carbon cloth. Subsequently, the modified carbon cloth was suspended in nickel nitrate and stannous chloride ethanol solution for anchoring Ni^{2+} and Sn^{2+} ions, respectively, followed by pyrolysis treatment to form the Ni–Sn DMC (Fig. 19b). The aberration-corrected HAADF-STEM showed evenly dispersed bright spots, which were assigned to Ni and Sn atoms (Fig. 19c). The FT-EXAFS spectra displayed main peaks at 1.58 and 1.39 Å, corresponding to the Ni–N and Sn–N scattering paths, respectively (Fig. 19d and e). The EXAFS fitting further indicated that both Ni and Sn centers were coordinated with four N atoms to form $Ni–N_4$ and $Sn–N_4$ structures. The Ni-Sn DMC exhibited excellent activity with an $FE_{formate}$ of 86.1% at −0.82 V (*vs.* RHE) and TOF of 4752 h^{-1}, surpassing the corresponding Ni and Sn MMCs (Fig. 19f and g). DFT calculations indicated that the electron redistribution of Sn caused by adjacent Ni lowered the energy barrier of the *OCHO intermediate, and thus enhanced the catalytic performance.[260]

Park *et al.* fabricated a Bi–In nanosphere DMC ($In_{16}Bi_{84}$ NS) *via* a modified polyol method assisted by top-down and bottom-up processes for electrocatalytic CO_2RR. Firstly, indium metal was melted in the top-down process, and bismuth salt was reduced to generate metal bismuth. Then, the melted In droplets were fused with Bi with the assistance of polyvinylpyrrolidone to form $In_{16}Bi_{84}$ nanospheres (NSs). The mass loadings of In and Bi in $In_{16}Bi_{84}$ NS were determined *via* EDS analysis. The SEM and TEM images of $In_{16}Bi_{84}$ NS showed that the average size of the In–Bi nanospheres was ~300 nm. The obtained $In_{16}Bi_{84}$ NSs exhibited excellent activity for electrocatalytic CO_2RR with an $FE_{formate}$ of >90% over a wide

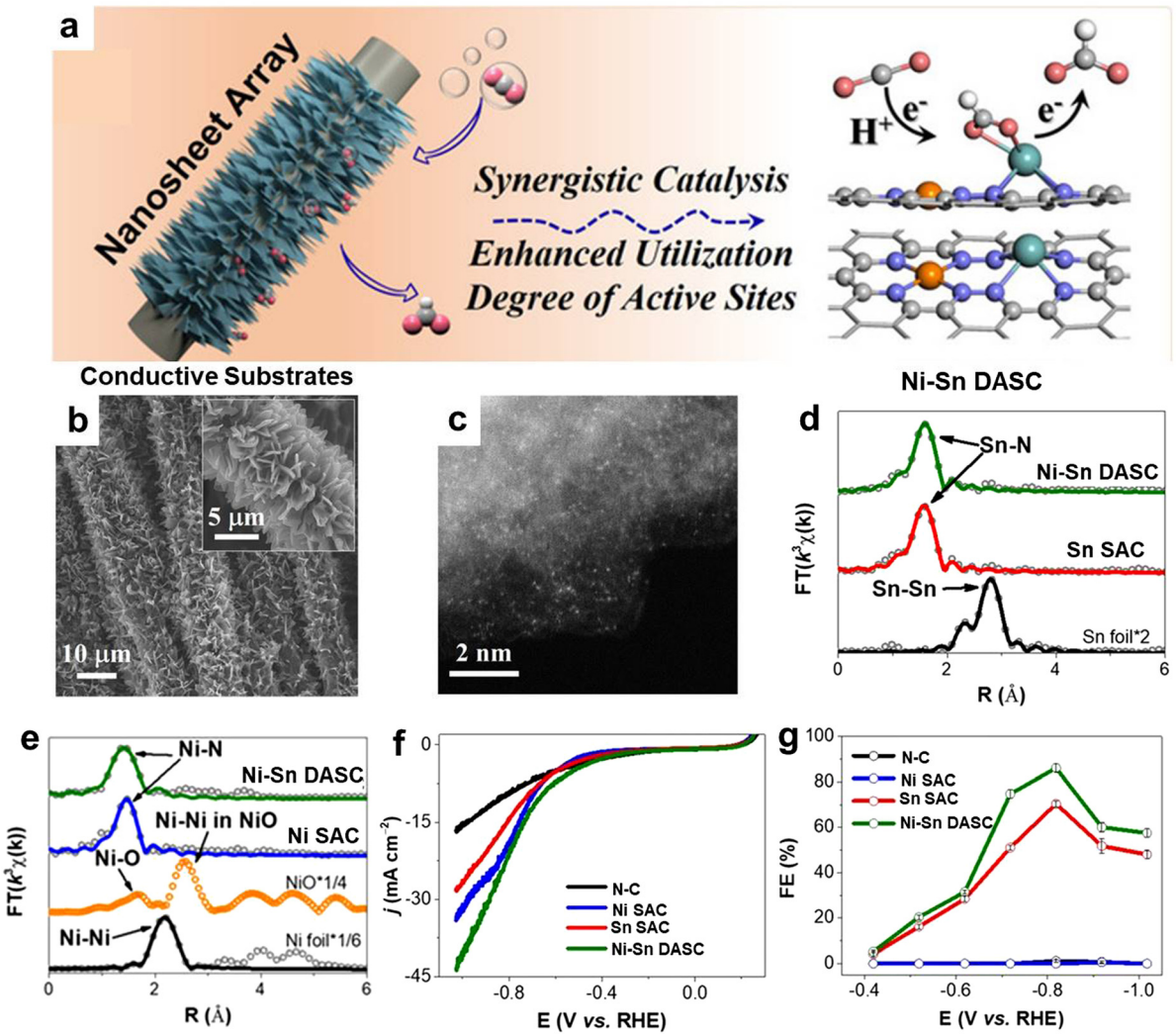

Fig. 19 (a) Schematic illustration showing the Ni–Sn DMC for synergistic electrocatalytic CO_2 reduction to formate. (b) SEM image of Ni–Sn DMC nanoarray. (c) Aberration-corrected HAADF-STEM image of Ni–Sn DMC. (d) Sn K-edge FT-EXAFS spectra of Ni–Sn DMC, Sn MMC and Sn foil. (e) Ni K-edge FT-EXAFS spectra of Ni–Sn DMC, Ni MMC, NiO and Ni foil. (f) LSV curves and (g) formate FEs for Ni–Sn DMC, Ni MMC, Sn MMC and N–C. Reproduced from ref. 260 with permission from Wiley-VCH, Copyright 2021.

potential window from −0.84 to −1.54 V (*vs.* RHE), with the maximum $FE_{formate}$ approaching 100% at −0.94 V. The superior catalytic performance of Bi–In DMC is attributed to the electronic synergistic effect between In and Bi to regulate the binding energy of intermediates, thus facilitating formate production.[261]

Chen *et al.* designed and synthesized a Bi–Sn DMC *via* the deposition of SnO_2 nanosheets on a flexible carbon support with a hydrothermal method, followed by the electrodeposition of Bi nanoparticles on the surface of the SnO_2 nanosheets. Benefiting from the active sites at the Bi–Sn interface, the Bi–Sn DMC exhibited high activity for electrocatalytic CO_2 reduction to formate with an FE of 96% at −1.1 V (*vs.* RHE), which is much higher than that for Bi and Sn MMCs. DFT calculations showed that the introduction of Bi nanoparticles upshifted both the p and d orbitals of the Sn electron states away from the Fermi level, which is conducive to stabilize the HCOO* intermediates and enhance the catalytic efficiency.[262]

Wang *et al.* prepared a series of Pd–Au DMCs for electrocatalytic CO_2RR by decorating Au nanoparticles with different Pd doses. Aberration-corrected HAADF-STEM, EELS and XAS characterization demonstrated that the Au nanoparticles were decorated with highly dispersed Pd atoms at low Pd doses ($Pd_2@Au_{98}$ and $Pd_5@Au_{95}$). With an increase in Pd dose, a semi-continuous Pd layer emerged ($Pd_{10}@Au_{90}$), and a Pd shell finally formed on the surface of the Au nanoparticle in the case of $Pd_{20}@Au_{80}$. The electrocatalytic results showed that all the Pd–Au DMCs could reduce CO_2 to CO, among which $Pd_5@Au_{95}$ displayed the highest activity with an FE_{CO} of ~80% and partial CO current density of 178 A g^{-1}_{metal} at −0.5 V (*vs.* RHE). Moreover, the catalytic performance of $Pd_5@Au_{95}$ was also higher than that for both pure Au and pure Pd. DFT calculations revealed that atomically dispersed Pd decorated on the Au nanoparticle surfaces lead to a lower energy barrier for CO_2 activation and are less likely to be poisoned by the *CO intermediate than pure Au and pure Pd, thus achieving the highest catalytic activity.[263]

4.5 N_2RR

4.5.1 Theoretical studies on DMCs for N_2RR. Researchers have carried out many simulations on the activation and reduction of N_2, particularly for the catalysts with dinuclear metal sites.[277–291] For example, Du *et al.* investigated the random combination of two types of metal atoms including Fe, Co, Mo, W and Ru to form DMCs. The calculation results showed that the energy barriers of these DMCs for the N_2RR are significantly decreased with respect to their mononuclear counterparts, indicating the much better activities of DMCs.[277] Huang *et al.* surveyed over 900 candidates of homonuclear DMCs as well as their heteronuclear counterparts supported on 2D phthalocyanine (Pc), and investigated their catalytic activity for the N_2RR. They found that three homonuclear DMCs and 28 heteronuclear DMCs can serve as highly active N_2RR catalysts. Particularly, five systems, including Ti_2–Pc, V_2–Pc, TiV–Pc, VCr–Pc, and VTa–Pc, have a favourable limiting potential of −0.75, −0.39, −0.74, −0.85, and −0.47 V, surpassing most of the reported electrocatalysts under acidic conditions.[278] Moreover, through first-principles high-throughput screening, Frauenheim *et al.* screened 23 metal centers *via* a "five-step" strategy (Fig. 20a), and picked Fe_2/g-CN featuring a high theoretical FE of 100% and the lowest limiting potential of −0.13 V (Fig. 20b). The high activity originated from the synergistic effects of metal dimers and g-CN, providing a favourable local environment for catalyzing the N_2RR. The thermodynamic results showed that the N_2RR processes prefer to proceed along the mixed pathway, that is, $*N_2 \rightarrow *NNH \rightarrow *NNH_2 \rightarrow *NHNH_2 \rightarrow *NHNH_3 \rightarrow *NH_2 \rightarrow *NH_3$ (Fig. 20c).[279]

4.5.2 Photocatalysis. Inspired by nitrogenase, Jiang *et al.* designed a series of U(Zr–Hf)-X catalysts *via* the modularization of UiO-66-based MOFs containing Zr–Hf bimetallic nodes and organic ligands with different functional groups (X = –Cl, –OH or –SH) to implement visible-light-driven photocatalytic N_2 fixation. The optimal photocatalyst U(Zr–Hf)-SH (Zr : Hf = 1 : 1) achieved the highest performance for N_2 reduction into NH_3, with the formation rate of 116.1 μmol g^{-1} h^{-1}. The mechanism studies revealed that the high catalytic performance of U(Zr–Hf)-SH can be ascribed to the synergistic effect between Zr and Hf; specifically, Zr serves as the active site to adsorb N_2, and Hf acts as an electron buffer tank to optimize the electron transfer and utilization. The –SH functional group in the organic ligand, which extended the absorption edge of the photocatalyst to the

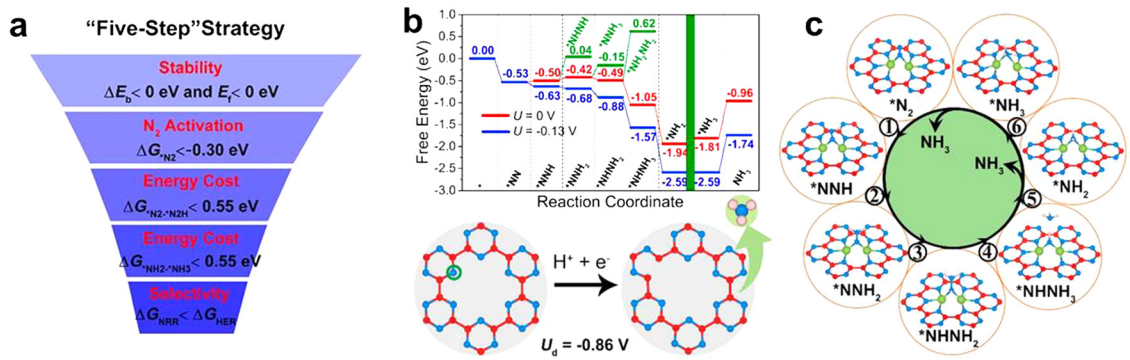

Fig. 20 (a) Proposed "five-step" strategy for screening N_2RR candidate catalysts. (b) Free energy diagrams of Fe_2/g-CN, and the decomposition energy of the substrate g-CN. (c) Adsorption structures during the N_2RR on Fe_2/g-CN through the minimum energy pathway. Reproduced from ref. 279 with permission from the American Chemical Society, Copyright 2021.

visible region, also contributed to the enhanced activity.[283] Furthermore, Xiong *et al.* found that doping Mo species in defect-rich $W_{18}O_{49}$ ultrathin nanowires could result in an excellent photocatalyst for N_2 reduction into ammonia. In Mo-doped $W_{18}O_{49}$, the Mo–W centers served as the active sites synergistically chemisorbing N_2 molecules, thus facilitating N_2 activation. The doped Mo species also improved the defect states in $W_{18}O_{49}$, which is beneficial for the photocatalytic N_2RR. Consequently, 1 mol% Mo-doped $W_{18}O_{49}$ achieved an ammonia production rate of 195.5 μmol g_{cat}^{-1} h^{-1}, which is 7-fold higher than that of pristine $W_{18}O_{49}$.[284]

Jin *et al.* synthesized a zinc-based coordination polymer with bridging dinitrogen anionic ligands, $\{[Zn(L)(N_2)_{0.5}(TCNQ\text{-}TCNQ)_{0.5}]\cdot(TCNQ)_{0.5}\}_n$ (NJUZ-1, L = tetra(isoquinolin-6-yl)-tetrathiafulvalene, TCNQ = tetracyanoquinodimethane), which can be used as an efficient photocatalyst for nitrogen fixation in an ambient environment without any external electron-sacrificial reagent. The secondary building units (SBUs) of NJUZ-1 consisted of two bilateral zinc centers and an end-on dinitrogen block, which were further linked by L to form a 3D framework with TCNQ guest molecules (Fig. 21a and b). DFT calculations demonstrated that the N≡N stretching vibration in the Zn–N_2–Zn structure is at 1937 cm^{-1} (Fig. 21c). The Raman spectrum of ^{15}N isotope-labelled NJUZ-1 showed a peak at 1920 cm^{-1}, corresponding to the $^{15}N{\equiv}{}^{15}N$ stretching vibration (Fig. 21d). These results suggest the presence of a bridge-coordinated dinitrogen anion in NJUZ-1. The photocatalytic results showed that NJUZ-1 displayed an ammonia conversion rate of 140 μmol g^{-1} h^{-1} in pure N_2, and also achieved an ammonia yield rate of 102.40 μmol g^{-1} h^{-1} in air in deionized water (Fig. 21e). O_2 was the only by-product detected by gas chromatography. The control experiments and theoretical calculations showed that the active [Zn^{2+}–(N≡N)–Zn^{2+}] sites in NJUZ-1 can facilitate the formation of NH_3, and the detachment

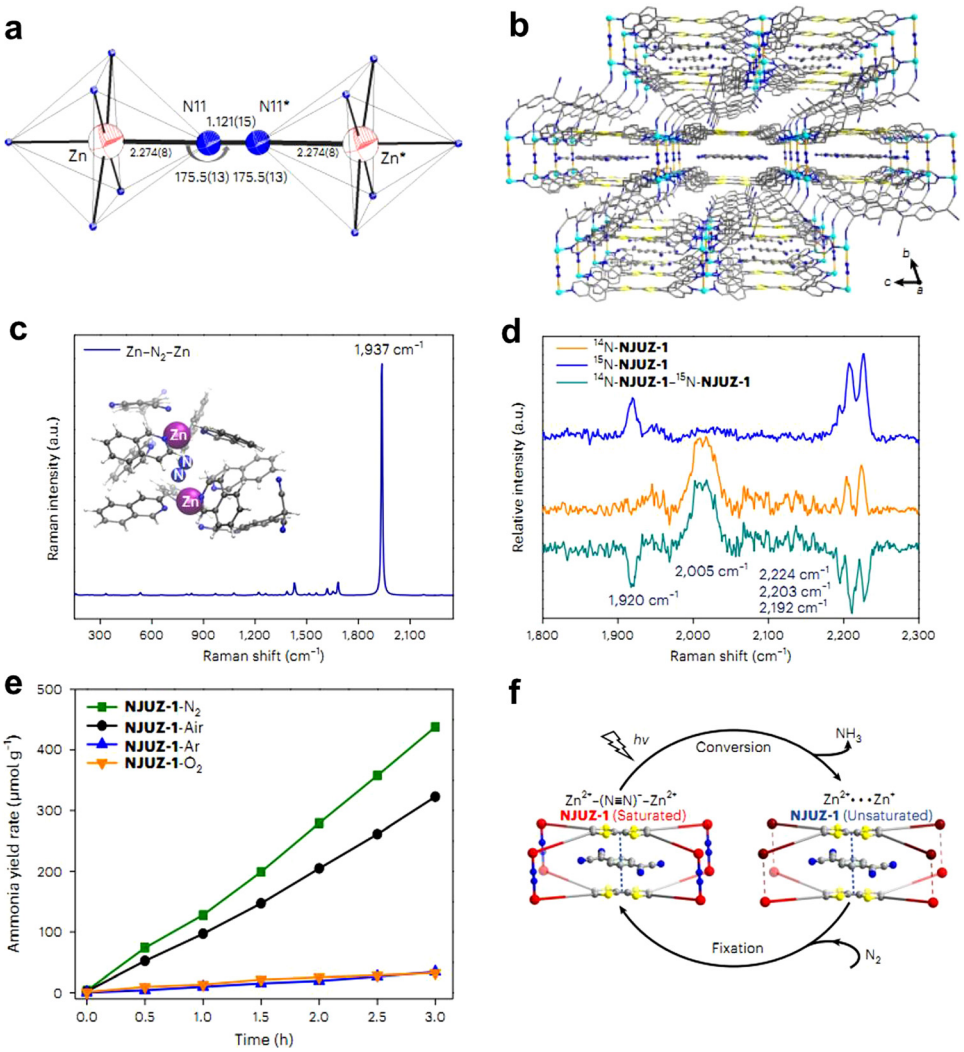

Fig. 21 (a) SBU of the $[Zn_2N_2]$-based NJUZ-1 coordination polymer. (b) 3D framework of NJUZ-1 1 with TCNQ guest molecules. (c) Simulated Raman spectrum of the Zn–N_2–Zn structure by DFT. (d) Raman spectra of ^{14}N-NJUZ-1 and ^{15}N-NJUZ-1. (e) Ammonia yield rates of NJUZ-1 in deionized water saturated by pure N_2, air, Ar or O_2 flow. (f) Scheme of the cycling process of NJUZ-1 during the photocatalytic N_2RR process. Reproduced from ref. 285 with permission from Springer Nature, Copyright 2023.

of the yielded NH_3 created an unsaturated reactive [$Zn^{2+}\cdots Zn^{+}$] intermediate, which could be populated by N_2 (Fig. 21f).[285]

4.5.3 Electrocatalysis. In 2020, Liang *et al.* successfully confined multiple Fe and Cu atoms in the surface cavities of graphitic carbon nitride (CNT@C_3N_4–Fe&Cu) by annealing a mixture of carbon nanotubes (CNTs), dicyandiamide (DICY), $FeCl_2$ and $CuCl_2$. The aberration-corrected HAADF-STEM image showed numerous compact bright spots with an average distance of 1.8–2.5 Å, suggesting the single-atom character of Fe and Cu. In the EELS spectra, two peaks appeared at ~710 and 940 eV, which were attributed to Fe and Cu, respectively. The FT-EXAFS *R*-space spectra of Fe and Cu displayed metal–metal coordination, implying the existence of Fe–Fe or Fe–Cu bonds. The resultant CNT@C_3N_4-Fe&Cu could be used as an efficient electrocatalyst for the N_2RR with an FE of 34.0% (*vs.* Ag/AgCl), which was higher than that of its Fe (15.3%) and Cu (22.0%) single-metallic counterparts. DFT calculations revealed that the synergistic effect between Fe and Cu could accelerate the N_2 adsorption and lower the energy barrier, thereby promoting the N_2RR.[286] Moreover, Cheng *et al.* synthesized a diatomic Zn/Fe–N–C catalyst *via* the pyrolysis of chitosan, zinc chloride and ferrous acetate, followed by acidic etching to remove the Fe and Zn nanoparticles. Numerous bright dual dots were observed, which were assigned to Fe and Zn atomic pairs, as indicated by aberration-corrected HAADF-STEM. The FT-EXAFS curves of the Fe and Zn K-edges showed Fe–N, Zn–N and Fe–Zn scattering paths. EXAFS fitting indicated a $ZnFeN_6$ structure in the diatomic Zn/Fe–N–C catalyst. The synthesized Zn/Fe–N–C exhibited excellent activity for the N_2RR with the NH_3 yield rate of 30.5 μg h^{-1} mg_{cat}^{-1} and FE of 26.5% at −0.3 V (*vs.* RHE), which are superior to that of Fe–N–C and Zn–N–C MMCs. DFT calculations demonstrated that the Fe atoms serve as the active centers, and the Zn atoms regulate the electronic structures of Fe to promote N_2 activation and lower the reaction barrier of the RDS of *NNH formation.[287]

Cho *et al.* synthesized an FeMo-PC (PC, phosphorus-doped carbon) catalyst *via* one-step pyrolysis-phosphating of bimetallic FeMo-MOFs. The aberration-corrected HAADF-STEM image and corresponding elemental mappings showed the uniform distribution of Fe and Mo in FeMo-PC. The FT-EXAFS spectrum of Fe K-edge demonstrated two main peaks centered at 1.29 and 1.71 Å, corresponding to the Fe–O and Fe–P bonds, respectively. In the Mo K-edge, three main peaks centered at 1.17, 1.57 and 2.27 Å were observed, which were assigned to Mo–O, Mo–P and Mo–Mo paths, respectively. The electrochemical N_2RR tests showed that FeMo-PC achieved a high NH_3 formation rate of 34.23 μg h^{-1} $mg_{cat.}^{-1}$ and FE of 16.83% at −0.5 V (*vs.* RHE), which is superior to that of the single-metal Fe-C (17.83 μg h^{-1} $mg_{cat.}^{-1}$; FE, 7.69%) and Mo-C (12.52 μg h^{-1} $mg_{cat.}^{-1}$; FE, 9.67%) catalysts.[288] Furthermore, Luo *et al.* constructed an Fe–Mo DMC (MoFe@NG) *via* the pyrolysis of a mixture of glucose, dicyandiamide, $FeCl_3$, $FeCl_2$ and $MoCl_5$. The aberration-corrected HAADF-STEM images showed many bright dots anchored on the N-doped graphene support, corresponding to Fe and Mo single atoms, as further confirmed by XANES. Benefiting from the synergistic effect between Fe and Mo atoms, MoFe@NG exhibited outstanding electrocatalytic N_2RR activity for the reduction of N_2 into ammonia with a yield rate of 14.95 μg h^{-1} $mg_{cat.}^{-1}$ at −0.4 V (*vs.* RHE) and FE of 41.7% at −0.2 V (*vs.* RHE). The catalytic activity of MoFe@NG was significantly better than that of Fe@NG and Mo@NG MMCs. DFT calculations demonstrated that the N-coordinated FeMo dimer in MoFe@NG is conducive to weaken the N≡N bond and lower the N_2RR energy barrier to facilitate N_2 reduction.[289]

Wang *et al.* demonstrated the theory-guided design of an MoSA-Mo_2C/NCNT composite by combining Mo single atoms (MoSAs) and Mo carbide particles (Mo_2C) on the same N-doped carbon nanotubes. The aberration-corrected HAADF-STEM image showed that numerous isolated Mo single atoms were dispersed around Mo_2C nanoparticles. The FT-EXAFS spectra of MoSAs-Mo_2C/NCNTs and Mo_2C/NCNTs displayed a dominant peak at 2.6 Å, which can be assigned to the Mo–Mo coordination. In the FT-EXAFS spectrum of MoSAs/NCNTs, a main peak at about 1.3 Å was observed, corresponding to the Mo–N/C scattering path. These results confirmed the successful formation of the desired materials. The MoSAs-Mo_2C/NCNTs exhibited outstanding N_2RR activity with an ammonia formation rate of 16.1 μg h^{-1} $cm_{cat.}^{-2}$ at −0.25 V (*vs.* RHE), which was 4- and 4.5-times higher than that of Mo_2C/NCNTs and MoSAs/NCNTs, respectively. The corresponding FE of MoSAs-Mo_2C/NCNTs (7.1%) was 2- and 7-times higher than that of Mo_2C/NCNTs and MoSAs/NCNTs, respectively. The significantly enhanced catalytic efficiency of MoSAs-Mo_2C/NCNTs can be attributed to the synergy of MoSAs and Mo_2C, which can effectively mediate the complex multi-step N_2RR processes.[290] Furthermore, Chu *et al.* constructed a bimetallic $MnMoO_4$/rGO N_2RR catalyst *via* the facile microwave-assisted hydrothermal reaction of $Na_2MoO_4{\cdot}2H_2O$, $Mn(CH_3COO)_2{\cdot}4H_2O$ and graphene oxide (GO). The HRTEM image of $MnMoO_4$/rGO showed an interplanar spacing of 0.356 nm, corresponding to the (220) plane of $MnMoO_4$. XPS analysis of $MnMoO_4$/rGO revealed that the valence states of Mn and Mo were +2 and +6, respectively. $MnMoO_4$/rGO presented excellent catalytic activity with the NH_3 production rate of 60.3 μg h^{-1} mg^{-1} and FE of 14.7%, surpassing the corresponding Mn and Mo-based N_2RR catalysts. DFT calculations revealed that the Mn and Mo atoms in $MnMoO_4$/rGO serve as dual active centers to synergistically promote the N_2RR.[291]

Xin *et al.* synthesized a Pd–Cu DMC (PdCu/NC) by pyrolyzing a mixture of $Cl_2H_{14}N_4OPd$, $CuCl_2$, $NH_2OH{\cdot}HCl$ and glucose at 600 °C. The aberration-corrected HAADF-STEM images showed numerous isolated bright dots anchored on a carbon support (Fig. 22a), among which some atomic pairs were observed, corresponding to diatomic Pd–Cu sites (Fig. 22b). The Pd K-edge FT-EXAFS spectrum of PdCu/NC presented a main peak at 1.46 Å, which can be assigned to Pd–N coordination (Fig. 22c). In the Cu K-edge FT-EXAFS spectrum, a main peak at 1.47 Å was observed, which was attributed to Cu–N coordination (Fig. 22d). The resulting PdCu/NC could be used as an outstanding electrocatalyst for the reduction of N_2 into NH_3 with the high yield rate of 69.2 μg h^{-1} $mg_{cat.}^{-1}$, which is 4.2- and 3.0-times higher than that of Pd/NC and Cu/NC, respectively (Fig. 22e). Moreover, the FE_{NH3} for PdCu/NC was

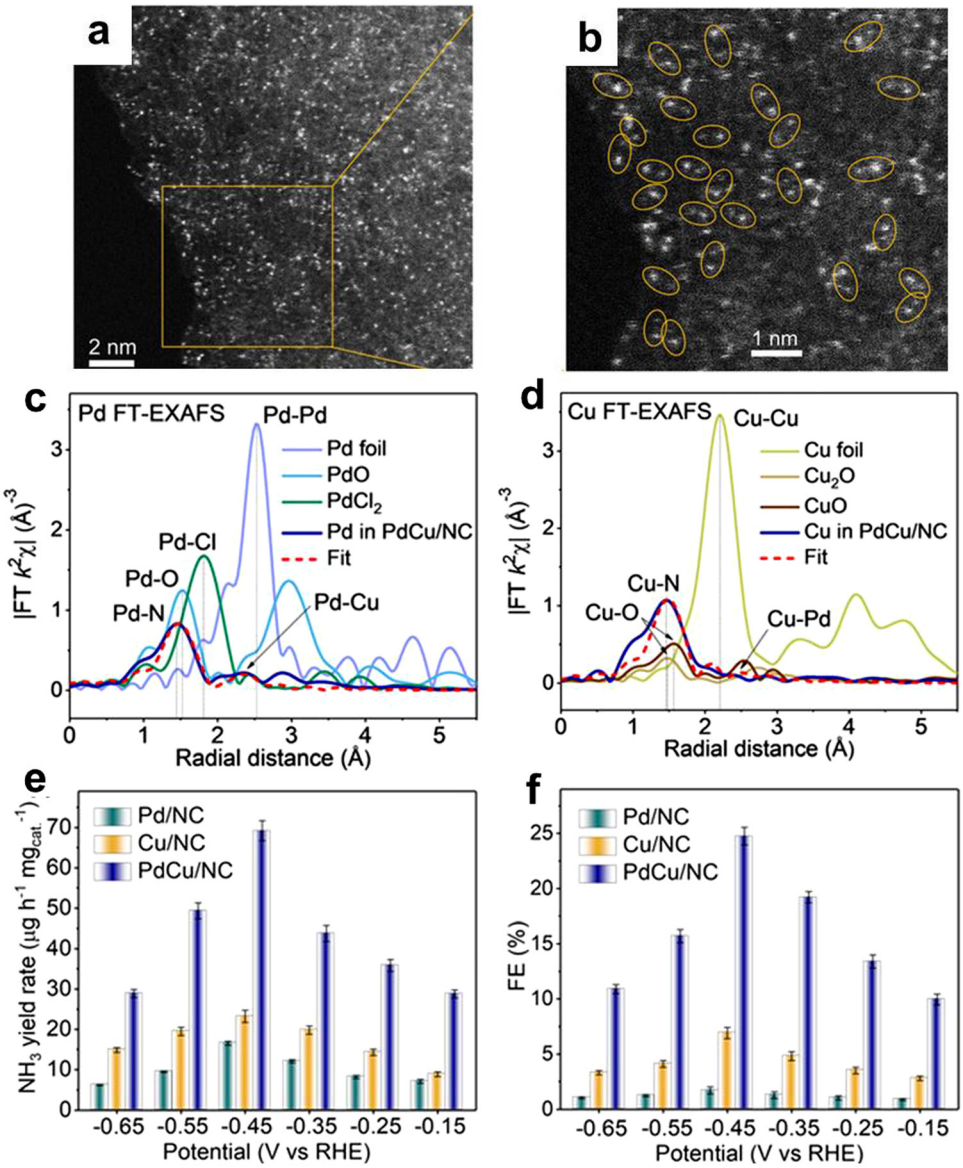

Fig. 22 (a) Aberration-corrected HAADF-STEM image of PdCu/NC. (b) Magnified aberration-corrected HAADF-STEM image of PdCu/NC, showing diatomic Pd–Cu sites highlighted by yellow circles. (c) Pd K-edge and (d) Cu K-edge FT-EXAFS spectra of PdCu/NC and reference samples. (e) NH_3 yield rates and (f) FEs of PdCu/NC, Pd/NC, and Cu/NC in N_2-saturated 0.05 M H_2SO_4. Reproduced from ref. 292 with permission from Wiley-VCH, Copyright 2021.

24.8% at −0.45 V (*vs.* RHE), which is 14.6- and 3.6-times that of Pd/NC and Cu/NC, respectively (Fig. 22f). DFT calculations revealed that the introduction of Cu shifted the partial density of states (pDOS) of Pd toward the Fermi level and facilitated the d–2π*coupling between Pd and adsorbed N_2, thus enhancing the catalytic activity for the N_2RR.[292]

Employing DFT calculations, Zheng *et al.* first revealed that the adjacent Ti^{3+} diatomic pairs on anatase TiO_2 can be used as active electrocatalytic centers for N_2 chemisorption and activation. Subsequently, Zr^{4+} ions were doped in the TiO_2 support by exchanging Ti^{4+} ions with Zr^{4+} on account of their similar d-electron configurations and oxide structures, as well as suitable sizes. The aberration-corrected HAADF-STEM image revealed some individual Zr^{4+} ions, which occupied the original positions of Ti^{4+} ions. The Ti K-edge FT-EXAFS spectrum of Zr-doped TiO_2 showed two main peaks at 1.34 and 2.41 Å, corresponding to Ti–O and Ti–Ti bonds, respectively. The Zr K-edge FT-EXAFS spectrum showed only a Zr–O scattering path at 1.52 Å, suggesting the single-atomic distribution of Zr^{4+}. The Zr^{4+}-doped anatase TiO_2 exhibited excellent activity for electrocatalytic N_2RR with the ammonia production rate of 8.90 μg h^{-1} cm^{-2} and FE of 17.3% at −0.45 V (*vs.* RHE), surpassing that of the undoped TiO_2 (1.48 μg h^{-1} cm^{-2} at −0.65 V *vs.* RHE). The significantly improved catalytic activity was attributed to the increased number of oxygen vacancies induced by introduction of Zr^{4+} ions.[293] Moreover, Chu *et al.*

constructed foordite $SnNb_2O_6$ nanosheets *via* the hydrothermal reaction of $Nb_2O_5{\cdot}nH_2O$ and $SnCl_2{\cdot}2H_2O$ for electrocatalytic N_2RR. The obtained $SnNb_2O_6$ exhibited high catalytic activity with the NH_3 yield of 53.1 mg h^{-1} mg^{-1} and FE of 17.6% at −0.3 V (*vs.* RHE). DFT calculations revealed that the dual active centers of Nb_{3c} and Sn_{4c}–Nb_{5c} dimer synergistically promoted N_2 adsorption and activation and lowered the energy barrier for the RDS, thereby boosting the electrocatalytic activity.[294]

5. Conclusions and outlook

Herein, we reviewed the major achievements regarding dinuclear metal catalysts in five typical energy conversion reactions, that is, hydrogen evolution reaction, oxygen evolution reaction, oxygen reduction reaction, CO_2 reduction reaction, and N_2 reduction reaction. Particularly, we focused on the analysis of the relationship between the structures and the performances of dinuclear metal catalysts. Based on the above discussion, it can be seen that the dinuclear metal sites in catalysts with appropriate spatial separations and geometric configurations can synergistically bind with substrate molecules by coordination interactions and optimize the adsorption and stability of the reaction substrates/intermediates, thus greatly boosting the energy conversion reactions. We also delineated the synergistic catalytic mechanisms of dinuclear sites in elevating the catalytic performances.

However, it should be noted that simply bringing two metal atoms in proximity does not necessarily give rise to the dinuclear metal synergistic catalysis effect and a superior performance. In most cases, the two metal atoms need to be immobilized at an appropriate separation distance and oriented in a proper geometric configuration to exert synergistic interactions on the substrate molecules, intermediate species or products. For homogeneous catalysts, this requires the sophisticated and delicate design of the ligand structure, for which theoretical calculations such as DFT and molecular dynamics simulation can be beneficial. For heterogeneous catalysts, the relevant research is still in its infancy, and available synthesis techniques that can reliably lead to the formation of diatomic metal sites are still limited. In this regard, preparation methods based on reticular chemistry and atomic layer deposition can enable structural control at the atomic level with moderate to high precision, and thus may offer new opportunities for constructing diatomic metal sites in a predictable and controllable manner. Regarding the mechanisms of dinuclear metal synergistic catalysis in the five energy conversion reactions mentioned above, although theoretical calculations have proven to be powerful tools for deciphering the complicated catalytic pathways, experimental observations can provide more direct and convincing evidence. Therefore, the importance of *in situ*/*operando* characterization techniques is becoming prominent. Presently, these techniques include optical spectroscopy (such as X-ray absorption spectroscopy, infrared spectroscopy, and Raman spectroscopy), electron spectroscopy (such as X-ray photoelectron spectroscopy, ultraviolet photoelectron spectroscopy, and electron energy loss spectroscopy) and electron microscopy (such as aberration-corrected high-angle annular dark-field scanning transmission electron microscopy), offering new in-depth insights into the adsorption/desorption, bond cleavage/formation and proton/electron transfer during the catalytic process.

It was also concluded that although considerable progress on dinuclear metal catalysts for energy conversion reactions has been achieved, the related research is still in the early stage. Firstly, there is a lack of general methods for the synthesis of dinuclear metal catalysts with high precision, especially heterogeneous dinuclear metal catalysts. Loading dinuclear metal complex precursors on supports with a subsequent pyrolysis process is the most common method to prepare dinuclear metal catalysts; however, the pyrolysis process often leads the migration of the metal centers, and therefore the structural unit of the dinuclear metal center may be impaired and cannot be intactly inherited by the as-obtained catalyst. Consequently, besides dinuclear metal catalytic sites, mononuclear metal ones usually appear, and the metal centers may even aggregate to form metal clusters and nanoparticles. Thus, the pyrolysis conditions including the temperature and atmosphere need be finely tuned. Secondly, the precise structures of most heterogeneous dinuclear metal catalysts are difficult to be determined, given that most of them (particularly when obtained *via* pyrolysis) are of poor long-range order. Although the local coordination environment around the dinuclear metal centers can be inferred *via* X-ray absorption spectroscopy, the microenvironments around the dinuclear metal coordination structure that may directly affect the catalytic activity are unclear, hindering the identification of structure–performance relationship of catalysts at the atomic/molecular level. Thirdly, there is a lack of design principles for dinuclear metal catalysts with outstanding catalytic performance for energy conversion reactions. Limited by the unclear structures, the mechanisms of dinuclear metal catalysts for a specific energy conversion reaction are also obscure. In summary, there is still a long way to go to achieve the precise design and synthesis of dinuclear metal catalysts with high performances, well-defined structures and well-recognized catalysis mechanisms for energy conversion reactions. Nevertheless, the recent studies summarized in this review clearly evidenced that the dinuclear metal catalysts feature unique superiority for energy conversion reactions, and the development of dinuclear metal catalysts is becoming a hot research area, with more marvels to be expected.

Author contributions

The manuscript was discussed and written through contributions of all authors.

Conflicts of interest

There are no conflicts to declare.

Acknowledgements

We are grateful for the financial support from the National Key R&D Program of China (2022YFA1502902), the National Natural Science Foundation of China (21931007, 22071182, 22001043 and 22271218).

References

1 S. Chu and A. Majumdar, *Nature*, 2012, **488**, 294–303.
2 Z. Luo, T. Wang and J. Gong, *Chem. Soc. Rev.*, 2019, **48**, 2158–2181.
3 W. Zhang, W. Lai and R. Cao, *Chem. Rev.*, 2017, **117**, 3717–3797.
4 A. J. Carrillo, J. González-Aguilar, M. Romero and J. M. Coronado, *Chem. Rev.*, 2019, **119**, 4777–4816.
5 G. Wang, J. Chen, Y. Ding, P. Cai, L. Yi, Y. Li, C. Tu, Y. Hou, Z. Wen and L. Dai, *Chem. Soc. Rev.*, 2021, **50**, 4993–5061.
6 K. Matuszek, M. Kar, J. M. Pringle and D. R. MacFarlane, *Chem. Rev.*, 2023, **123**, 491–514.
7 H.-F. Wang, L. Chen, H. Pang, S. Kaskel and Q. Xu, *Chem. Soc. Rev.*, 2020, **49**, 1414–1448.
8 X.-P. Zhang, A. Chandra, Y.-M. Lee, R. Cao, K. Ray and W. Nam, *Chem. Soc. Rev.*, 2021, **50**, 4804–4811.
9 X. Li, H. Lei, L. Xie, N. Wang, W. Zhang and R. Cao, *Acc. Chem. Res.*, 2022, **55**, 878–892.
10 H. Ding, H. Liu, W. Chu, C. Wu and Y. Xie, *Chem. Rev.*, 2021, **121**, 13174–13212.
11 L. Huang, S. Zaman, X. Tian, Z. Wang, W. Fang and B. Y. Xia, *Acc. Chem. Res.*, 2021, **54**, 311–322.
12 J.-W. Wang, W.-J. Liu, D.-C. Zhong and T.-B. Lu, *Coord. Chem. Rev.*, 2019, **378**, 237–261.
13 C. Tang and S.-Z. Qiao, *Chem. Soc. Rev.*, 2019, **48**, 3166–3180.
14 C. Kim, F. Dionigi, V. Beermann, X. Wang, T. Möller and P. Strasser, *Adv. Mater.*, 2019, **31**, 1805617.
15 Y. Li, N. Wang, H. Lei, X. Li, H. Zheng, H. Wang, W. Zhang and R. Cao, *Coord. Chem. Rev.*, 2021, **442**, 213996.
16 X.-P. Zhang, H.-Y. Wang, H. Zheng, W. Zhang and R. Cao, *Chin. J. Catal.*, 2021, **42**, 1253–1268.
17 J. Pritchard, G. A. Filonenko, R. Putten, E. J. M. Hensen and E. A. Pidko, *Chem. Soc. Rev.*, 2015, **44**, 3808–3833.
18 J. Li, M. F. Stephanopoulos and Y. Xia, *Chem. Rev.*, 2020, **120**, 11699–11702.
19 S. Zhang, Q. Fan, R. Xia and T. J. Meyer, *Acc. Chem. Res.*, 2020, **53**, 255–264.
20 N. Elgrishi, M. B. Chambers, X. Wang and M. Fontecave, *Chem. Soc. Rev.*, 2017, **46**, 761–796.
21 L. Chen, G. Chen, C.-F. Leung, C. Cometto, M. Robert and T.-C. Lau, *Chem. Soc. Rev.*, 2020, **49**, 7271–7283.
22 S.-T. Bai, G. D. Smet, Y. Liao, R. Sun, C. Zhou, M. Beller, B. U. W. Maes and B. F. Sels, *Chem. Soc. Rev.*, 2021, **50**, 4259–4298.
23 D.-C. Liu, D.-C. Zhong and T.-B. Lu, *EneryChem*, 2020, **2**, 100034.
24 B. Zhang and L. Sun, *Chem. Soc. Rev.*, 2019, **48**, 2216–2264.
25 K. Koshiba, K. Yamauchi and K. Sakai, *Angew. Chem., Int. Ed.*, 2017, **56**, 4247–4251.
26 X. Zhang, K. Yamauchi and K. Sakai, *ACS Catal.*, 2021, **11**, 10436–10449.
27 C. Cometto, R. Kuriki, L. Chen, K. Maeda, T.-C. Lau, O. Ishitani and M. Robert, *J. Am. Chem. Soc.*, 2018, **140**, 7437–7440.
28 M. Wang, L. Chen, T.-C. Lau and M. Robert, *Angew. Chem., Int. Ed.*, 2018, **57**, 7769–7773.
29 H. Rao, L. C. Schmidt, J. Bonin and M. Robert, *Nature*, 2017, **548**, 74–77.
30 S. Ren, D. Joulié, D. A. Salvatore, K. Torbensen, M. Wang, M. Robert and C. P. Berlinguette, *Science*, 2019, **365**, 367–369.
31 P. B. Pati, R. Wang, E. Boutin, S. Diring, S. Jobic, N. Barreau, F. Odobel and M. Robert, *Nat. Commun.*, 2020, **11**, 3499.
32 J.-W. Wang, K. Yamauchi, H.-H. Huang, J.-K. Sun, Z.-M. Luo, D.-C. Zhong, T.-B. Lu and K. Sakai, *Angew. Chem., Int. Ed.*, 2019, **58**, 10923–10927.
33 J.-W. Wang, H.-H. Huang, J.-K. Sun, D.-C. Zhong and T.-B. Lu, *ACS Catal.*, 2018, **8**, 7612–7620.
34 L. Wang, L. Duan, Y. Wang, M. Ahlquist and L. Sun, *Chem. Commun.*, 2014, **50**, 12947–12950.
35 B. Zhang and L. Sun, *J. Am. Chem. Soc.*, 2019, **141**, 5565–5580.
36 Z. Lu, Y. Gao, H. Chen, Z. Liu, L. Chen and L. Sun, *Angew. Chem., Int. Ed.*, 2016, **5**, 12683–12687.
37 D.-C. Liu, H.-J. Wang, J.-W. Wang, D.-C. Zhong, L. Jiang and T.-B. Lu, *Chem. Commun.*, 2018, **54**, 11308–11311.
38 W.-J. Liu, H.-H. Huang, T. Ouyang, L. Jiang, D.-C. Zhong, W. Zhang and T.-B. Lu, *Chem. – Eur. J.*, 2018, **24**, 4503–4508.
39 D.-C. Liu, H.-H. Huang, J.-W. Wang, L. Jiang, D.-C. Zhong and T.-B. Lu, *ChemCatChem*, 2018, **10**, 3435–3440.
40 J.-W. Wang, H.-H. Huang, J.-K. Sun, T. Ouyang, D.-C. Zhong and T.-B. Lu, *ChemSusChem*, 2018, **11**, 1025–1031.
41 T. Ouyang, C. Hou, J.-W. Wang, W.-J. Liu, D.-C. Zhong, Z.-F. Ke and T.-B. Lu, *Inorg. Chem.*, 2017, **56**, 7307–7311.
42 T. Ouyang, H.-H. Huang, J.-W. Wang, D.-C. Zhong and T.-B. Lu, *Angew. Chem., Int. Ed.*, 2017, **56**, 738–743.
43 T. Ouyang, H.-J. Wang, H.-H. Huang, J.-W. Wang, S. Guo, W.-J. Liu, D.-C. Zhong and T.-B. Lu, *Angew. Chem., Int. Ed.*, 2018, **57**, 16480–16485.
44 B. Wang, G. M. Biesold, M. Zhang and Z. Lin, *Chem. Soc. Rev.*, 2021, **50**, 6914–6949.
45 A. Bavykina, N. Kolobov, S. Khan, J. A. Bau, A. Ramirez and J. Gascon, *Chem. Rev.*, 2020, **120**, 8468–8535.
46 H. Wang, H. Wang, Z. Wang, L. Tang, G. Zeng, P. Xu, M. Chen, T. Xiong, C. Zhou, X. Li, D. Huang, Y. Zhu, Z. Wang and J. Tang, *Chem. Soc. Rev.*, 2020, **49**, 4135–4165.
47 C. Tang, M. Cheng, C. Lai, L. Li, X. Yang, L. Du, G. Zhang, G. Wang and L. Yang, *Coord. Chem. Rev.*, 2023, **474**, 214846.
48 H.-J. Son, C. Pac and S. O. Kang, *Acc. Chem. Res.*, 2021, **54**, 4530–4544.
49 L. Jiao, Y. Wang, H.-L. Jiang and Q. Xu, *Adv. Mater.*, 2018, **30**, 1703663.

50 R.-B. Lin, Y. He, P. Li, H. Wang, W. Zhou and B. Chen, *Chem. Soc. Rev.*, 2019, **48**, 1362–1389.
51 Y. He, S. Liu, C. Priest, Q. Shi and G. Wu, *Chem. Soc. Rev.*, 2020, **49**, 3484–3524.
52 W. Jing, H. Shen, R. Qin, Q. Wu, K. Liu and N. Zheng, *Chem. Rev.*, 2022, DOI: **10.1021/acs.chemrev.2c00569**.
53 Y. Wang, J. Mao, X. Meng, L. Yu, D. Deng and X. Bao, *Chem. Rev.*, 2019, **119**, 1806–1854.
54 L. Wang, W. Chen, D. Zhang, Y. Du, R. Amal, S. Qiao, J. Wu and Z. Yin, *Chem. Soc. Rev.*, 2019, **48**, 5310–5349.
55 A. Arora, P. Oswal, A. Datta and A. Kumar, *Coord. Chem. Rev.*, 2022, **459**, 214406.
56 L. Zhang, M. Zhou, A. Wang and T. Zhang, *Chem. Rev.*, 2020, **120**, 683–733.
57 D. Zhao, Z. Zhuang, X. Cao, C. Zhang, Q. Peng, C. Chen and Y. Li, *Chem. Soc. Rev.*, 2020, **49**, 2215–2264.
58 L. Tong, L. Duan, A. Zhou and R. P. Thummel, *Coord. Chem. Rev.*, 2020, **402**, 213079.
59 G. D. Liberto, L. A. Cipriano and G. Pacchioni, *J. Am. Chem. Soc.*, 2021, **143**, 20431–20441.
60 S. Ji, Y. Chen, X. Wang, Z. Zhang, D. Wang and Y. Li, *Chem. Rev.*, 2020, **120**, 11900–11955.
61 Y.-S. Wei, M. Zhang, R. Zou and Q. Xu, *Chem. Rev.*, 2020, **120**, 12089–12174.
62 H. Xu, Y. Zhao, Q. Wang, G. He and H. Chen, *Coord. Chem. Rev.*, 2022, **451**, 214261.
63 S. Zhang, M. Jin, T. Shi, M. Han, Q. Sun, Y. Lin, Z. Ding, L. R. Zheng, G. Wang, Y. Zhang, H. Zhang and H. Zhao, *Angew. Chem., Int. Ed.*, 2020, **59**, 13423–13429.
64 M. Li, H. Wang, W. Luo, P. C. Sherrell, J. Chen and J. Yang, *Adv. Mater.*, 2020, **32**, 2001848.
65 S. Rej, H. Tsurugi and K. Mashima, *Coord. Chem. Rev.*, 2018, **355**, 223–239.
66 J.-W. Wang, D.-C. Zhong and T.-B. Lu, *Coord. Chem. Rev.*, 2018, **377**, 225–236.
67 G. Li, D. Zhu, X. Wang, Z. Su and M. R. Bryce, *Chem. Soc. Rev.*, 2020, **49**, 765–838.
68 Y. Hu, Z. Li, B. Li and C. Yu, *Small*, 2022, **18**, 2203589.
69 Y. Pan, C. Zhang, Z. Liu, C. Chen and Y. Li, *Matter*, 2020, **2**, 78–110.
70 K. Sonogashira, Y. Tohda and N. Hagihara, *Tetrahedron Lett.*, 1975, **16**, 4467–4470.
71 H. A. Dieck and F. R. Heak, *J. Organomet. Chem.*, 1975, **93**, 259–263.
72 J. Liu, J. Xue, G.-P. Yang, L.-L. Dang, L.-F. Ma, D.-S. Li and Y.-Y. Wang, *Coord. Chem. Rev.*, 2022, **463**, 214521.
73 T. Shima, Q. Zhuo and Z. Hou, *Coord. Chem. Rev.*, 2022, **472**, 214766.
74 W. Xu, M. Li, L. Qiao and J. Xie, *Chem. Commun.*, 2020, **56**, 8524–8536.
75 N. Qiu, J. Li, H. Wang and Z. Zhang, *Sci. China Mater.*, 2022, **65**, 3302–3323.
76 T. He, A. R. P. Santiago, Y. Kong, M. A. Ahsan, R. Luque, A. Du and H. Pan, *Small*, 2022, **18**, 2106091.
77 S. Zhang, Y. Wu, Y.-X. Zhang and Z. Niu, *Sci. China: Chem.*, 2021, **64**, 1908–1922.
78 S. Abednatanzi, P. G. Derakhshandeh, H. Depauw, F.-X. Coudert, H. Vrielinck, P. Van, D. Voort and K. Leus, *Chem. Soc. Rev.*, 2019, **48**, 2535–2565.
79 S. Tian, Q. Fu, W. Chen, Q. Feng, Z. Chen, J. Zhang, W.-C. Cheong, R. Yu, L. Gu, J. Dong, J. Luo, C. Chen, Q. Peng, C. Draxl, D. Wang and Y. Li, *Nat. Commun.*, 2018, **9**, 2353.
80 Y. Li, C. Chen, R. Cao, Z. Pan, H. He and K. Zhou, *Appl. Catal., B*, 2020, **268**, 118747.
81 H. Yan, Y. Lin, H. Wu, W. Zhang, Z. Sun, H. Cheng, W. Liu, C. Wang, J. Li, X. Huang, T. Yao, J. Yang, S. Wei and J. Lu, *Nat. Commun.*, 2017, **8**, 1070.
82 J. Li, H. Huang, W. Xue, K. Sun, X. Song, C. Wu, L. Nie, Y. Li, C. Liu, Y. Pan, H.-L. Jiang, D. Mei and C. Zhong, *Nat. Catal.*, 2021, **4**, 719–729.
83 T. Ding, X. Liu, Z. Tao, T. Liu, T. Chen, W. Zhang, X. Shen, D. Liu, S. Wang, B. Pang, D. Wu, L. Cao, L. Wang, T. Liu, Y. Li, H. Sheng, M. Zhu and T. Yao, *J. Am. Chem. Soc.*, 2021, **143**, 11317–11324.
84 J. Jiao, R. Lin, S. Liu, W.-C. Cheong, C. Zhang, Z. Chen, Y. Pan, J. Tang, K. Wu, S.-F. Hung, H. M. Chen, L. Zheng, Q. Lu, X. Yang, B. Xu, H. Xiao, J. Li, D. Wang, Q. Peng, C. Chen and Y. Li, *Nat. Chem.*, 2019, **11**, 222–228.
85 J. Fesseler, J.-H. Jeoung and H. Dobbek, *Angew. Chem., Int. Ed.*, 2015, **54**, 8560–8564.
86 M. Shoji, H. Isobec, T. Nakajima and K. Yamaguchi, *Chem. Phys. Lett.*, 2015, **640**, 23–30.
87 J. B. Vincent, G. L. Olivier-Lilley and B. A. Averill, *Chem. Rev.*, 1990, **90**, 1447–1467.
88 L. Que Jr and W. B. Tolman, *Nature*, 2008, **455**, 333–340.
89 Y.-J. Yuan, Z.-T. Yu, D.-Q. Chen and Z.-G. Zou, *Chem. Soc. Rev.*, 2017, **46**, 603–631.
90 Y. Yuan, J. Yang and A. Lei, *Chem. Soc. Rev.*, 2021, **50**, 10058–10086.
91 N. K. Szymczak, L. A. Berben and J. C. Peters, *Chem. Commun.*, 2009, 6729–6731.
92 J. Jökel, F. Schwer, M. Delius and U.-P. Apfel, *Chem. Commun.*, 2020, **56**, 14179–14182.
93 T. Fang, L.-Z. Fu, L.-L. Zhou and S.-Z. Zhan, *Electrochim. Acta*, 2015, **161**, 388–394.
94 Y. Han, H. Fang, H. Jing, H. Sun, H. Lei, W. Lai and R. Cao, *Angew. Chem., Int. Ed.*, 2016, **55**, 5457–5462.
95 X. Guo, N. Wang, X. Li, Z. Zhang, J. Zhao, W. Ren, S. Ding, G. Xu, J. Li, U.-P. Apfel, W. Zhang and R. Cao, *Angew. Chem., Int. Ed.*, 2020, **59**, 8941–8946.
96 M. Ogawa, G. Ajayakumar, S. Masaoka, H.-B. Kraatz and K. Sakai, *Chem. – Eur. J.*, 2011, **17**, 1148–1162.
97 S. Ding, P. Ghosh, A. M. Lunsford, N. Wang, N. Bhuvanesh, M. B. Hall and M. Y. Darensbourg, *J. Am. Chem. Soc.*, 2016, **138**, 12920–12927.
98 J.-P. Collin, A. Jouaiti and J.-P. Sauvage, *Inorg. Chem.*, 1988, **27**, 1986–1990.
99 N. Weder, N. S. Grundmann, B. Probst, O. Blacque, R. Ketkaew, F. Creazzo, S. Luber and R. Alberto, *ChemSusChem*, 2022, **15**, e202201049.
100 L.-L. Zhou, L.-Z. Fu, L.-Z. Tang, Y.-X. Zhang and S.-Z. Zhan, *Int. J. Hydrogen Energy*, 2015, **40**, 5099–5105.

101 J. Du, F. Li and L. Sun, *Chem. Soc. Rev.*, 2021, **50**, 2663–2695.
102 S. M. Barnett, K. I. Goldberg and J. M. Mayer, *Nat. Chem.*, 2012, **4**, 498–502.
103 X.-J. Su, M. Gao, L. Jiao, R.-Z. Liao, P. E. M. Siegbahn, J.-P. Cheng and M.-T. Zhang, *Angew. Chem., Int. Ed.*, 2015, **54**, 4909–4914.
104 Q.-F. Chen, Z.-Y. Cheng, R.-Z. Liao and M.-T. Zhang, *J. Am. Chem. Soc.*, 2021, **143**, 19761–19768.
105 S. J. Koepke, K. M. Light, P. E. VanNatta, K. M. Wiley and M. T. Kieber-Emmons, *J. Am. Chem. Soc.*, 2017, **139**, 8586–8600.
106 G. Ruan, P. Ghosh, N. Fridman and G. Maayan, *J. Am. Chem. Soc.*, 2021, **143**, 10614–10623.
107 F. Xie and M.-T. Zhang, *J. Energy Chem.*, 2021, **63**, 1–7.
108 W. A. A. Arafa, M. D. Kärkäs, B.-L. Lee, T. Åkermark, R.-Z. Liao, H.-M. Berends, J. Messinger, P. E. M. Siegbahna and B. Åkermark, *Phys. Chem. Chem. Phys.*, 2014, **16**, 11950–11964.
109 A. Dey, A. Guha, V. Kumar, S. Bawari, T. N. Narayanan and V. Chandrasekhar, *Dalton Trans.*, 2021, **50**, 14257–14263.
110 A. Petronilho, J. A. Woods, S. Bernhard and M. Albrecht, *Eur. J. Inorg. Chem.*, 2014, 708–714.
111 M.-C. Kafentzi, R. Papadakis, F. Gennarini, A. Kochem, O. Iranzo, Y. L. Mest, N. L. Poul, T. Tron, B. Faure, A. J. Simaan and M. Réglier, *Chem. – Eur. J.*, 2018, **24**, 5213–5224.
112 X. Zhang, Y.-Y. Li, J. Jiang, R. Zhang, R.-Z. Liao and M. Wang, *Inorg. Chem.*, 2020, **59**, 5424–5432.
113 Q.-Q. Hu, X.-J. Su and M.-T. Zhang, *Inorg. Chem.*, 2018, **57**, 10481–10484.
114 X.-J. Su, C. Zheng, Q.-Q. Hu, H.-Y. Du, R.-Z. Liao and M.-T. Zhang, *Dalton Trans.*, 2018, **47**, 8670–8675.
115 T. Ishizuka, A. Watanabe, H. Kotani, D. Hong, K. Satonaka, T. Wada, Y. Shiota, K. Yoshizawa, K. Ohara, K. Yamaguchi, S. Kato, S. Fukuzumi and T. Kojima, *Inorg. Chem.*, 2016, **55**, 1154–1164.
116 G. Chen, T. Fan, B. Liu, M. Xue, J.-J. Wei, S.-R. Kang, H.-X. Tong and X.-Y. Yi, *Dalton Trans.*, 2021, **50**, 2018–2022.
117 M. Shao, Q. Chang, J.-P. Dodelet and R. Chenitz, *Chem. Rev.*, 2016, **116**, 3594–3657.
118 R. Jasinski, *Nature*, 1964, **201**, 1212–1213.
119 L. Wang, M. Gennari, F. G. C. Reinhard, J. Gutierrez, A. M. C. Philouze, S. Demeshko, V. Artero, F. Meyer, S. P. de Visser and C. Duboc, *J. Am. Chem. Soc.*, 2019, **141**, 8244–8253.
120 N. Mihara, Y. Yamada, H. Takaya, Y. Kitagawa, S. Aoyama, K. Igawa, K. Tomooka and K. Tanaka, *Chem. – Eur. J.*, 2017, **23**, 7508–7514.
121 L. Nurdin, D. M. Spasyuk, L. Fairburn, W. E. Piers and L. Maron, *J. Am. Chem. Soc.*, 2018, **140**, 16094–16105.
122 Y. Liu, G. Zhou, Z. Zhang, H. Lei, Z. Yao, J. Li, J. Lin and R. Cao, *Chem. Sci.*, 2020, **11**, 87–96.
123 A. M. J. Devoille and J. B. Love, *Dalton Trans.*, 2012, **41**, 65–72.
124 K. M. Kadish, L. Frémond, J. Shen, P. Chen, K. Ohkubo, S. Fukuzumi, M. E. Ojaimi, C. P. Gros, J.-M. Barbe and R. Guilard, *Inorg. Chem.*, 2009, **48**, 2571–2582.
125 M. Volpe, H. Hartnett, J. W. Leeland, K. Wills, M. Ogunshun, B. J. Duncombe, C. Wilson, A. J. Blake, J. McMaster and J. B. Love, *Inorg. Chem.*, 2009, **48**, 5195–5207.
126 C. Liu, H. Lei, Z. Zhang, F. Chen and R. Cao, *Chem. Commun.*, 2017, **53**, 3189–3192.
127 S. Sinha and L. M. Mirica, *ACS Catal.*, 2021, **11**, 5202–5211.
128 Y. Oh and X. Hu, *Chem. Soc. Rev.*, 2013, **42**, 2253–2261.
129 Z. Guo, G. Chen, C. Cometto, B. Ma, H. Zhao, T. Groizard, L. Chen, H. Fan, W.-L. Man, S.-M. Yiu, K.-C. Lau, T.-C. Lau and M. Robert, *Nat. Catal.*, 2019, **2**, 801–808.
130 R. Giereth, P. Lang, E. McQueen, X. Meißner, B. Braun-Cula, C. Marchfelder, M. Obermeier, M. Schwalbe and S. Tschierlei, *ACS Catal.*, 2021, **11**, 390–403.
131 J.-W. Wang, J.-K. Sun, D.-C. Liu and L. Jiang, *Eur. J. Inorg. Chem.*, 2020, 4450–4453.
132 D. Hong, T. Kawanishi, Y. Tsukakoshi, H. Kotani, T. Ishizuka and T. Kojima, *J. Am. Chem. Soc.*, 2019, **141**, 20309–20317.
133 Y. Kuramochi, Y. Fujisawa and A. Satake, *J. Am. Chem. Soc.*, 2020, **142**, 705–709.
134 C. Matlachowski, B. Braun, S. Tschierlei and M. Schwalbe, *Inorg. Chem.*, 2015, **54**, 10351–10360.
135 L.-M. Cao, H.-H. Huang, J.-W. Wang, D.-C. Zhong and T.-B. Lu, *Green Chem.*, 2018, **20**, 798–803.
136 D. E. Polyansky, D. C. Grills, M. Z. Ertem, K. T. Ngo and E. Fujita, *ACS Catal.*, 2022, **12**, 1706–1717.
137 W. Yang, S. S. Roy, W. C. Pitts, R. L. Nelson, F. R. Fronczek and J. W. Jurss, *Inorg. Chem.*, 2018, **57**, 9564–9575.
138 M. Cheng, Y. Yu, X. Zhou, Y. Luo and M. Wang, *ACS Catal.*, 2019, **9**, 768–774.
139 A. Wilting, T. Stolper, R. A. Mata and I. Siewert, *Inorg. Chem.*, 2017, **56**, 4176–4185.
140 W. Guo, K. Zhang, Z. Liang, R. Zou and Q. Xu, *Chem. Soc. Rev.*, 2019, **48**, 5658–5716.
141 P. L. Arnold, T. Ochiai, F. Y. T. Lam, R. P. Kelly, M. L. Seymour and L. Maron, *Nat. Chem.*, 2020, **12**, 654–659.
142 F. Schendzielorz, M. Finger, J. Abbenseth, C. Wgrtele, V. Krewald and S. Schneider, *Angew. Chem., Int. Ed.*, 2019, **58**, 830–834.
143 A. Fujishima and K. Honda, *Nature*, 1972, **238**, 37–38.
144 S. Wang, G. Liu and L. Wang, *Chem. Rev.*, 2019, **119**, 5192–5247.
145 Q. Ding, F. Meng, C. R. English, M. Cabán-Acevedo, M. J. Shearer, D. Liang, A. S. Daniel, R. J. Hamers and S. Jin, *J. Am. Chem. Soc.*, 2014, **136**, 8504–8507.
146 W.-J. Ong, L.-L. Tan, Y. H. Ng, S.-T. Yong and S.-P. Chai, *Chem. Rev.*, 2016, **116**, 7159–7329.
147 R. Yang, J. Liu, B. Wang, R. Wang, Y. Song, Y. Hua, C. Wang, Y. She, J. Yuan, H. Xu and H. Li, *J. Alloys Compd.*, 2022, **895**, 162290.
148 K. Sun, J. Shen, Q. Liu, H. Tang, M. Zhang, S. Zulfiqar and C. Lei, *Chin. J. Catal.*, 2020, **41**, 72–81.
149 T. Wei, P. Ding, T. Wang, L.-M. Liu, X. An and X. Yu, *ACS Catal.*, 2021, **11**, 14669–14676.
150 Y. Feng, Y. Wang, K. Wang, C. Ban, Y. Duan, J. Meng, X. Liu, J. Ma, J. Dai, D. Yu, C. Wang, L. Gan and X. Zhou, *Nano Energy*, 2022, **103**, 107853.

151 Z. Chen, Y. Xu, D. Ding, G. Song, X. Gan, H. Li, W. Wei, J. Chen, Z. Li, Z. Gong, X. Dong, C. Zhu, N. Yang, J. Ma, R. Gao, D. Luo, S. Cong, L. Wang, Z. Zhao and Y. Cui, *Nat. Commun.*, 2022, **13**, 763.
152 Y. Yang, Y. Qian, H. Li, Z. Zhang, Y. Mu, D. Do, B. Zhou, J. Dong, W. Yan, Y. Qin, L. Fang, R. Feng, J. Zhou, P. Zhang, J. Dong, G. Yu, Y. Liu, X. Zhang and X. Fan, *Sci. Adv.*, 2020, **6**, eaba6586.
153 N. Yao, P. Li, Z. Zhou, Y. Zhao, G. Cheng, S. Chen and W. Luo, *Adv. Energy Mater.*, 2019, **9**, 1902449.
154 B. Geng, F. Yan, X. Zhang, Y. He, C. Zhu, S.-L. Chou, X. Zhang and Y. Chen, *Adv. Mater.*, 2021, **33**, 2106781.
155 L. Zhang, Y. Jia, H. Liu, L. Zhuang, X. Yan, C. Lang, X. Wang, D. Yang, K. Huang, S. Feng and X. Yao, *Angew. Chem., Int. Ed.*, 2019, **58**, 9404–9408.
156 J. Guo, J. Liu, X. Zhang, X. Guan, M. Zeng, J. Shen, J. Zou, Q. Chen, T. Wang and D. Qian, *J. Mater. Chem. A*, 2022, **10**, 13727–13734.
157 T. Chao, X. Luo, W. Chen, B. Jiang, J. Ge, Y. Lin, G. Wu, X. Wang, Y. Hu, Z. Zhuang, Y. Wu, X. Hong and Y. Li, *Angew. Chem., Int. Ed.*, 2017, **56**, 16047–16051.
158 L. Zhang, R. Si, H. Liu, N. Chen, Q. Wang, K. Adair, Z. Wang, J. Chen, Z. Song, J. Li, M. N. Banis, R. Li, T.-K. Sham, M. Gu, L.-M. Liu, G. A. Botton and X. Sun, *Nat. Commun.*, 2019, **10**, 4936.
159 Z. Li, S. Xu, K. Chu, G. Yao, Y. Xu, P. Niu, Y. Yang and F. Zheng, *Inorg. Chem.*, 2020, **59**, 13741–13748.
160 H. Cheng, Y. Diao, Q. Liu, L. Wei, X. Li, J. Chen and F. Wang, *Chem. Eng. J.*, 2022, **428**, 131084.
161 L. Bai, C.-S. Hsu, D. T. L. Alexander, H. M. Chen and X. Hu, *J. Am. Chem. Soc.*, 2019, **141**, 14190–14199.
162 M. Liu, N. Li, S. Cao, X. Wang, X. Lu, L. Kong, Y. Xu and X.-H. Bu, *Adv. Mater.*, 2022, **34**, 2107421.
163 Y.-S. Wei, L. Sun, M. Wang, J. Hong, L. Zou, H. Liu, Y. Wang, M. Zhang, Z. Liu, Y. Li, S. Horike, K. Suenaga and Q. Xu, *Angew. Chem., Int. Ed.*, 2020, **59**, 16013–16022.
164 K. Rui, G. Zhao, Y. Chen, Y. Lin, Q. Zhou, J. Chen, J. Zhu, W. Sun, W. Huang and S. Xue Dou, *Adv. Funct. Mater.*, 2018, **28**, 1801554.
165 D. Yu, Y. Ma, F. Hu, C.-C. Lin, L. Li, H.-Y. Chen, X. Han and S. Peng, *Adv. Energy Mater.*, 2021, **11**, 2101242.
166 F. Pan, T. Jin, W. Yang, H. Li, Y. Cao, J. Hu, X. Zhou, H. Liu and X. Duan, *Chem. Catal.*, 2021, **1**, 734–745.
167 T. Cui, Y.-P. Wang, T. Ye, J. Wu, Z. Chen, J. Li, Y. Lei, D. Wang and Y. Li, *Angew. Chem., Int. Ed.*, 2022, **61**, e202115219.
168 Y. Jin, S. Huang, X. Yue, H. Du and P. K. Shen, *ACS Catal.*, 2018, **8**, 2359–2363.
169 X. Han, X. Ling, D. Yu, D. Xie, L. Li, S. Peng, C. Zhong, N. Zhao, Y. Deng and W. Hu, *Adv. Mater.*, 2019, **31**, 1905622.
170 Z. Pei, X. F. Lu, H. Zhang, Y. Li, D. Luan and X. W. Lou, *Angew. Chem., Int. Ed.*, 2022, **61**, e202207537.
171 D. D. Babu, Y. Huang, G. Anandhababu, X. Wang, R. Si, M. Wu, Q. Li, Y. Wang and J. Yao, *J. Mater. Chem. A*, 2019, **7**, 8376–8383.
172 M. Xiao, J. Zhu, S. Li, G. Li, W. Liu, Y.-P. Deng, Z. Bai, L. Ma, M. Feng, T. Wu, D. Su, J. Lu, A. Yu and Z. Chen, *ACS Catal.*, 2021, **11**, 8837–8846.
173 Y. Zhou, L. Chen, L. Sheng, Q. Luo, W. Zhang and J. Yang, *Nano Res.*, 2022, **15**, 7994–8000.
174 Z. Li, H. He, H. Cao, S. Sun, W. Diao, D. Gao, P. Lu, S. Zhang, Z. Guo, M. Li, R. Liu, D. Ren, C. Liu, Y. Zhang, Z. Yang, J. Jiang and G. Zhang, *Appl. Catal., B*, 2019, **240**, 112–121.
175 X. Zhu, D. Zhang, C.-J. Chen, Q. Zhang, R.-S. Liu, Z. Xia, L. Dai, R. Amal and X. Lu, *Nano Energy*, 2020, **71**, 104597.
176 J. Liu, Y. Zheng, Z. Wang, Z. Lu, A. Vasileff and S.-Z. Qiao, *Chem. Commun.*, 2018, **54**, 463–466.
177 J. Chen, H. Li, C. Fan, Q. Meng, Y. Tang, X. Qiu, G. Fu and T. Ma, *Adv. Mater.*, 2020, **32**, 2003134.
178 B. Wei, Z. Fu, D. Legut, T. C. Germann, S. Du, H. Zhang, J. S. Francisco and R. Zhang, *Adv. Mater.*, 2021, **33**, 2102595.
179 Y. Zhao, X. Yan, K. R. Yang, S. Cao, Q. Dong, J. E. Thorne, K. L. Materna, S. Zhu, X. Pan, M. Flytzani-Stephanopoulos, G. W. Brudvig, V. S. Batista and D. Wang, *ACS Cent. Sci.*, 2018, **4**, 1166–1172.
180 Q. Zhao, Z. Yan, C. Chen and J. Chen, *Chem. Rev.*, 2017, **117**, 10121–10211.
181 X. Yan, Y. Jia and X. Yao, *Chem. Soc. Rev.*, 2018, **47**, 7628–7658.
182 W. Ye, S. Chen, Y. Lin, L. Yang, S. Chen, X. Zheng, Z. Qi, C. Wang, R. Long, M. Chen, J. Zhu, P. Gao, L. Song, J. Jiang and Y. Xiong, *Chem*, 2019, **5**, 2865–2878.
183 N. Zhang, T. Zhou, J. Ge, Y. Lin, Z. Du, C. Zhong, W. Wang, Q. Jiao, R. Yuan, Y. Tian, W. Chu, C. Wu and Y. Xie, *Matter*, 2020, **3**, 509–521.
184 M. Xiao, H. Zhang, Y. Chen, J. Zhu, L. Gao, Z. Jin, J. Ge, Z. Jiang, S. Chen, C. Liu and W. Xing, *Nano Energy*, 2018, **46**, 396–403.
185 J. Wang, Z. Huang, W. Liu, C. Chang, H. Tang, Z. Li, W. Chen, C. Jia, T. Yao, S. Wei, Y. Wu and Y. Li, *J. Am. Chem. Soc.*, 2017, **139**, 17281–17284.
186 M. Xiao, Y. Chen, J. Zhu, H. Zhang, X. Zhao, L. Gao, X. Wang, J. Zhao, J. Ge, Z. Jiang, S. Chen, C. Liu and W. Xing, *J. Am. Chem. Soc.*, 2019, **141**, 17763–17770.
187 R. Zhao, Z. Liang, S. Gao, C. Yang, B. Zhu, J. Zhao, C. Qu, R. Zou and Q. Xu, *Angew. Chem., Int. Ed.*, 2019, **58**, 1975–1979.
188 H. Li, Y. Wen, M. Jiang, Y. Yao, H. Zhou, Z. Huang, J. Li, S. Jiao, Y. Kuang and S. Luo, *Adv. Funct. Mater.*, 2021, **31**, 2011289.
189 M. Jiang, F. Wang, F. Yang, H. He, J. Yang, W. Zhang, J. Luo, J. Zhang and C. Fu, *Nano Energy*, 2022, **93**, 106793.
190 M. Ma, A. Kumar, D. Wang, Y. Wang, Y. Jia, Y. Zhang, G. Zhang, Z. Yan and X. Sun, *Appl. Catal., B*, 2020, **274**, 119091.
191 C. Du, Y. Gao, H. Chen, P. Li, S. Zhu, J. Wang, Q. He and W. Chen, *J. Mater. Chem. A*, 2020, **8**, 16994–17001.
192 H. Sun, M. Wang, S. Zhang, S. Liu, X. Shen, T. Qian, X. Niu, J. Xiong and C. Yan, *Adv. Funct. Mater.*, 2021, **31**, 2006533.

193 S. Gong, C. Wang, P. Jiang, L. Hu, H. Lei and Q. Chen, *J. Mater. Chem. A*, 2018, **6**, 13254–13262.
194 B. Wang, J. Zou, X. Shen, Y. Yang, G. Hu, W. Li, Z. Peng, D. Banham, A. Dong and D. Zhao, *Nano Energy*, 2019, **63**, 103851.
195 G. Yang, J. Zhu, P. Yuan, Y. Hu, G. Qu, B.-A. Lu, X. Xue, H. Yin, W. Cheng, J. Cheng, W. Xu, J. Li, J. Hu, S. Mu and J.-N. Zhang, *Nat. Commun.*, 2021, **12**, 1734.
196 Z. Chen, X. Liao, C. Sun, K. Zhao, D. Ye, J. Li, G. Wu, J. Fang, H. Zhao and J. Zhang, *Appl. Catal., B*, 2021, **288**, 120021.
197 P. Zhu, X. Xiong, X. Wang, C. Ye, J. Li, W. Sun, X. Sun, J. Jiang, Z. Zhuang, D. Wang and Y. Li, *Nano Lett.*, 2022, **22**, 9507–9515.
198 M. Li, H. Zhu, Q. Yuan, T. Li, M. Wang, P. Zhang, Y. Zhao, D. Qin, W. Guo, B. Liu, X. Yang, Y. Liu and Y. Pan, *Adv. Funct. Mater.*, 2022, 2210867.
199 Z. Lu, B. Wang, Y. Hu, W. Liu, Y. Zhao, R. Yang, Z. Li, J. Luo, B. Chi, Z. Jiang, M. Li, S. Mu, S. Liao, J. Zhang and X. Sun, *Angew. Chem., Int. Ed.*, 2019, **58**, 2622–2626.
200 J. Zang, F. Wang, Q. Cheng, G. Wang, L. Ma, C. Chen, L. Yang, Z. Zou, D. Xie and H. Yang, *J. Mater. Chem. A*, 2020, **8**, 3686–3691.
201 M. Tong, F. Sun, Y. Xie, Y. Wang, Y. Yang, C. Tian, L. Wang and H. Fu, *Angew. Chem., Int. Ed.*, 2021, **60**, 14005–14012.
202 X. Zeng, J. Shui, X. Liu, Q. Liu, Y. Li, J. Shang, L. Zheng and R. Yu, *Adv. Energy Mater.*, 2018, **8**, 1701345.
203 R. Gao, J. Wang, Z.-F. Huang, R. Zhang, W. Wang, L. Pan, J. Zhang, W. Zhu, X. Zhang, C. Shi, J. Lim and J.-J. Zou, *Nat. Energy*, 2021, **6**, 614–623.
204 L. Zhang, J. Melisande, T. A. Fischer, Y. Jia, X. Yan, W. Xu, X. Wang, J. Chen, D. Yang, H. Liu, L. Zhuang, M. Hankel, D. J. Searles, K. Huang, S. Feng, C. L. Brown and X. Yao, *J. Am. Chem. Soc.*, 2018, **140**, 10757–10763.
205 M. Luo, Z. Zhao, Y. Zhang, Y. Sun, Y. Xing, F. Lv, Y. Yang, X. Zhang, S. Hwang, Y. Qin, J.-Y. Ma, F. Lin, D. Su, G. Lu and S. Guo, *Nature*, 2019, **574**, 81–85.
206 J. Long, R. Li and X. Gou, *Catal. Commun.*, 2017, **95**, 31–35.
207 Y. Zhou, W. Yang, W. Utetiwabo, Y. Lian, X. Yin, L. Zhou, P. Yu, R. Chen and S. Sun, *J. Phys. Chem. Lett.*, 2020, **11**, 1404–1410.
208 Z. Li, T. Yang, W. Zhao, T. Xu, L. Wei, J. Feng, X. Yang, H. Ren and M. Wu, *ACS Appl. Mater. Interfaces*, 2019, **11**, 3937–3945.
209 D. Zhang, W. Chen, Z. Li, Y. Chen, L. Zheng, Y. Gong, Q. Li, R. Shen, Y. Han, W.-C. Cheong, L. Gu and Y. Li, *Chem. Commun.*, 2018, **54**, 4274–4277.
210 J. Wang, W. Liu, G. Luo, Z. Li, C. Zhao, H. Zhang, M. Zhu, Q. Xu, X. Wang, C. Zhao, Y. Qu, Z. Yang, T. Yao, Y. Li, Y. Lin, Y. Wu and Y. Li, *Energy Environ. Sci.*, 2018, **11**, 3375–3379.
211 G. Zhang, Y. Jia, C. Zhang, X. Xiong, K. Sun, R. Chen, W. Chen, Y. Kuang, L. Zheng, H. Tang, W. Liu, J. Liu, X. Sun, W.-F. Lin and H. Dai, *Energy Environ. Sci.*, 2019, **12**, 1317–1325.
212 X. Liu, L. Wang, P. Yu, C. Tian, F. Sun, J. Ma, W. Li and H. Fu, *Angew. Chem., Int. Ed.*, 2018, **57**, 16166–16170.
213 L. Chen, Y. Zhang, L. Dong, W. Yang, X. Liu, L. Long, C. Liu, S. Dong and J. Jia, *J. Mater. Chem. A*, 2020, **8**, 4369–4375.
214 X. Fang, L. Jiao, S.-H. Yu and H.-L. Jiang, *ChemSusChem*, 2017, **10**, 3019–3024.
215 Y.-J. Wu, X.-H. Wu, T.-X. Tu, P.-F. Zhang, J.-T. Li, Y. Zhou, L. Huang and S.-G. Sun, *Appl. Catal., B*, 2020, **278**, 119259.
216 F. Luo, S. Wagner, I. Onishi, S. Selve, S. Li, W. Ju, H. Wang, J. Steinberg, A. Thomas, U. I. Kramm and P. Strasser, *Chem. Sci.*, 2021, **12**, 384–396.
217 D. Liu, B. Wang, H. Li, S. Huang, M. Liu, J. Wang, Q. Wang, J. Zhang and Y. Zhao, *Nano Energy*, 2019, **58**, 277–283.
218 N. Zhang, T. Zhou, J. Ge, Y. Lin, Z. Du, C. Zhong, W. Wang, Q. Jiao, R. Yuan, Y. Tian, W. Chu, C. Wu and Y. Xie, *Matter*, 2020, **3**, 509–521.
219 Y. Wu, C. Ye, L. Yu, Y. Liu, J. Huang, J. Bi, L. Xue, J. Sun, J. Yang, W. Zhang, X. Wang, P. Xiong and J. Zhu, *Energy Storage Mater.*, 2022, **45**, 805–813.
220 Z. Hu, Z. Guo, Z. Zhang, M. Dou and F. Wang, *ACS Appl. Mater. Interfaces*, 2018, **10**, 12651–12658.
221 W. Yang, H.-J. Wang, R.-R. Liu, J.-W. Wang, C. Zhang, C. Li, D.-C. Zhong and T.-B. Lu, *Angew. Chem., Int. Ed.*, 2021, **60**, 409–414.
222 J. Wang, E. Kim, D. P. Kumar, A. P. Rangappa, Y. Kim, Y. Zhang and T. Kim, *Angew. Chem., Int. Ed.*, 2022, **61**, e202113044.
223 M. Wang, D. Chen, N. Li, Q. Xu, H. Li, J. He and J. Lu, *Adv. Mater.*, 2022, **34**, 2202960.
224 H. Ou, S. Ning, P. Zhu, S. Chen, A. Han, Q. Kang, Z. Hu, J. Ye, D. Wang and Y. Li, *Angew. Chem., Int. Ed.*, 2022, **61**, e202206579.
225 H. Shi, H. Wang, Y. Zhou, J. Li, P. Zhai, X. Li, G. G. Gurzadyan, J. Hou, H. Yang and X. Guo, *Angew. Chem., Int. Ed.*, 2022, **61**, e202208904.
226 G. Jia, M. Sun, Y. Wang, Y. Shi, L. Zhang, X. Cui, B. Huang and J. C. Yu, *Adv. Funct. Mater.*, 2022, **32**, 2206817.
227 Z.-H. Yan, M.-H. Du, J. Liu, S. Jin, C. Wang, G.-L. Zhuang, X.-J. Kong, L.-S. Long and L.-S. Zheng, *Nat. Commun.*, 2018, **9**, 3353.
228 K. Sekizawa, K. Maeda, K. Domen, K. Koike and O. Ishitani, *J. Am. Chem. Soc.*, 2013, **135**, 4596–4599.
229 D. Saito, Y. Yamazaki, Y. Tamaki and O. Ishitani, *J. Am. Chem. Soc.*, 2020, **142**, 19249–19258.
230 Q.-Q. Bi, J.-W. Wang, J.-X. Lv, J. Wang, W. Zhang and T.-B. Lu, *ACS Catal.*, 2018, **8**, 11815–11821.
231 S.-J. Li, Y.-B. Chang, M. Li, Y.-X. Feng and W. Zhang, *RSC Adv.*, 2020, **10**, 17951–17954.
232 H. Jiang, S. Gong, S. Xu, P. Shi, J. Fan, V. Cecen, Q. J. Xu and Y. L. Min, *Dalton Trans.*, 2020, **49**, 5074–5086.
233 J. Zhang, Y. Wang, H. Wang, D. Zhong and T. Lu, *Chin. Chem. Lett.*, 2022, **33**, 2065–2068.
234 Z. Wang, H. Lee, J. Chen, M. Wu, D. Y. C. Leung, C. A. Grimes, Z. Lu, Z. Xu and S.-P. Feng, *J. Power Sources*, 2020, **466**, 228306.
235 H. Lai, W. Xiao, Y. Wang, T. Song, B. Long, S. Yin, A. Ali and G.-J. Deng, *Chem. Eng. J.*, 2021, **417**, 129295.

236 J. Wang, Y. Song, C. Zuo, R. Li, Y. Zhou, Y. Zhang and B. Wu, *J. Colloid Interface Sci.*, 2022, **625**, 722–733.
237 Y. Wang, B. J. Park, V. K. Paidi, R. Huang, Y. Lee, K.-J. Noh, K.-S. Lee and J. W. Han, *ACS Energy Lett.*, 2022, **7**, 640–649.
238 X. Cao, L. Zhao, B. Wulan, D. Tan, Q. Chen, J. N. Ma and J. Zhang, *Angew. Chem., Int. Ed.*, 2022, **61**, e202113918.
239 Y.-N. Gong, C.-Y. Cao, W.-J. Shi, J.-H. Zhang, J.-H. Deng, T.-B. Lu and D.-C. Zhong, *Angew. Chem., Int. Ed.*, 2022, **61**, e202215187.
240 L. Zhang, X.-X. Li, Z.-L. Lang, Y. Liu, J. Liu, L. Yuan, W.-Y. Lu, Y.-S. Xia, L.-Z. Dong, D.-Q. Yuan and Y.-Q. Lan, *J. Am. Chem. Soc.*, 2021, **143**, 3808–3816.
241 L.-L. Zhuo, P. Chen, K. Zheng, X.-W. Zhang, J.-X. Wu, D.-Y. Lin, S.-Y. Liu, Z.-S. Wang, J.-Y. Liu, D.-D. Zhou and J.-P. Zhang, *Angew. Chem., Int. Ed.*, 2022, **61**, e202204967.
242 P. Shao, W. Zhou, Q.-L. Hong, L. Yi, L. Zheng, W. Wang, H.-X. Zhang, H. Zhang and J. Zhang, *Angew. Chem., Int. Ed.*, 2021, **60**, 16687–16692.
243 R. Wang, J. Liu, Q. Huang, L.-Z. Dong, S.-L. Li and Y.-Q. Lan, *Angew. Chem., Int. Ed.*, 2021, **60**, 19829–19835.
244 N. Zhang, X. Zhang, Y. Kang, C. Ye, R. Jin, H. Yan, R. Lin, J. Yang, Q. Xu, Y. Wang, Q. Zhang, L. Gu, L. Liu, W. Song, J. Liu, D. Wang and Y. Li, *Angew. Chem., Int. Ed.*, 2021, **60**, 13388–13393.
245 W. Ren, X. Tan, W. Yang, C. Jia, S. Xu, K. Wang, S. C. Smith and C. Zhao, *Angew. Chem., Int. Ed.*, 2019, **58**, 6972–6976.
246 L. Jiao, J. Zhu, Y. Zhang, W. Yang, S. Zhou, A. Li, C. Xie, X. Zheng, W. Zhou, S.-H. Yu and H.-L. Jiang, *J. Am. Chem. Soc.*, 2021, **143**, 19417–19424.
247 Y. Li, W. Shan, M. J. Zachman, M. Wang, S. Hwang, H. Tabassum, J. Yang, X. Yang, S. Karakalos, Z. Feng, G. Wang and G. Wu, *Angew. Chem., Int. Ed.*, 2022, **61**, e202205632.
248 Z. Zeng, L. Y. Gan, H. B. Yang, X. Su, J. Gao, W. Liu, H. Matsumoto, J. Gong, J. Zhang, W. Cai, Z. Zhang, Y. Yan, B. Liu and P. Chen, *Nat. Commun.*, 2021, **12**, 4088.
249 Q. He, Y. Zhang, H. Li, Y. Yang, S. Chen, W. Yan, J. Dong, X.-M. Zhang and X. Fan, *Small*, 2022, **18**, 2108034.
250 F. Wang, H. Xie, T. Liu, Y. Wu and B. Chen, *Appl. Energy*, 2020, **269**, 115029.
251 M. Feng, X. Wu, H. Cheng, Z. Fan, X. Li, F. Cui, S. Fan, Y. Dai, G. Lei and G. He, *J. Mater. Chem. A*, 2021, **9**, 23817–23827.
252 J. Pei, T. Wang, R. Sui, X. Zhang, D. Zhou, F. Qin, X. Zhao, Q. Liu, W. Yan, J. Dong, L. Zheng, A. Li, J. Mao, W. Zhu, W. Chen and Z. Zhuang, *Energy Environ. Sci.*, 2021, **14**, 3019–3028.
253 J.-D. Yi, X. Gao, H. Zhou, W. Chen and Y. Wu, *Angew. Chem., Int. Ed.*, 2022, **61**, e202212329.
254 W. Zhu, L. Zhang, S. Liu, A. Li, X. Yuan, C. Hu, G. Zhang, W. Deng, K. Zang, J. Luo, Y. Zhu, M. Gu, Z.-J. Zhao and J. Gong, *Angew. Chem., Int. Ed.*, 2020, **59**, 12664–12668.
255 H. Cheng, X. Wu, M. Feng, X. Li, G. Lei, Z. Fan, D. Pan, F. Cui and G. He, *ACS Catal.*, 2021, **11**, 12673–12681.
256 C. Ding, C. Feng, Y. Mei, F. Liu, H. Wang, M. Dupuis and C. Li, *Appl. Catal., B*, 2020, **268**, 118391.
257 X. Zhang, C. Liu, Y. Zhao, L. Li, Y. Chen, F. Raziq, L. Qiao, S.-X. Guo, C. Wang, G. G. Wallace, A. M. Bond and J. Zhang, *Appl. Catal., B*, 2021, **291**, 120030.
258 C. Yang, B. H. Ko, S. Hwang, Z. Liu, Y. Yao, W. Luc, M. Cui, A. S. Malkani, T. Li, X. Wang, J. Dai, B. Xu, G. Wang, D. Su, F. Jiao and L. Hu, *Sci. Adv.*, 2020, **6**, eaaz6844.
259 Y. Li, B. Wei, M. Zhu, J. Chen, Q. Jiang, B. Yang, Y. Hou, L. Lei, Z. Li, R. Zhang and Y. Lu, *Adv. Mater.*, 2021, **33**, 2102212.
260 W. Xie, H. Li, G. Cui, J. Li, Y. Song, S. Li, X. Zhang, J. Y. Lee, M. Shao and M. Wei, *Angew. Chem., Int. Ed.*, 2021, **60**, 7382–7388.
261 D. Tan, W. Lee, Y. E. Kim, Y. N. Ko, M. H. Youn, Y. E. Jeon, J. Hong, J. E. Park, J. Seo, S. K. Jeong, Y. Choi, H. Choi, H. Y. Kim and K. T. Park, *ACS Appl. Mater. Interfaces*, 2022, **14**, 28890–28899.
262 G. Wen, D. U. Lee, B. Ren, F. M. Hassan, G. Jiang, Z. P. Cano, J. Gostick, E. Croiset, Z. Bai, L. Yang and Z. Chen, *Adv. Energy Mater.*, 2018, **8**, 1802427.
263 Y. Wang, L. Cao, N. J. Libretto, X. Li, C. Li, Y. Wan, C. He, J. Lee, J. Gregg, H. Zong, D. Su, J. T. Miller, T. Mueller and C. Wang, *J. Am. Chem. Soc.*, 2019, **141**, 16635–16642.
264 M.-J. Sun, Z.-W. Gong, J.-D. Yi, T. Zhang, X. Chen and R. Cao, *Chem. Commun.*, 2020, **56**, 8798–8801.
265 J. Hao, Z. Zhuang, J. Hao, C. Wang, S. Lu, F. Duan, F. Xu, M. Du and H. Zhu, *Adv. Energy Mater.*, 2022, **12**, 2200579.
266 S. Singh, R. K. Gautam, K. Malik and A. Verma, *J. CO_2* Util., 2017, **18**, 139–146.
267 L. Lin, H. Li, C. Yan, H. Li, R. Si, M. Li, J. Xiao, G. Wang and X. Bao, *Adv. Mater.*, 2019, **31**, 1903470.
268 Z. Liang, L. Song, M. Sun, B. Huang and Y. Du, *Sci. Adv.*, 2021, **7**, eabl4915.
269 W. Xiong, J. Yang, L. Shuai, Y. Hou, M. Qiu, X. Li and M. K. H. Leung, *ChemElectroChem*, 2019, **6**, 5951–5957.
270 M. Balamurugan, H.-Y. Jeong, V. S. K. Choutipalli, J. S. Hong, H. Seo, N. Saravanan, J. H. Jang, K.-G. Lee, Y. H. Lee, S. W. Im, V. Subramanian, S. H. Kim and K. T. Nam, *Small*, 2020, **16**, 2000955.
271 W. Ni, Z. Liu, X. Guo, Y. Zhang, C. Ma, Y. Deng and S. Zhang, *Appl. Catal., B*, 2021, **291**, 120092.
272 X. Ma, J. Tian, M. Wang, X. Jin, M. Shena and L. Zhang, *Catal. Sci. Technol.*, 2021, **11**, 6096–6102.
273 Q. Gong, Y. Wang, X. Ren, C. He, J. Liu and Q. Zhang, *ChemSusChem*, 2021, **14**, 4499–4506.
274 M. Xie, Y. Shen, W. Ma, D. Wei, B. Zhang, Z. Wang, Y. Wang, Q. Zhang, S. Xie, C. Wang and Y. Wang, *Angew. Chem., Int. Ed.*, 2022, **61**, e2022134.
275 X.-F. Qiu, H.-L. Zhu, J.-R. Huang, P.-Q. Liao and X.-M. Chen, *J. Am. Chem. Soc.*, 2021, **143**, 7242–7246.
276 H.-L. Zhu, H.-Y. Chen, Y.-X. Han, Z.-H. Zhao, P.-Q. Liao and X.-M. Chen, *J. Am. Chem. Soc.*, 2022, **144**, 13319–13326.
277 T. He, A. R. P. Santiago and A. Du, *J. Catal.*, 2020, **388**, 77–83.
278 X. Guo, J. Gu, S. Lin, S. Zhang, Z. Chen and S. Huang, *J. Am. Chem. Soc.*, 2020, **142**, 5709–5721.
279 X. Lv, W. Wei, B. Huang, Y. Dai and T. Frauenheim, *Nano Lett.*, 2021, **21**, 1871–1878.

280 C. N. Sun, Z. L. Wang, X.-Y. Lang, Z. Wen and Q. Jiang, *ChemSusChem*, 2021, **14**, 4593–4600.
281 L. J. Arachchige, Y. Xu, Z. Dai, X. L. Zhang, F. Wang and C. Sun, *J. Mater. Sci. Technol.*, 2021, **77**, 244–251.
282 M. Qu, G. Qin, J. Fan, A. Du and Q. Sun, *Appl. Surf. Sci.*, 2021, **537**, 148012.
283 K. An, H. Ren, D. Yang, Z. Zhao, Y. Gao, Y. Chen, J. Tan, W. Wang and Z. Jiang, *Appl. Catal., B*, 2021, **292**, 120167.
284 N. Zhang, A. Jalil, D. Wu, S. Chen, Y. Liu, C. Gao, W. Ye, Z. Qi, H. Ju, C. Wang, X. Wu, L. Song, J. Zhu and Y. Xiong, *J. Am. Chem. Soc.*, 2018, **140**, 9434–9443.
285 Y. Xiong, B. Li, Y. Gu, T. Yan, Z. Ni, S. Li, J.-L. Zuo, J. Ma and Z. Jin, *Nat. Chem.*, 2023, **15**, 286–293.
286 X. Wang, S. Qiu, J. Feng, Y. Tong, F. Zhou, Q. Li, L. Song, S. Chen, K.-H. Wu, P. Su, S. Ye, F. Hou, S. X. Dou, H. K. Liu, G. Q. Lu, C. Sun, J. Liu and J. Liang, *Adv. Mater.*, 2020, **32**, 2004382.
287 L. Zhang, G. Fan, W. Xu, M. Yu, L. Wang, Z. Yan and F. Cheng, *Chem. Commun.*, 2020, **56**, 11957–11960.
288 S. Chen, H. Jang, J. Wang, Q. Qin, X. Liu and J. Cho, *J. Mater. Chem. A*, 2020, **8**, 2099–2104.
289 Y. Li, Q. Zhang, C. Li, H.-N. Fan, W.-B. Luo, H.-K. Liu and S.-X. Dou, *J. Mater. Chem. A*, 2019, **7**, 22242–22247.
290 Y. Ma, T. Yang, H. Zou, W. Zang, Z. Kou, L. Mao, Y. Feng, L. Shen, S. J. Pennycook, L. Duan, X. Li and J. Wang, *Adv. Mater.*, 2020, **32**, 2002177.
291 Y. Liu, Y. Luo, Q. Li, J. Wang and K. Chu, *Chem. Commun.*, 2020, **56**, 10227–10230.
292 L. Han, Z. Ren, P. Ou, H. Cheng, N. Rui, L. Lin, X. Liu, L. Zhuo, J. Song, J. Sun, J. Luo and H. L. Xin, *Angew. Chem., Int. Ed.*, 2021, **60**, 345–350.
293 N. Cao, Z. Chen, K. Zang, J. Xu, J. Zhong, J. Luo, X. Xu and G. Zheng, *Nat. Commun.*, 2019, **10**, 2877.
294 X. Li, Y. Tian, X. Wang, Y. Guo and K. Chu, *Sustainable Energy Fuels*, 2021, **5**, 4277–4283.

